Lars Kaestner · Peter Lipp *Editors*

Microscopy of the Heart

Springer

Microscopy of the Heart

Lars Kaestner • Peter Lipp
Editors

Microscopy of the Heart

Springer

Editors
Lars Kaestner
Theoretical Medicine and Biosciences
Saarland University
Homburg/Saar, Germany

Peter Lipp
Preclinical Center for Molecular Signal
Processing, Building 61
Saarland University
Homburg/Saar, Germany

ISBN 978-3-319-95302-1 ISBN 978-3-319-95304-5 (eBook)
https://doi.org/10.1007/978-3-319-95304-5

Library of Congress Control Number: 2018963211

This Springer imprint is published by the registered company Springer Nature Switzerland AG
The registered company address is: Gewerbestrasse 11, 6330 Cham, Switzerland

Preface

The heart is one of the most vital organs in the mammalian body—failure is immediately associated with the death of the entire organism. This is one of the reasons the heart is situated in the well-protected ribcage and is therefore hardly accessible by classical microscopic techniques. However, non-invasive imaging like sonography or magnet resonance tomography allows visualisation of the heart and its subunits in operation and is therefore referred to as functional imaging. Although these techniques are sometimes denoted as microscopic methods, within this book we regard microscopy to start at a resolution limit of one micrometre or below and therefore only such approaches are included. They allow subcellular investigations of the basic building blocks of the heart, the cardiomyocytes. Albeit a part of cardiac diseases can only be understood at the organ level, other pathologies have a clear cellular or molecular origin. These peculiarities require besides the investigations of molecular biology and genetics the microscopic characterisation of the cardiac myocytes, either in a histologic manner or with increasing importance as cellular functional readouts. Although this is more common in animal models, it is also possible with cells from patients' biopsies.

Most of the techniques presented in this book therefore require a particular sample preparation in the form of slices (electron microscopy) or cell isolations (optical microscopy, scanning ion conductance microscopy) or other modes of dissections like the preparation of the sinoatrial node (selective plane imaging) or the atrial auricles (second harmonic generation microscopy).

Since the first microscope was build, which is believed to have happened at the end of the sixteenth century, more than 400 years of research and development resulted in devices that not only are mechano-optical in nature as the first generations of microscopes but also to a large extent are based on electric and electronic components. There has been particular great progress in the development of microscopic methods within the last decades resulting in Nobel Prize for the development of both molecular sensors and imaging technologies. Within this book we provide an overview of state-of-the-art microscopic methods to investigate the ultrastructure of the cardiac cells (super-resolution microscopy, electron microscopy), their cellular und subcellular function (genetically encoded indicators, optical sectioning microscopy, uncaging techniques, scanning ion conductance microscopy) as well as extracellular components like the extracellular matrix (second harmonic generation

microscopy). It is a timely overview for both students and established scientists since many proof-of-principle techniques still await their final establishment and routine application in cellular cardiology, like the use of second harmonic generation microscopy (transmission mode) of myosin to quantify the contraction of stem cell-derived cardiomyocytes.

Homburg/Saar, Germany Lars Kaestner
November, 2018

Contents

Studying Structure and Function of the Heart Cells Using Scanning Ion Conductance Microscopy

Anamika Bhargava and Julia Gorelik

Introduction

Scanning ion conductance microscopy (SICM) is a kind of scanning probe microscopy (SPM) that provides images of nonconducting surfaces that are covered with electrolytes, for example plasma membranes of biological cells, composed of non-conducting lipids [1]. Biological surfaces have complex 3D structures associated with complex functions. Real-time investigation of the membrane structure and function of living cells is of utmost importance, however techniques are limited. Conventional microscopy is limited by light diffraction limit (advanced optical imaging reaching a resolution of ~5–100 nm). Non optical methods like atomic force microscopy can reach resolutions up to ~10 nm but the intermittent contact with the sample and the use of force can sometimes distort the biological membrane structures. Techniques like scanning electron microscopy provide high resolution up to ~0.5 nm but it is invasive and the samples require special fixing procedures so that the sample is compromised. A demand for non-optical high resolution imaging of live samples promoted rapid development of SICM [2–6] and its successful application to imaging topography of live biological cells where existing microdomains can be imaged. A particular advantage of SICM technique for imaging biological cells is that it requires no physical contact with the sample and

A. Bhargava
Department of Biotechnology, Indian Institute of Technology Hyderabad, Kandi, Sangareddy, Telangana, India

J. Gorelik (✉)
Department of Cardiovascular Sciences, Imperial Centre for Translational and Experimental Medicine, National Heart and Lung Institute, Imperial College London, London, UK
e-mail: j.gorelik@imperial.ac.uk

L. Kaestner, P. Lipp (eds.), *Microscopy of the Heart*,
https://doi.org/10.1007/978-3-319-95304-5_1

operates at nanoscale resolution. In particular, this offers a unique advantage to studying cardiomyocytes whose plasma membrane is organized into specialized microdomains.

The Technique of SICM

History

In 1989, Hansma and colleagues [1] used a glass pipette microelectrode filled with an electrolyte solution as a probe for SPM. It is based on principle that ion current flowing through the micropipette tip decreases when it approaches the surface of a nonconducting substrate. Thus, by using the ion current through the micropipette tip as a feedback signal for SPM, it is possible to obtain images of the membrane surface. However this technique in its original form was not very successful in imaging biological surfaces as they are much more convoluted and can have relatively high protrusions, like microvilli.

The technique was improved by Korchev and colleagues [3] at Imperial College London and first high-resolution images of living cells were obtained using fine glass microelectrodes pulled with standard pipette pullers, used in every electrophysiology laboratory. The setup consisted of standard electrophysiological patch-clamp electronics, with SICM controller added on. Further development by Novak and colleagues [7] adapted the technique to image taller biological structures and was named as hopping probe ion conductance microscopy (HPICM), described later in this chapter.

Setup

The instrument typically uses an inverted microscope. A computer-controlled three axis piezotranslation system, typically with 100 × 100 μm x–y piezo-stage for sample positioning and 25 μm z-axis piezo-actuator for pipette movement, is mounted on the microscope stage. The glass micropipette is mounted on the vertical piezo-actuator stage and connected to the headstage of a patch clamp amplifier. Ag/AgCl electrodes, in the bath and pipette, provide an electrical connection in a conventional electrophysiological circuit (Fig. 1). The electrode consists of a micropipette of defined tip geometry that is usually made from a borosilicate glass capillary of 1.00-mm outer diameter, 0.78-mm inner diameter pulled using a laser-based puller. The ion currents flowing through the pipette are measured at applied DC voltages of 50–200 mV and are used in the feedback loop that controls the micropipette's vertical position.

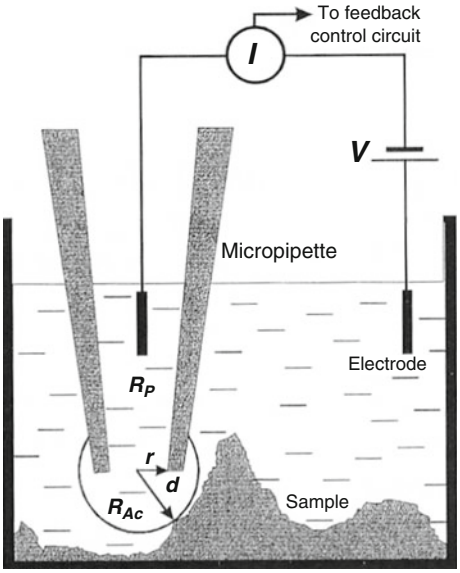

Fig. 1 Principle of the scanning ion conductance microscope. Diagram shows the micropipette tip/surface interaction. The position of the micropipette tip relative to the sample surface strongly influences the access resistance (R_{Ac}) and, consequently, the ion current (I) flowing through the pipette. The current value at a distance (d) that exceeds the radius (r) can be used to control the vertical position of the pipette tip to sense neighboring structures that are higher than the vertical sample/probe separation. During the scan, the tip of the pipette, with its "spherical current sensor" of radius d, "rolls" over surface irregularities of the specimen without damaging it. Modified with permission from [3]

Principle

When an electrolyte-filled pipette approaches a non-conducting surface at a distance comparable to the size of the pipette tip opening, the current through the tip drops due to restrictions to ion movement imposed by the lack of space to move freely. The ion current through the pipette is proportional to the distance between the pipette tip and the surface [3]. This ion current is digitized and fed into the feedback control system of SICM, which provides the signal to the vertical piezo-actuator to control the vertical position of the tip of pipette, keeping a constant pipette-sample separation. By keeping the pipette current constant (so the distance between the pipette tip and the sample surface remains constant) and scanning the sample, it is possible to obtain an image of the surface without physical contact between the pipette and the surface. The ion current through the pipette depends on overall resistance of the pipette tip, which is a combination of the resistance of the micropipette itself (Rp) and the access resistance (R_{AC}) of the micropipette opening. R_{AC} is a complex function of the distance between the sample and the probe, and the geometry and

electrochemical properties of the sample surface. The current (I) through the pipette, which is measured directly, is given by:

$$I = V/(Rp + Ra^{*}d)$$

where "V" is the voltage applied to the electrode and "d" is the distance between sample and the probe.

In conventional SICM, a nanopipette is mounted on a three-dimensional piezoelectric translation stage and automatic feedback control moves the pipette up or down to keep the pipette current constant (the set point) while the sample is scanned in x and y directions. Thus, a pipette-sample separation, typically equal to the pipette's inner radius, is maintained during imaging. In this classic form of SICM a continuous feedback mechanism kept the pipette always in the proximity of the sample surface by moving the pipette up and down while the pipette was raster scanning the sample [1, 4]. This could produce good images of relatively flat cells (e.g. fibroblasts). However, because the tip of the probe was very close to the sample, it had limited ability to scan surfaces with prominent tall structures such as microvilli (e.g. on epithelial cells). When the structures were taller than the pipette-sample separation the probe often broke itself or damaged the surface structures.

The recently developed HPICM by Novak and coworkers at Imperial College London circumvented this problem and could obtain clear images of samples with very steep surfaces and complex convoluted structures [7]. In HPICM, continuous feedback is no longer used. Instead, at each imaging point, the pipette approaches the sample from a starting position that is above any of the surface feature. The pipette is then lowered towards cell surface and the current is reduced by a predefined value, which is usually approximately 0.25–1.0% of its initial value. The position of *z*-dimension actuator at which this reduction is achieved is recorded as the height of the sample at this imaging point. The *z*-dimension actuator then withdraws the pipette away from the surface to the starting point. The sample is then moved laterally to a new imaging point, and the procedure is repeated. Because lateral movement occurs while the pipette is raised, the pipette doesn't collide with the sample (Fig. 2).

Imaging of the Heart Cell Topography by SICM

Cardiomyocytes

The foremost application of SICM is to image topography of a large variety of live biological cells. With SICM one can generate 3D topographical images of cells with resolution as high as 20 nm. These cells can be imaged live without any special preparation like fixing or labelling, in their natural environment, such as culture medium. As this is a non-contact microscopy, it does not damage the cells during scanning and the cells can be used afterwards for other procedures. It is particularly useful in the context of cells which have specialized membrane topography.

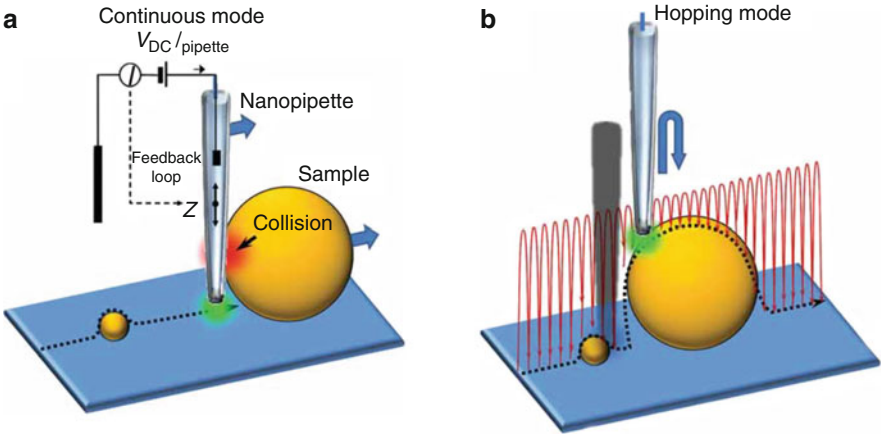

Fig. 2 Principle of the hopping probe ion conductance microscopy (HPICM). (**a**) Scanning nanopipette probe operating in continuous scan mode collides with a large spherical object possessing a steep vertical slope. (**b**) Scanning nanopipette in hopping mode is withdrawn to a position well above the sample before approaching the surface at the next position of the scan. Modified with permission from [7]

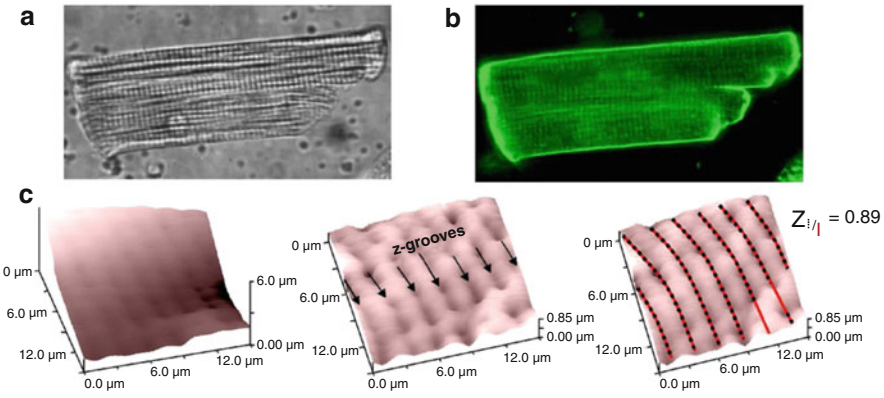

Fig. 3 Calculation of the Z-groove index. (**a**) Bright field optical image of a rat adult ventricular cardiomyocyte. (**b**) Fluorescent image of the same cardiomyocyte labelled with Di-8-ANNEPS. (**c**) SICM topographic image of a cardiomyocyte (left image). Result of filtration processing of image (centre image). Z-groove ratio is calculated by dividing the length of Z-grooves (indicated by dotted lines), to the total length of Z-groove as if they all were present on the surface of the cell (indicated by solid lines) (right image). Reproduced with permission from [8]

Well-differentiated cardiomyocytes isolated from an adult heart possess complex plasma membrane organization; microdomains are present such as Z-grooves containing the openings of the internal system of membranous tubules called T-tubules and in between grooves crests are situated. In Fig. 3 one can see a typical topographical image of a cardiomyocyte. The grooves are invaginations in the

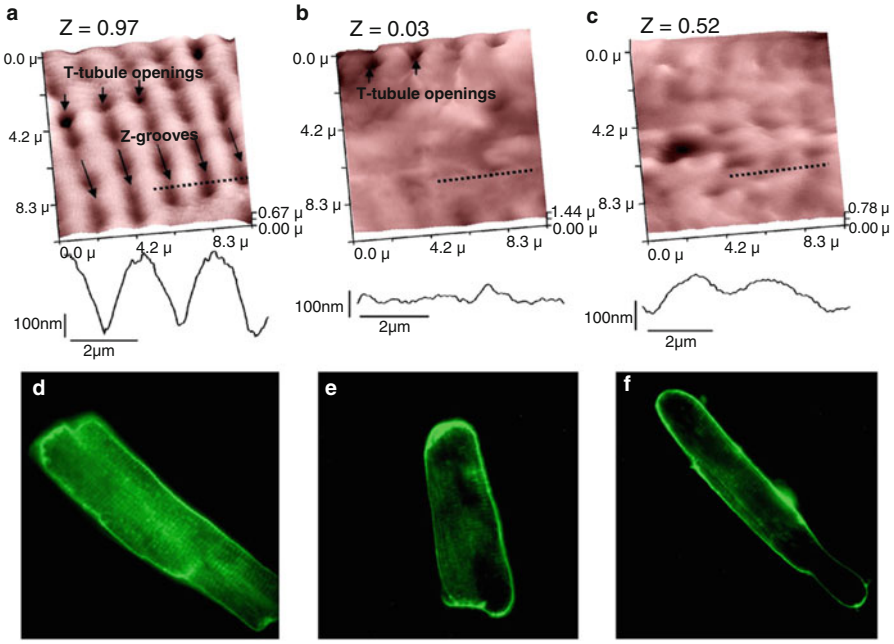

Fig. 4 Loss of external and internal structure of adult rat cardiomyocytes after formamide treatment and prolonged cell culture. (**a**–**c**) SICM topographic image of a representative, freshly isolated cell (**a**), a cell after formamide treatment (**b**) and a cell after 4 days of culture (**c**). Z-grooves, and t-tubule openings are indicated. The profile along the dotted line is shown below each image. Corresponding Z-groove index is indicated above each image. (**d**–**f**) Fluorescent images of cells stained with Di-8-ANNEPS corresponding to cells in (**a**), (**b**), and (**c**), respectively. Modified with permission from [8]

membrane and T-tubule openings are seen as holes in the membrane. Several years ago we calculated the ratio between the average length of Z-grooves on a surface topography image of a cardiomyocyte and the imaginary maximal length of Z-grooves possible on the given surface image; we introduced that as a Z-groove index of structural integrity [8] as can be seen in the Fig. 3. When we chemically destroyed the internal T-tubule network by formamide, we saw the loss of surface topography organization. Similarly, the surface structure can be substantially lost following prolonged culture of cardiomyocytes as revealed in Fig. 4 both by fluorescent imaging and by SICM. Lately, Z-groove index has been successfully used to quantify changes in cardiomyocyte structure happening under conditions of cardiovascular disease like heart failure, myocardial infarction [9]. Figure 5 compares topography of healthy and diseased rat and human cardiomyocytes and one can immediately acknowledge the structural differences. Less T-tubules and Z-grooves are present in diseased cardiomyocytes [9].

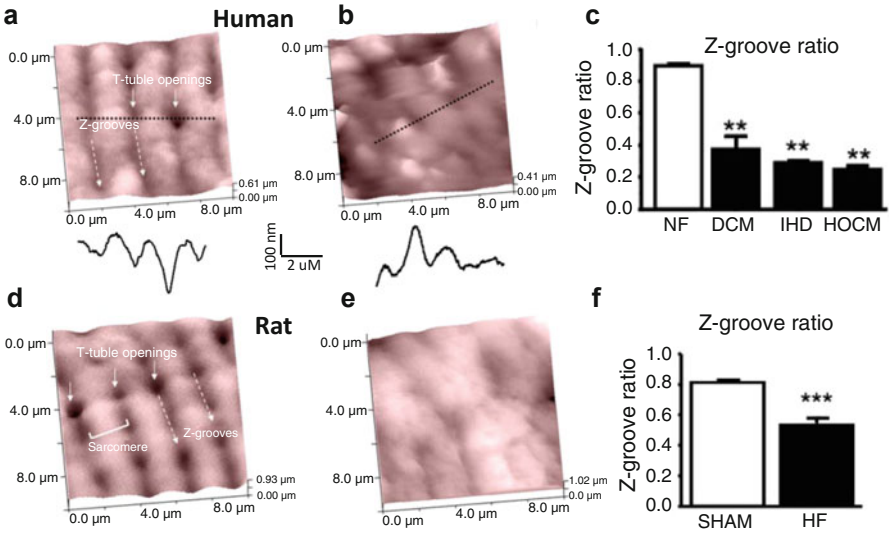

Fig. 5 SICM images of the surface of cardiomyocytes isolated from non-failing (**a**) and failing (**b**) human hearts and sham-ligated (**d**) and failing (**e**) rat hearts. Z-grooves, and t-tubule openings are indicated. The profile along the black dotted line is shown below images (**a**) and (**b**). (**c**) Z-groove ratio for non-failing (NF), dilated cardiomyopathy (DCM), ischaemic heart disease (IHD) and hypertrophic obstructive cardiomyopathy (HOCM) patients (**, $P = 0.001$ vs. NF). (**f**) Z-groove ratio for sham-operated (n 12) and failing rat myocytes (n 16) (***, $P = 0.001$ vs. sham). Modified with permission from [9]

Endothelial Cells

In a similar manner SICM images of aortic endothelial cells have been obtained. The endothelial cells from different aortic regions were isolated and cultured in laboratory conditions [10]. Figure 6 shows the SICM images of aortic endothelial cells. Aortic cells have long been known for their dynamism and the ability to adapt to the shear stress they are subjected to. With SICM imaging we followed these changes by comparing cells from the two aortic regions which experience different shear conditions; importantly the tissue samples were not transparent and therefore not suitable for conventional transmitter light microscopy [10]. In tissue culture, we subjected the cells to shear stress and studied the orientation of cells in cluster that would mimic their organization in vivo. We found that in static conditions endothelial cells oriented randomly but when shear stress was applied they became aligned [10].

Not only aortic tissue samples can be imaged; we have successfully studied valve cells on intact valve preparations [11]. The study of aortic valve structure is important to understand physiology and develop potential valve replacement therapies. The aortic valve is composed of a monolayer of endothelial cells lining both sides of the valve, with a mixed population of interstitial cells in between. SICM could reveal the fundamental topographical differences in the cells from ventricular and atrial sides of the aortic valve (Fig. 6) [11].

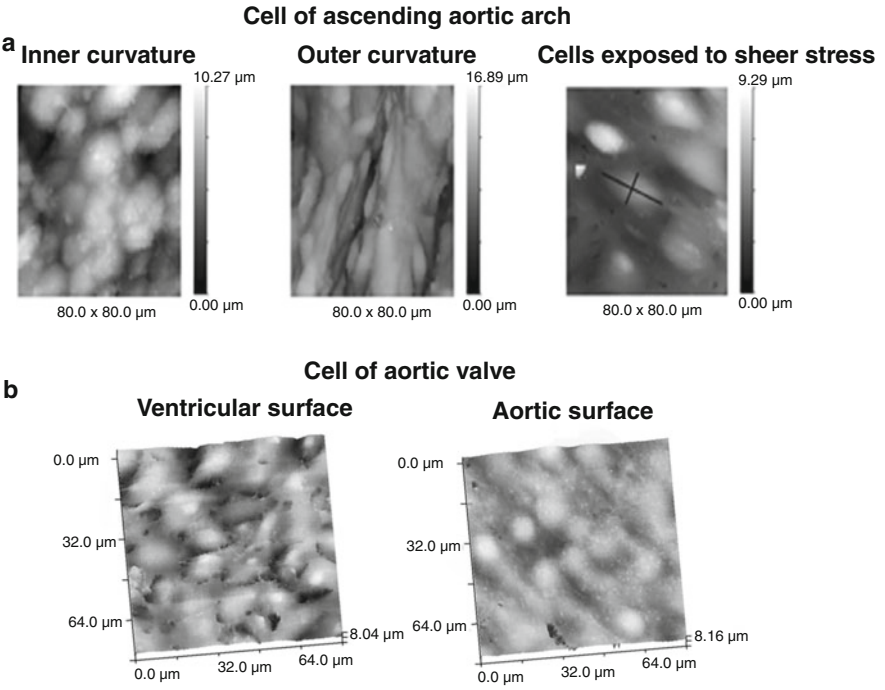

Fig. 6 Differences in topography of endothelial cells from different parts of the aorta and the aortic valve. (**a**) Representative topographical SICM images of the inner and outer curvature regions of the ascending pig aorta and endothelial cells cultured under high shear conditions. The greyscale represents the height of the cells. (**b**) Topography of aortic valve cells on the ventricular and aortic sides of aortic valve cusps. Modified with permission from [10, 11]

Combining Cardiomyocyte Structure with Function

In biology, it is imperative to study structure combined with function to understand the living system in great details and to understand the role the structure plays in defining the function. Emerging concepts suggest that receptors can change their signaling properties depending on their cellular locations [12, 13]. Protein kinases and phosphatases can also form structurally determined microdomains by specific localization to the cytoskeleton thus facilitating local signaling [14]. In recent years we have combined SICM with an array of other techniques to study compartmentation of proteins and signaling which we are going to describe in the next sections.

Super-Resolution Scanning Patch-Clamp

Super-resolution scanning patch-clamp technique, developed recently [15, 16] combines SICM with patch-clamp electrophysiology. Patch-clamp electrophysiology is conventionally used to record ion channel activity from cell membranes.

Combining patch-clamp with SICM gives the information of spatial location of these channels on the plasma membrane and allows study of their distribution. This is useful in deciphering the role they might play in functioning together with the group of other signaling proteins (such as enzymes and docking proteins) in that particular microdomain.

The technique of super-resolution scanning patch-clamp evolved from the earlier developed smart patch-clamp technique [2, 17]. Smart patch-clamp technique uses the glass micropipette as a dual probe: scanning probe and patch-clamp pipette. After obtaining a topographical image, the feedback of the system is turned off and the pipette is lowered manually until it touches the membrane and then light suction results in a gigaseal in quite a conventional way (See schematics in Fig. 7, but without clipping). Recordings can then be performed in patch-clamp mode, the only difference being the size of the tip of the patching pipette (~1 μm in conventional

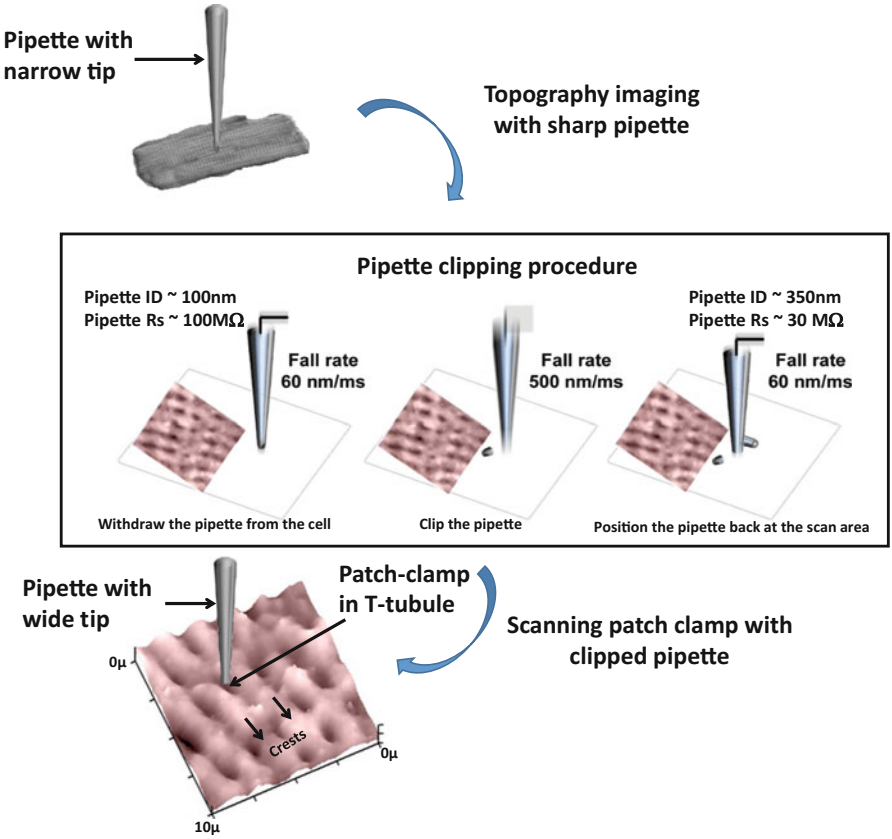

Fig. 7 Schematic depiction of the clipping procedure and the super-resolution scanning patch-clamp. After obtaining a high resolution topography image with sharp pipette, the pipette is clipped using the procedure depicted in the box. The clipped pipette which has a wider tip, is now used for single ion channel recording. Modified with permission from [15]

electrophysiology vs ~100 nm in smart patch-clamp). Using this method we produced a distribution map of calcium and chloride channels in the cardiomyocyte surface (Fig. 8). However this technique is quite tiresome and limited in its throughput because of the use of the very fine-tipped scanning pipette ($\leq$100 nm internal diameter) for patch-clamping. The fine tip of the pipette limits the area under the pipette and thus lowers the chances of recording activity from ion channels under the pipette that are distributed on the sarcolemma.

Subsequently improvement was made to the original technique and that resulted in the super-resolution scanning patch-clamp. After obtaining a high resolution topography image with fine-tipped pipette, the pipette tip is clipped using a software-controlled movement of the piezo-actuator. After generating the topographical image of the surface, the pipette ($\approx$100 nm ID) is moved to a clean area of the dish free from cells or debris. The rate at which the pipette approaches the sample during scanning is then increased to $\approx$500 nm/ms for 500 ms. At such speed the feedback can't properly operate and the pipette tip taps against the solid bottom of the dish. As a result the pipette tip clips, which allows to produce a wider tip without affecting the tip geometry (see the schematics of pipette clipping, Fig. 7). The clipping is constantly monitored by looking at the drop in the pipette resistance. After clipping, the pipette is repositioned to the chosen coordinates based on the SICM image obtained earlier with the sharp pipette. It is possible to reposition the tip back with high precision as the lateral error of the x–y piezo-actuators is only $\pm$2 nm (one can find complete set of specifications in http://www.physikinstrumente.com/product-detail-page/p-6202-p-6292-202400.html). It is important to note that the tip size is only a determinant of the lateral resolution of the scanned image and it does not affect repositioning lateral error. To establish the actual error in our repositioning

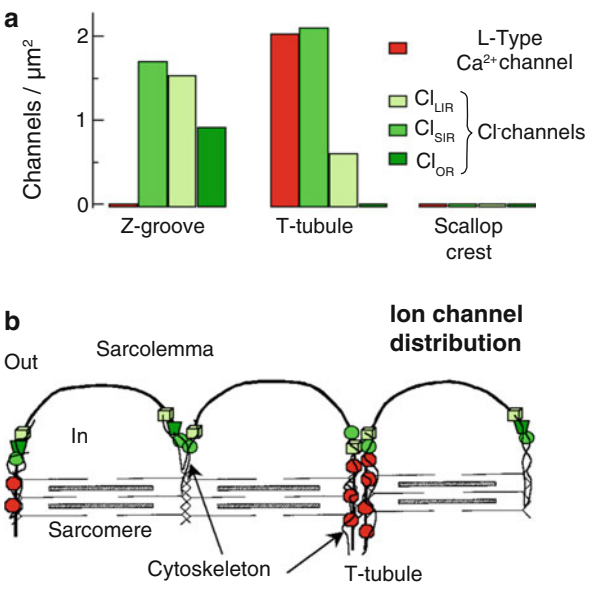

Fig. 8 Calcium and chloride channel distribution. (**a**) Variation of the density of chloride and L-type calcium channels at different positions on the cardiomyocyte surface. (**b**) Functional schematic of the sarcomeric unit showing clustering and co-localization of chloride and calcium channels on the cell surface. Reproduced with permission from [2]

we scanned the same area of a cell before and after clipping of the pipette and despite the fact that the image after clipping was of much lower resolution we could recognize that it showed exactly the same area to the precision of nm (see supplementary Fig. 1 in [15]). Once the *x*, *y* coordinates of the structure are established, the precision with which the pipette is returned to a specific location is determined exclusively by the resolution and repeatability of the *x*–*y* piezo-actuators. Now that the recording tip actually occupies a larger area after clipping, it increases the chance of recording ion channel activity (see the activity recorded vs pipette resistance graph in Fig. 9). The clipping of the pipette tip does not affect the success rate of getting a gigaseal after touching the membrane when compared to success rate without clipping the pipette and is comparable to the conventional patch-clamping [15]. This could be attributable to the fact that the clipping procedure does not change the overall shape of the pipette tip but only allow controlled widening of the tip. This was investigated by electron microscopy of the tips before and immediately after clipping [16]. This super-resolution scanning patch-clamp method permits high resolution imaging of the topography of a live cell and then recording of ion channels from a selected site with nanoscale precision.

This technique is particularly useful to study cells whose membrane have specific microdomains, like cardiomyocytes. Sarcolemma of cardiomyocytes includes numerous microdomains where several ion channels, receptors and cytoskeletal proteins exist together. An excellent example is L-type calcium channels which reside in T-tubular membrane microdomains and with super-resolution scanning patch-clamp technique it was possible to directly record ion channel activity from T-tubular microdomains and study their distribution on the cardiomyocyte surface [15]. Similarly, distribution of sodium channels on the surface of cardiomyocytes has been also studied [15]. An advantage of visualizing ion channels with super-resolution scanning patch-clamp technique over other microscopic techniques such as immunocytochemistry is that it elucidates the location of only functional channels

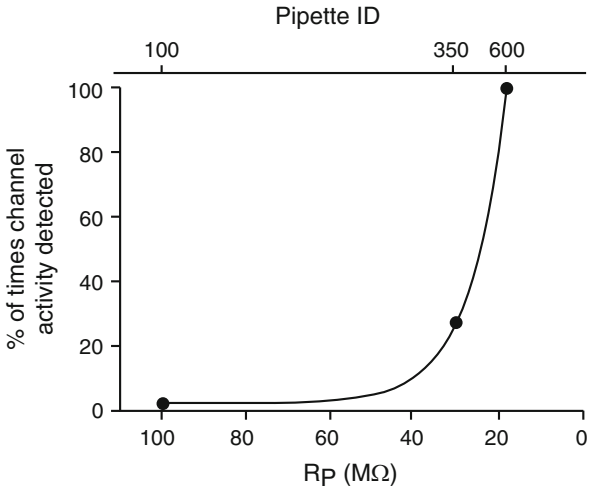

Fig. 9 Relationship between pipette resistance and probability of observing single L-type calcium channel (LTCC) activity. The graph depicts that clipping the pipette tip to 20 MΩ or lower greatly increases the chance of recording single LTCC activity in the T-tubules of cardiomyocytes. Lower *x* axis is pipette resistance (Rp) and upper *x*-axis denotes estimated pipette internal diameter (ID). Reproduced with permission from [15]

that may contribute to ion flux, whereas immunocytochemistry visualizes all the channels irrespective of their functional state and is unable to distinguish between functional and quiescent channels. In principle it is possible to study distribution of any ion channel on the cell surface with super-resolution scanning patch-clamp technique.

SICM-FRET

SICM can be combined with fluorescent imaging techniques like Förster Resonance Energy Transfer (FRET) to study cell signaling in biological cells. The unique advantage of combining FRET with SICM is that with this combined method it is possible to study signaling from individual microdomains on the surface. We developed and used this technique to study β-adrenergic signaling in cardiomyocytes. Adrenergic stimulation of cardiomyocytes has long been studied, but without a good spatial resolution it was rather difficult to study the distribution and compartmentation of cAMP signals that are generated upon activation of β-receptors. Monitoring β-adrenergic-dependent cAMP signaling in living cells in real time is now possible due to the development of highly sensitive fluorescent biosensors [18, 19]. These probes are based on FRET between two fluorophores (for example, CFP and YFP) fused to a single cyclic nucleotide-binding domain taken from proteins like Epac or PKA. Transgenic mice studies using such a sensor have revealed that in cardiomyocytes β1AR-mediated cAMP signals propagated throughout large parts of the cell, whereas β2AR signals were locally confined [19]. Now combining FRET with SICM revealed the role the surface structures play in this compartmentation. We transfected isolated cardiomyocytes with a viral vector containing an EPAC-based FRET sensor. Allowing for viral transfection we first imaged the cardiomyocyte with SICM 48 h later revealing T-tubules and crest structures on the sarcolemma. Then the same nanopipette was positioned above either a T-tubule opening or a crest and β-adrenergic agonist was locally applied through the pipette. To apply the agonist locally, pressure was applied into the pipette while constantly superfusing the cells with the buffer/antagonist solution from the side so that any receptor stimulation that occurs stays local. Results from these experiments suggest that selective stimulation of β1ARs both in T-tubules and crests results in cAMP generation. In contrast, cAMP signals were seen only if β2ARs were stimulated in T-tubules, but not in other regions of the sarcolemma [20]. We concluded that β1ARs are distributed evenly on the plasma membrane whereas β2ARs reside in T-tubules. In cardiomyocytes isolated from a rat model of heart failure we found changes in the surface structure which reflect changes that occur to the internal T-tubular system [9]. Moreover, in failing cardiomyocytes (Fig. 10), β2AR signal is no longer constrained to the T-tubules but observed in both T-tubules and crests in a pattern similar to β1ARs [20]. We proposed that altered cAMP compartmentation with the signal redistributed from the T-tubules to the crests may contribute to altered heart contraction and arrhythmias in heart failure.

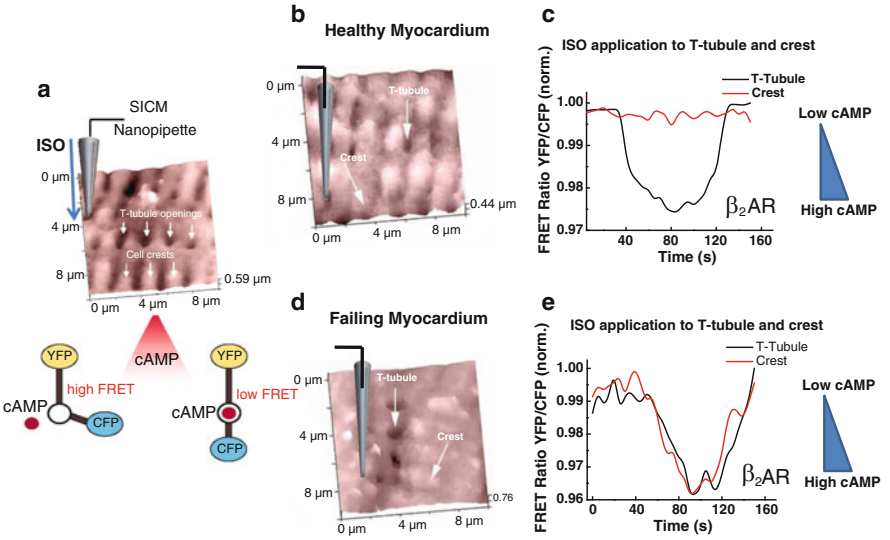

Fig. 10 Functional localization of βAR-induced cAMP signaling. (**a**) Principle of the combined SICM-FRET. SICM surface image indicating the application of isoprenaline (ISO) through the nanopipette above a T-tubule opening. Receptor activity is measured by monitoring the production of cAMP by a FRET sensor Epac2-camps. (**b**) Topography of the surface of a healthy cardiomyocyte with a well-defined structure. Z grooves separating T tubule openings and crests are indicated. (**c**) FRET ratio on application of ISO to either T-tubule (black line) or crest (red line). Low FRET corresponds to high cAMP (indicated on right). (**d**) Topography of the surface of a failing cardiomyocyte showing disrupted surface topography. (**e**) ISO application produces cAMP signals both in T-tubules and crest suggesting the loss of cAMP compartmentation in heart failure. Reproduced with permission from [21]

Scanning Laser Confocal Microscopy

The most fundamental property of cardiomyocytes is their ability to contract. Following scanning of a contracting myocyte the SICM pipette can be positioned at one spot above the cell and the Z-displacement of the nanopipette can be recorded. As cell contracts, its shape changes and the pipette, which follows the membrane moves upwards and downwards. Cardiomyocyte contraction is brought about by the alterations in cytoplasmic calcium concentration. To follow this, SICM can be combined with laser confocal microscopy to record the contraction via pipette concurrently with recording changes in calcium concentration just beneath the membrane in a cell loaded with a fluorescent calcium indicator (e.g. Fluo-4). To combine SICM with laser confocal microscopy the laser is focussed on the tip of the pipette, and the sample is moved up and down to maintain a constant distance between pipette and cell surface [22]. This means that, even during contraction, the fluorescence is recorded at the same distance below the cell membrane. The distance the stage moves and the intensity of the fluo-4 is simultaneously recorded. The confocal volume is centered at the tip of the micropipette by focusing the laser

onto a top surface of the coverslip and bringing the pipette directly in focus above the surface. It is possible to probe intracellular calcium within 1 μm of the cell membrane (Fig. 11) [22].

Recently we successfully used SICM to image and record contractions of human embryonic stem cells derived cardiomyocytes (hESCs) [23]. In the case of hESCs

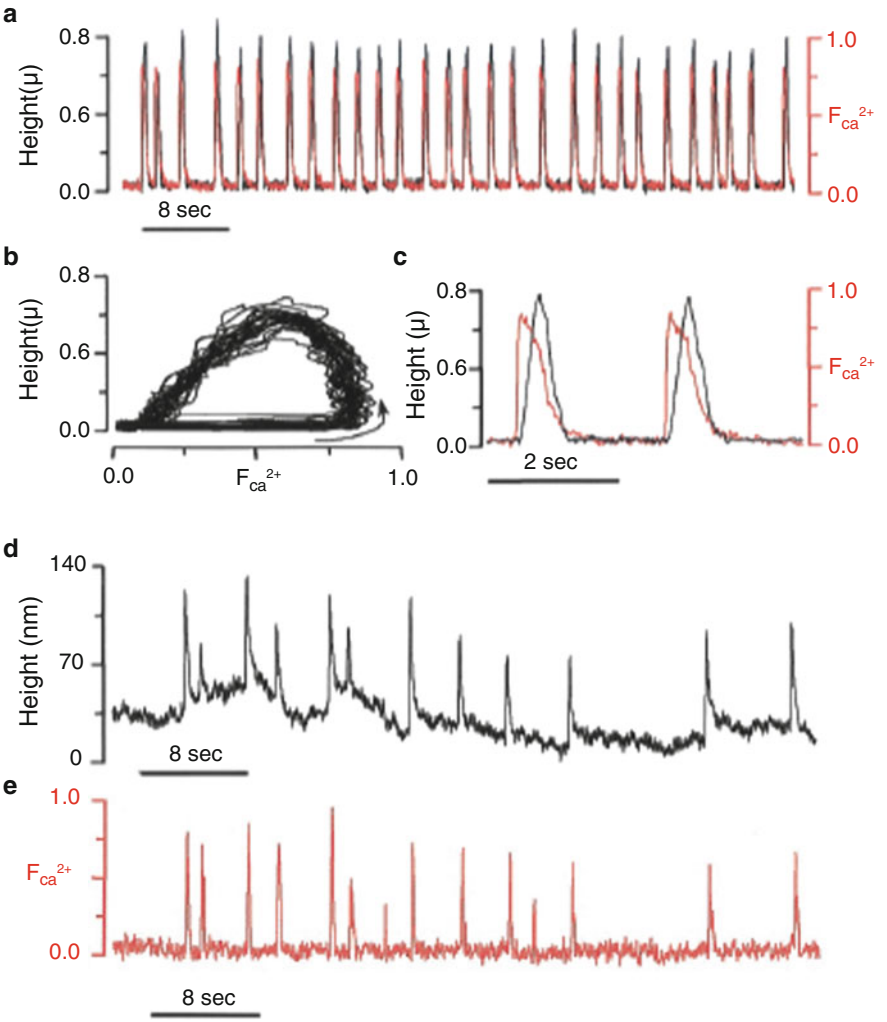

Fig. 11 Simultaneous measurement of contraction and local relative calcium concentration. Simultaneous measurement of the cell surface displacement and intracellular local relative calcium concentration just below the cell surface (**a**, **c**). (**b**) A plot of cell height versus relative calcium concentration for all the contraction in (**a**). (**c**) A blow-up of two of the contractions in (**a**). (**d**, **e**) The simultaneous measurement of the cell height and relative calcium concentration of 1-day-old cultured cardiac myocyte. Figure reproduced with permission from [22]

this technique is extremely useful to characterize the beating clusters of stem cells as to whether they show contraction and calcium characteristics of cardiomyocytes.

Also scanning laser confocal microscopy is a useful tool to test in vitro drugs which can alter the contractility of cardiomyocytes. The SICM setup can be attached to a perfusion system and various drugs can be added to the bath and removed by perfusion of the cells. In this similar context, SICM has been used for studying arrhythmia in an in vitro model of neonatal rat ventricular myocytes where, in the presence of taurocholic acid, known to affect calcium homeostasis, the cells start to show signs of arrhythmia and desynchronized beating with reduced calcium amplitude [24]. With this data the amplitude and the duration of calcium transients can be studied together with contraction without the need for touching the cell.

SICM as a Mechanical Probe

The cell membrane of biological cells is a dynamic structure and therefore its mechanical properties vary at nanoscale level. The mechanical properties of the cellular plasma membrane can also be altered during diseased state. SICM can be applied to study properties of membranes such as membrane compliance and modulus of elasticity. This modification was possible due to the fact that SICM uses a glass nanopipette for imaging and therefore hydrostatic forces can be applied through this nanopipette by displacing the liquid out of the pipette tip at predefined speed. As SICM is a no contact imaging, any contact of the pipette with the cell surface is prohibited thus permitting fast and accurate measurements. Importantly, as SICM can generate topography map with nanoscale resolution pressure can be applied locally at selected locations and thus mechanical properties of the membrane can be probed and compared to other parts of the membrane.

To measure the compliance, the SICM pipette can be mounted in a patch-clamp electrode holder and, after acquiring the topography image, a positive hydrostatic jet (0.1–40 kPa) can be applied through the pressure port in the holder via a tube as traditionally used in patch-clamping for suction. Instead of suction, positive pressure is applied, which can be varied with precision and monitored through a precision pump. This force can be calibrated beforehand, using the AFM cantilever as the gold standard, with applied pipette pressure bending the cantilever. The SICM distance feedback control ensures that the pipette follows the bending lever.

Sanchez and colleagues developed this method where they initially calibrated the SICM using an AFM cantilever with a spring constant of 0.01 N/m [25]. Pipette pressure on the cantilever bends the lever, and then one can measure the corresponding change in pipette position. The relationship between the cantilever deformation and applied pressure is linear. Since the spring constant of the cantilever is known, the distance moved by the cantilever can be directly converted into force using $F = k$ (spring constant) $\times$ (distance) allowing a direct conversion of applied pressure into applied force. The compliance of single cells as result of local dynamic pressure can be calculated from the resistance of the pipette (Rp, determined experimentally), the induced pressure (calculated as above) and the resulting

displacement of the cell surface (determined by changed pipette position on applying pressure) using the formula below [10]:

$$C = d/P \times \sqrt{R}/\sqrt{Ri}$$

where C = compliance d = displacement of the membrane (μm); P = pressure (kPa); R = actual pipette resistance (Ω); Ri = ideal pipette resistance (Ω).

We successfully used this method to measure membrane compliance of endothelial cells from aorta [10] and different regions of aortic valve [11] (Fig. 12) and found that membrane compliance differs between regions. In intact tissue samples endothelial cells on ventricular side of the aortic valve differed significantly in their compliance from the cells on the aortic side. Cells on the ventricular surface of the

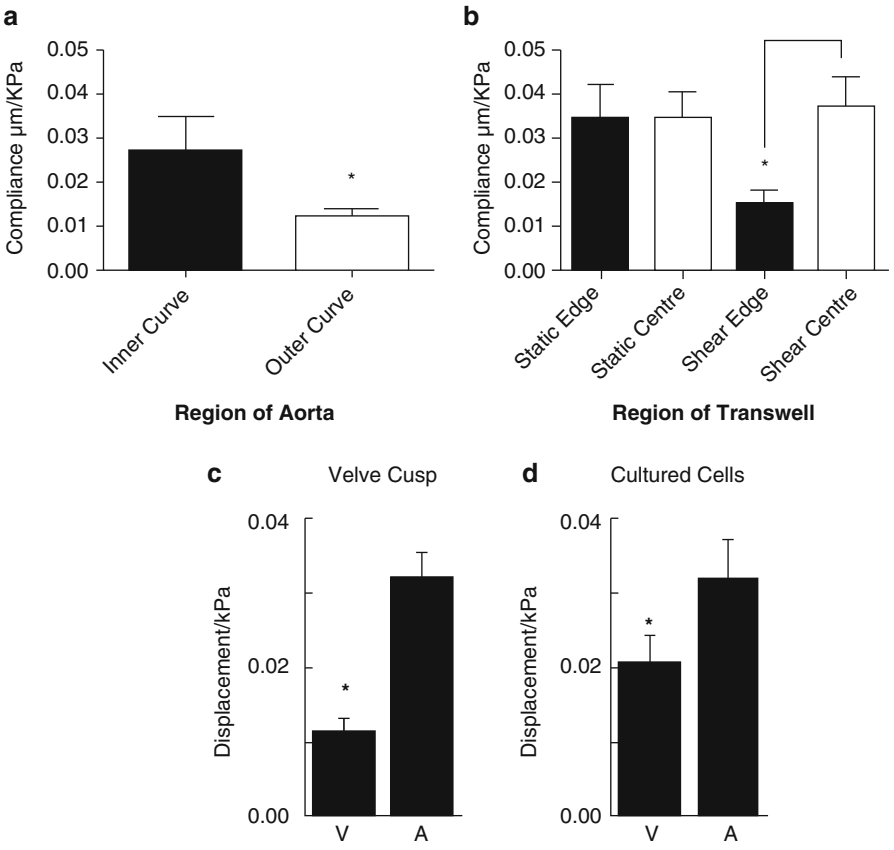

Fig. 12 Compliance measurements of different endothelial cells. Compliance of cells of the inner and outer curvatures of the ascending aorta (**a**) and of cultured aortic endothelial cells under different shear conditions (**b**) (* P = 0.01). Compliance measurement of endothelial cell on freshly isolated valve cusps (**c**) or in cultured cells (**d**) from the ventricular (V) and aortic (A) side of valve cusps (* P = 0.05). Figure modified with permission from [10, 11]

valve were relatively stiffer, whereas cells on aortic surface deformed more for the same applied pressure and were significantly softer. These cells when cultured and subjected to similar experiments also showed similar pattern and magnitude of cell compliance. Similarly, endothelial cells from different regions of aorta have different compliance depending upon the kind of shear forces they are subjected to [10].

Cell Volume Measurements by SICM

Volume of cells can change under many physiological and pathophysiological conditions. To calculate cell volume many methods have been proposed in the past [26–28]. One of the most advanced technique uses scanning laser confocal microscope [29] but it is limited by photodynamic damage and the need of specimen preparation prior to measurement.

On the other hand SICM can successfully measure cell volumes between 10^{-19} and 10^{-9} L [6] and without the need of any fluorescent markers or cell preparation. The SICM measures volume by integrating the raster image (Z-displacement) in X and Y directions, of the whole cell assuming that the entire cell's basal surface is in close contact with the dish/substrate and therefore is flat at the level of the dish. As a reference, the Z position of the pipette touching the dish/substrate is measured. The software can then integrate the area in X-Y direction giving the value for cell volume. With this method a comparison of cell volume between healthy and hypertrophic cardiomyocytes has been made [24]. In this particular experiment neonatal cardiomyocytes were isolated and cultured and then were subjected to hypertrophic stimulus which led to increase in cell volume and size. In a similar manner cell size of any cell on a flat substrate can be estimated with SICM.

Summary

SICM is the current state of the art super resolution microscopy technique of choice to study topography of biological cells. This non-contact microscopy offers several advantages over other comparable techniques like atomic force microscopy. The cells can be imaged without any preparation at an unprecedented resolution. The sample is well preserved during imaging and experiments of longer duration in real time can be performed because of non-optical nature of the technique. Combining SICM with various other techniques like patch-clamp, FRET and confocal microscopy has provided researchers with exceptional tools to probe cell structure and function concurrently at a resolution never achieved before. Existing and potential applications of SICM are described in Fig. 13. However, SICM has the limitation of imaging only the topography of cells, it cannot provide information on the interior compartments of cells like scanning electron microscopy. The potential of SICM is best exploited by combining it with other techniques. SICM alone can only provide the information on the surface structure but combining it with other techniques can provide information on local signaling or local structural properties.

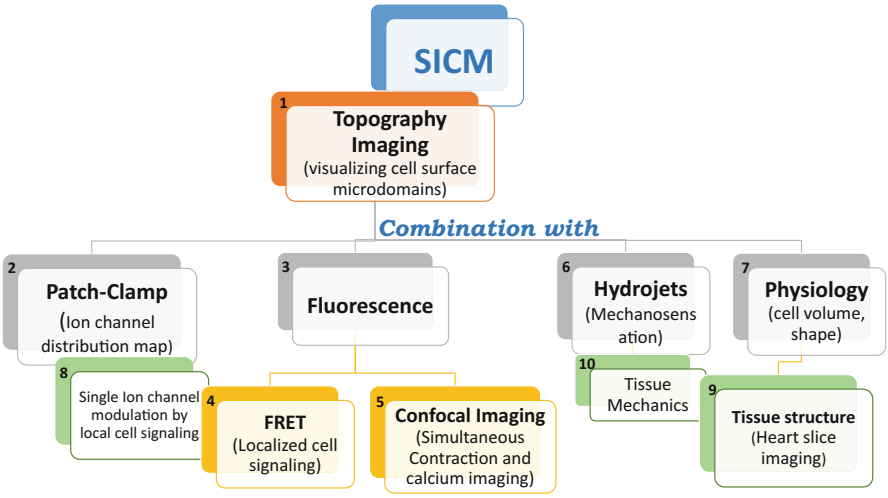

Fig. 13 Existing and potential applications of SICM. The foremost application of topography imaging (1) can be combined (combination techniques in grey) with patch-clamp (2) to study spatial distribution of ion channels on the cardiomyocyte surface. (3) SICM has been combined with fluorescence techniques (in yellow) like FRET (4) to study local cAMP signaling and laser confocal microscopy (5) to image calcium transients concurrently with contraction of the cardiomyocytes. When the SICM pipette is connected to a pressure pump it can function as a hydrojet (6) used to study mechano-sensitive properties like compliance of single cells. SICM images can be directly used to calculate physiology parameters (7) like cell volume and shape. In future one can further explore opportunities (in green) for example to combine SICM with patch clamp and FRET (8) to investigate the direct role of β-adrenergic signaling on the function and location of calcium channels. Further, tissue structure like heart slices (9) can be imaged and mechanical properties of the cells can be studied in a tissue environment (10)

References

1. Hansma PK, Drake B, Marti O, Gould SA, Prater CB. The scanning ion-conductance microscope. Science. 1989;243:641–3.
2. Gu Y, Gorelik J, Spohr HA, Shevchuk A, Lab MJ, Harding SE, et al. High-resolution scanning patch-clamp: new insights into cell function. FASEB J. 2002;16:748–50.
3. Korchev YE, Bashford CL, Milovanovic M, Vodyanoy I, Lab MJ. Scanning ion conductance microscopy of living cells. Biophys J. 1997;73:653–8.
4. Korchev YE, Milovanovic M, Bashford CL, Bennett DC, Sviderskaya EV, Vodyanoy I, et al. Specialized scanning ion-conductance microscope for imaging of living cells. J Microsc. 1997;188:17–23.
5. Korchev YE, Raval M, Lab MJ, Gorelik J, Edwards CR, Rayment T, et al. Hybrid scanning ion conductance and scanning near-field optical microscopy for the study of living cells. Biophys J. 2000;78:2675–9.
6. Korchev YE, Gorelik J, Lab MJ, Sviderskaya EV, Johnston CL, Coombes CR, et al. Cell volume measurement using scanning ion conductance microscopy. Biophys J. 2000;78:451–7.
7. Novak P, Li C, Shevchuk AI, Stepanyan R, Caldwell M, Hughes S, et al. Nanoscale live-cell imaging using hopping probe ion conductance microscopy. Nat Methods. 2009;6:279–81.

8. Gorelik J, Yang LQ, Zhang Y, Lab M, Korchev Y, Harding SE. A novel Z-groove index characterizing myocardial surface structure. Cardiovasc Res. 2006;72:422–9.
9. Lyon AR, MacLeod KT, Zhang Y, Garcia E, Kanda GK, Lab MJ, et al. Loss of T-tubules and other changes to surface topography in ventricular myocytes from failing human and rat heart. Proc Natl Acad Sci U S A. 2009;106:6854–9.
10. Potter CM, Schobesberger S, Lundberg MH, Weinberg PD, Mitchell JA, Gorelik J. Shape and compliance of endothelial cells after shear stress in vitro or from different aortic regions: scanning ion conductance microscopy study. PLoS One. 2012;7:e31228.
11. Miragoli M, Yacoub MH, El-Hamamsy I, Sanchez-Alonso JL, Moshkov A, Mongkoldhumrongkul N, et al. Side-specific mechanical properties of valve endothelial cells. Am J Physiol Heart Circ Physiol. 2014;307:H15–24.
12. Calebiro D, Nikolaev VO, Persani L, Lohse MJ. Signaling by internalized G-protein-coupled receptors. Trends Pharmacol Sci. 2010;31:221–8.
13. Wozniak M, Keefer JR, Saunders C, Limbird LE. Differential targeting and retention of G protein-coupled receptors in polarized epithelial cells. J Recept Signal Transduct Res. 1997;17:373–83.
14. Scott JD. A-kinase-anchoring proteins and cytoskeletal signalling events. Biochem Soc Trans. 2003;31:87–9.
15. Bhargava A, Lin X, Novak P, Mehta K, Khorchev Y, Delmar M, et al. Super-resolution scanning patch-clamp reveals clustering of functional ion channels in the adult ventricular myocyte. Circ Res. 2013;112:1112.
16. Novak P, Gorelik J, Vivekananda U, Shevchuk AI, Ermolyuk YS, Bailey RJ, et al. Nanoscale-targeted patch-clamp recordings of functional presynaptic ion channels. Neuron. 2013;79:1067–77.
17. Gorelik J, Gu Y, Spohr HA, Shevchuk AI, Lab MJ, Harding SE, et al. Ion channels in small cells and subcellular structures can be studied with a smart patch-clamp system. Biophys J. 2002;83:3296–303.
18. Nikolaev VO, Bunemann M, Hein L, Hannawacker A, Lohse MJ. Novel single chain cAMP sensors for receptor-induced signal propagation. J Biol Chem. 2004;279:37215–8.
19. Nikolaev VO, Bunemann M, Schmitteckert E, Lohse MJ, Engelhardt S. Cyclic AMP imaging in adult cardiac myocytes reveals far-reaching beta1-adrenergic but locally confined beta2-adrenergic receptor-mediated signaling. Circ Res. 2006;99:1084–91.
20. Nikolaev VO, Moshkov A, Lyon AR, Miragoli M, Novak P, Paur H, et al. Beta2-adrenergic receptor redistribution in heart failure changes cAMP compartmentation. Science. 2010;327:1653–7.
21. Lab MJ, Bhargava A, Wright PT, Gorelik J. The scanning ion conductance microscope for cellular physiology. Am J Physiol Heart Circ Physiol. 2013;304:H1–11.
22. Shevchuk AI, Gorelik J, Harding SE, Lab MJ, Klenerman D, Korchev YE. Simultaneous measurement of Ca2+ and cellular dynamics: combined scanning ion conductance and optical microscopy to study contracting cardiac myocytes. Biophys J. 2001;81:1759–64.
23. Harding SE, Ali NN, Brito-Martins M, Gorelik J. The human embryonic stem cell-derived cardiomyocyte as a pharmacological model. Pharmacol Ther. 2007;113:341–53.
24. Miragoli M, Moshkov A, Novak P, Shevchuk A, Nikolaev VO, El-Hamamsy I, et al. Scanning ion conductance microscopy: a convergent high-resolution technology for multi-parametric analysis of living cardiovascular cells. J R Soc Interface. 2011;8:913–25.
25. Sanchez D, Johnson N, Li C, Novak P, Rheinlaender J, Zhang Y, et al. Noncontact measurement of the local mechanical properties of living cells using pressure applied via a pipette. Biophys J. 2008;95:3017–27.
26. Crowe WE, Altamirano J, Huerto L, Alvarez-Leefmans FJ. Volume changes in single N1E-115 neuroblastoma cells measured with a fluorescent probe. Neuroscience. 1995;69:283–96.
27. Farinas J, Kneen M, Moore M, Verkman AS. Plasma membrane water permeability of cultured cells and epithelia measured by light microscopy with spatial filtering. J Gen Physiol. 1997;110:283–96.

28. Kawahara K, Onodera M, Fukuda Y. A simple method for continuous measurement of cell height during a volume change in a single A6 cell. Jpn J Physiol. 1994;44:411–9.
29. Zhu Q, Tekola P, Baak JP, Belien JA. Measurement by confocal laser scanning microscopy of the volume of epidermal nuclei in thick skin sections. Anal Quant Cytol Histol. 1994;16:145–52.

Optical Sectioning Microscopy at 'Temporal Super-Resolution'

Katja Flügel, Qinghai Tian, and Lars Kaestner

General Introduction

Within the recent years several super-resolution microscopic methods were developed, where the super-resolution refers to bringing the optical resolution beyond the diffraction limit introduced by Ernst Abbe, which was believed to be a real limit for quite some time. The popularity of the method also in cardiac related research can be followed in the chapter 'Quantitative super-resolution microscopy of cardiac myocytes' in this book. In parallel to this spatial super-resolution progress, within the past two decades there was a dynamic development of high speed–high resolution imaging initially towards video-rate (30 frames per second, also referred to as 'real time'-imaging) but soon to ever increasing frame rates reaching the kHz order of magnitude these days. Many processes, especially those in excitable cells such as neurons and cardiomyocytes [1] or cells in flow like erythrocytes or leukocytes [2], require even higher temporal resolution to elucidate the kinetics of processes like the Excitation-Contraction Coupling (ECC). Such ultra high speed recordings still require a diffraction limited spatial resolution to correlate function and subcellular structures [3]. Within this chapter we review optical sectioning microscopy and their application in cellular cardiology. In this approach we focus on methods that allow to access any part of the cell, i.e. we exclude methods that are intrinsically limited to surface investigations like total internal reflection fluorescence (TIRF) microscopy [4] or scanning near field optical microscopy (SNOM) [5]. In similarity we exclude techniques that require several images to

K. Flügel · Q. Tian
Theoretical Medicine and Biosciences, Saarland University, Homburg/Saar, Germany

L. Kaestner (✉)
Theoretical Medicine and Biosciences, Saarland University, Homburg/Saar, Germany

Experimental Physics, Saarland University, Saarbrücken, Germany

L. Kaestner, P. Lipp (eds.), *Microscopy of the Heart*,
https://doi.org/10.1007/978-3-319-95304-5_2

calculate an image section such as deconvolution microscopy [6] or structured illumination microscopy [7] (e.g., Apotome.2, Zeiss, Jena, Germany).

Confocal Microscopy

The basic principle of laser scanning confocal microscopy is an optical sectioning of the specimen along the optical axis. This is achieved by excitation of a diffraction limited spot and excluding light originating from above or below the plane of focus by fixed pinholes or variable irises depending on the construction of the confocal microscope. The price one has to pay for the optical sectioning capabilities offered with this approach is that measurements can only be obtained at a single point. Hence confocal imaging is a scanning process that can be realised by numerous scanning concepts as outlined below.

Single Beam Options

In the very initial design of a confocal microscope, Marvin Minsky used to scan the sample, i.e. the microscope stage across a stationary light beam [8]. Although this is still commercially available, especially for single molecule applications (e.g., MicroTime 200, PicoQuant, Berlin, Germany), this scanning process is inherently too slow to be further considered in this chapter. The faster alternative is scanning a single laser beam across the specimen. This method is the widely used and popular standard approach. Single beam scanners are usually equipped with galvanometer-based scanning mirrors for both, the x- and the y-direction. While this keeps the scanning electronics and the acquisition algorithms reasonably simple, this method is still relatively slow because the mirrors have to be moved physically. While conventional scanners are usually limited to single-figure frames per second, latest developments like digital controlled scan mirrors in combination with water-cooled galvanometers (e.g., LSM 880, Zeiss, Jena, Germany) can reach similar frame rates as resonating mirrors (see below).

Another well-proved concept to an increased frame rate is to switch from conventional mirrors to resonating mirrors (at least in the more demanding x-direction). When doing this, frame rates can easily reach video or double video rate (e.g., TCS SP8, Leica, Mannheim, Germany or A1R+, Nikon, Tokyo, Japan). One of the major difficulties with such an approach is the fact that the scanning process is not linear, thus sinusoidal scanning has to be accounted for with rather complex optical and/or electronics designs for compensation. In practice this leads to a selection of the most 'linear part' of the sinusoidal scan resulting in a loss of more than two thirds of the scanning time. The combination of this loss with the high frame rate results in very short pixel dwell times (as low as 25 ns).

Yet another approach to further gain one order of magnitude of scanning speed is to substitute the x-scanning mirror by an **a**custo **o**ptical **d**eflector (AOD) crystal (e.g., VT-Eye, VisiTech, Sunderland, UK). This mass-free scanning pushes the frame rate up to several hundred Hertz. The price for this speed is a reduced spatial resolution.

Caused by the design of AOD-scanning, both x- and z-direction have a slightly decreased optical resolution. This is because the AOD operates wavelength dependent and can therefore, due to the Stokes shift of the fluorescent dyes, not be used for the de-scanning as it is usually implemented in confocal heads based on scanning mirrors. This lack of descanning results in a linear moving point of the emitted fluorescence instead of a stationary point as in conventional scanners. This linearly moving point at the level of the detector excludes the implementation of a pinhole but its' replacement by a slit. For this kind of devices the restriction in scanning speed in experiments is no longer the scanning mechanism itself but most often the amount of fluorescence light available and the viability of the cells like the cardiomyocytes.

Multi Beam Options

A totally different approach of increasing the frame-rate of confocal scanning is the idea of exciting with more than one beam simultaneously. This can be realised either by a linear array of points (a line) such as the swept field microscope (e.g., Opterra II, Bruker, Billerica, MA, USA) or by a two-dimensional array of points. Since the incarnations of the latter ones use several thousands of parallel scanning beams they are referred to as kilobeam-scanners. They have many advantageous properties that are essential for imaging the dynamic behaviour of cells like cardiomyocytes. These advantages comprise beside the high acquisition speed (as fast as the attached camera can capture images), high efficiency in terms of simultaneous imaging of thousands of beams, low bleaching and low photo toxicity [9]. These kilobeam-scanners are available in two versions: The historical first version is the Nipkow-disc system, which is based on a rotating disc with a specific pattern of pinholes originally invented, designed and built to code and transmit TV images [10]. This scanning principle was made popular some 20 years ago, when the first confocal scanning units became commercially available (CSU-10, Yokogawa, Tokyo, Japan). One of the major drawbacks of spinning disc systems when reaching ultra high speed imaging, is the synchronisation of the sectors of the rotating disc with the acquisition of the camera. A system where such a synchronisation is intrinsically implemented is the so-called 2D-array scanner (e.g., VT-Infinity IV, VisiTech, Sunderland, UK). In such a device the array of parallel laser beams generated by a microlens array is actively moved across the specimen. Here, in contrast to the Nipkow disc system, the microlens- and pinhole-arrays are stationary. The only moving part is a single mirror responsible for scanning and de-scanning on the front surface as well as rescanning the image across the detection camera on its back surface. A schematic drawing of the 2D-array scanner is provided in Fig. 1. This approach ensures absolute synchrony between the scanning and the detection side of the confocal head. This concept of the 2D-array scanner also includes changeable pinhole sizes for variable resolutions in the direction of the optical axis, a feature not found in current versions of Nipkow disc based systems. Furthermore, this 2D-array scanner is now also available in a spatial super-resolution version (resolution improvement by factor of 2) based on structured illumination (VT-iSIM, Visitech, Sunderland, UK) without compromising in the recording speed.

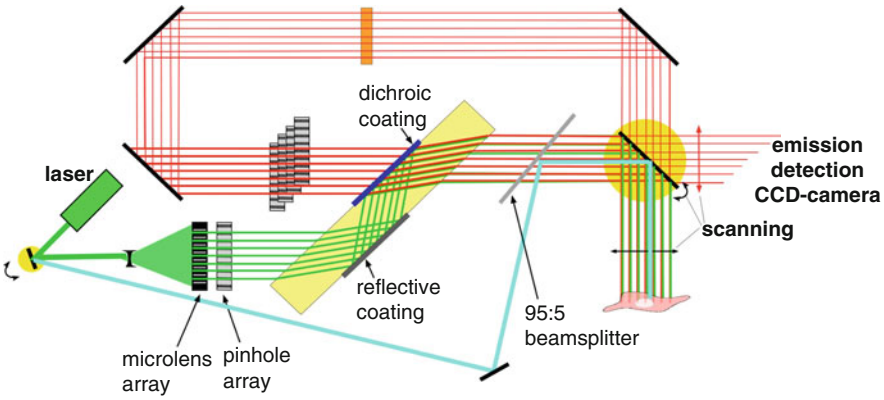

Fig. 1 A schematic design of the kilo-beam array scanner. A laser beam is widened, and a complementary stationary system consisting of a micro-lens array and a pinhole array generates a set of 50 × 50 beams. These beams pass through a dichroic mirror design that is insensitive to slight position changes and can be quickly changed by a motorised filter wheel. The beam bundle hits the major scanning mirror and serves three functions, scanning, de-scanning and, on its backside, re-scanning. Between the latter two functions, the emitted light passes the dichroic mirror and stationary pinhole array that consists of a set of five different pinhole sizes as well as an emission filter (orange). An additional beam path (cyan) illustrates the possibility of performing manipulations in a region of interest within the image, such as fluorescence redistribution after photobleaching (FRAP). This Figure is a reprint from Kaestner 2013 [3]

One of the most frequently used preconceptions about kilobeam scanners is the possible crosstalk between the pinholes, most prominent in thicker specimens. This will result in a diminished sectioning ability when recording 3D stacks for reconstructions [11]. However, recently kilobeam scanners with an increased distance between the pinholes became commercially available (e.g., CSU-W1, Yokogawa, Tokyo, Japan).

Beside the "true" confocal point and multi point scanner there is a variant available that inherently bears high-speed recordings: Slit-scanners do not use an individual point, but an entire line for excitation. Consequently the pinhole is replaced by a slit. The idea is to gain acquisition speed (matching the AOD-driven scanner) by sacrificing some of the resolution. This technique is currently not commercially available.

Analysis Algorithms

As outlined above, researchers are technically able to follow fast subcellular signalling in living cells, such as ECC in cardiac myocytes [12]. Decreasing the single pixel dwell times and concomitant decreases in the signal-to-noise ratio have limited the progress. However, scientific interest is not limited to the occurrence of Ca^{2+}-signals per se but also focuses on where, how much and how fast the Ca^{2+} increases occur because the signalling information is encoded in all of these properties

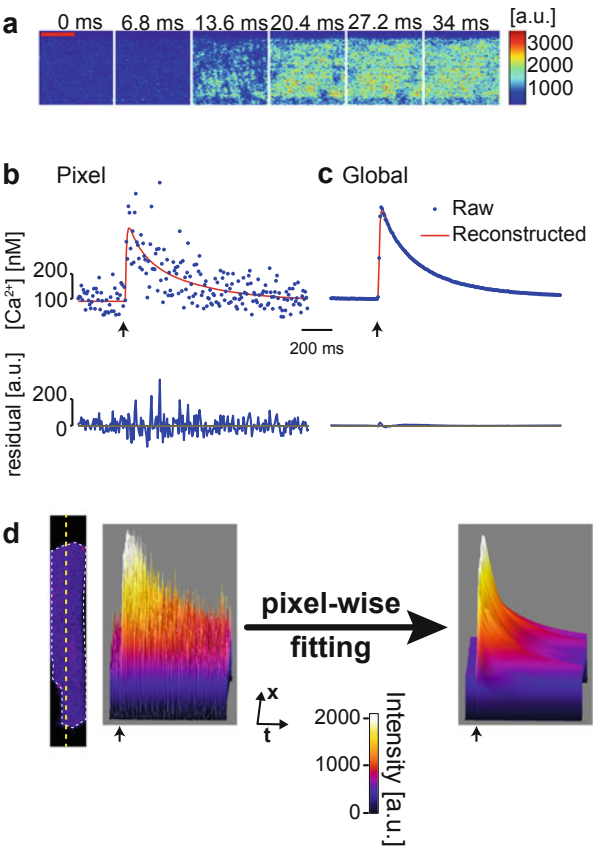

Fig. 2 Pixel Wise Fitting of fast 2D confocal data over time. (**a**) Raw images of 2D confocal data during the upstroke phase of an electrically evoked Ca^{2+} transient in a single rat ventricular myocyte loaded with fluo-4. Scale bar: 10 µm. (**b**) Upper panel: plot of the single-pixel fluorescence over time (blue dots) and the single-pixel PWF data (red line). Lower panel: plot of the residual over time for the single-pixel data. (**c**) The same plots as in (**b**) but for globally averaged fluorescence data. (**d**) Surface representation of the pseudo-linescan data along the yellow dashed line of the cell image for raw data (left panel) and after PWF (right panel). The arrows mark the time point of the electrical stimulation. This figure is reproduced from [26], with permission from Wolters Kluwer

[13]. Although the analysis of the 'where' can still be achieved using data with low signal-to-noise ratios, quantitative analysis, such as determining 'how much' and 'how fast', requires data with high signal-to-noise levels. Image quality could be improved by sacrificing a spatial dimension [14], but so-called linescan imaging does not appear to adequately capture all of the necessary spatial aspects of cardiac ECC because a single line only represents approximately 1.5% of the entire confocal cross section. Figure 2a depicts typical raw images from confocal recordings of a cardiomyocyte during the onset of an electrically evoked Ca^{2+} transient that was acquired at a frame rate of 146 Hz. It appears obvious from the individual images (Fig. 2a) and from the plot of the single-pixel fluorescence over time (Fig. 2b, blue dots) that single-pixel data are extremely noisy (signal coefficient of variation: 43% at baseline Ca^{2+}). Within such data, several sources of noise limit the detailed analysis of the spatiotemporal aspects of Ca^{2+} signalling and render interpretation difficult. To overcome such restrictions analysis algorithms were developed, such as the pixel wise fitting as outlined for Ca^{2+} transients in Fig. 2c. Thus, the entire Ca^{2+} transient image stack was reconstructed and compared with the raw data (Fig. 2d).

Examples from Cardiac Ca^{2+}-Handling

The pixel-wise fitting provides, for example, new mechanistic insights in a phenomenon called Ca^{2+} transient alternans, which is the cellular equivalent of T-wave alternans in the ECG that is associated with a plethora of disease situations [15, 16]. Figure 3 shows the comparison of manifested Ca^{2+} alternans (right column) with the period preceding these macroscopic alternans (left column) in rat myocytes. For Fig. 3a–c, left column, no obvious changes occurred relative to the 'healthy' situation. In the macroscopic alternans condition, a restricted response is evident in only part of the myocytes. Despite this difference, one can find coupling sites (Fig. 3a, yellow arrows) that displayed alternating amplitudes of microscopic Ca^{2+} transients (Fig. 3d). The red traces represent the local Ca^{2+} transients as a result of

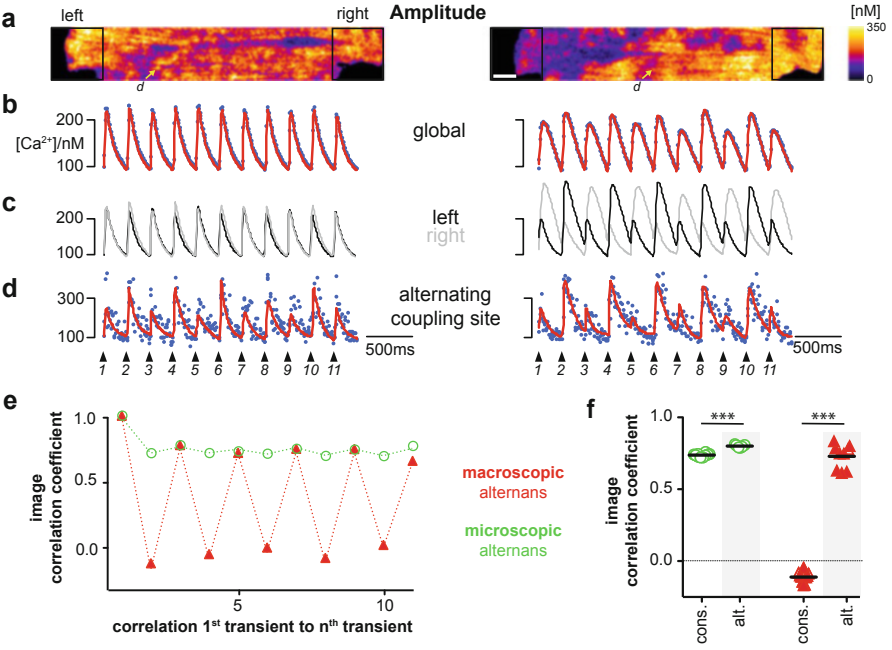

Fig. 3 Pixel Wise Fitting analysis revealed microscopic and macroscopic alternans in cardiac myocytes. Rat ventricular myocytes were loaded with fluo-4 and subjected to a step-wise increase in the stimulation frequency from 1 to 4 Hz [27]. The left column depicts the results of the analysis shortly after the increase in frequency, and the right column shows the results associated with the severe global, macroscopic alternans at a later time point. (**a**) The amplitude of the PWF. Scale bar: 10 µm. (**b**) The raw (blue dots) and reconstructed global Ca^{2+} transients (red trace). (**c**) The average of signals from the regions marked with black boxes in (**a**). (**d**) The single-pixel data (arrows in (**a**); raw: blue dots; reconstructed: red line). (**e**, **f**) Image correlation analysis for the distribution of the amplitude for microscopic (green) and macroscopic (red) alternans. For a detailed description, please see the text. These results were representative of seven ventricular myocytes that were studied under identical conditions. This figure is reproduced from [26], with permission from Wolters Kluwer. A more detailed comparison between the microscopic and macroscopic alternans is provided in a supplementary video 2 in the original publication [26]

PWF. The behaviour of those Ca^{2+} transients preceding the macroscopic alternans was called microscopic alternans. Quantification of the alternating behaviour was achieved by calculating the correlation coefficient between the amplitude distribution images (as depicted in Fig. 3a) of the first and all successive transients (Fig. 3e). Although the correlation was slightly but significantly changed between the consecutive and alternating transients during microscopic alternans (marked in green circles; Fig. 3f), the macroscopic alternans resulted in an alternation between large positive and negative values for the image correlation coefficient (marked in red triangels, Fig. 3e, f). These data revealed quantitative information about the subtle details of ECC in cardiac myocytes during the onset of alternans.

Going further into details, it would be desirable to monitor the activity of individual ECC sites (couplons), especially since plasmalemma and sarcoplasmic reticulum membrane calcium channels are important determinants of the heart's performance. The astronomer's CLEAN algorithm [17] initially designed to observe individual stars in a galaxy was recently applied to fast confocal images of cardiac myocytes and named CaCLEAN [1]. This algorithm was shown to untangle the fundamental characteristics of ECC couplons by combining the known properties of calcium diffusion. CaCLEAN empowers the investigation of fundamental properties of ECC couplons in beating cardiomyocytes without pharmacological interventions. Upon examining individual ECC couplons at the nanoscopic level, their roles in the negative amplitude-frequency relationship and in β-adrenergic stimulation, including decreasing and increasing firing reliability, respectively, was reviled as depicted in Fig. 4A, B. CaCLEAN combined with 3D confocal imaging of beating cardiomyocytes provides a functional 3D map of active ECC couplons (on average, 17,000 per myocyte) as shown in Fig. 4C. In future, CaCLEAN will enlighten the ECC-couplon-remodelling processes that underlie cardiac diseases.

Non-linear Microscopy

The idea behind non-linear microscopy (NLM) is to condense the laser energy in time (femto-second pulses) and space (focus) such that the energy density in the focus becomes so high that the photons and the molecule of the sample interact in a non-linear manner. This NLM can either be based on fluorescence (multi photon microscopy) or on the interaction with so called non-linear materials leading to a frequency multiplication like second harmonic generation (SHG) or third harmonic generation (THG).

Multi Photon Microscopy

In multi photon microscopy, the dye absorbs two (or multiple) photons simultaneously. Since the underlying molecular excitation process remains the same, both photons have to deliver approximately half (or other fractions depending on the multiplicity of excitation) of the energy. Half of the energy translates into a doubling of the wavelength, which explains why far red and infrared light emitting Titan:Sapphire lasers are

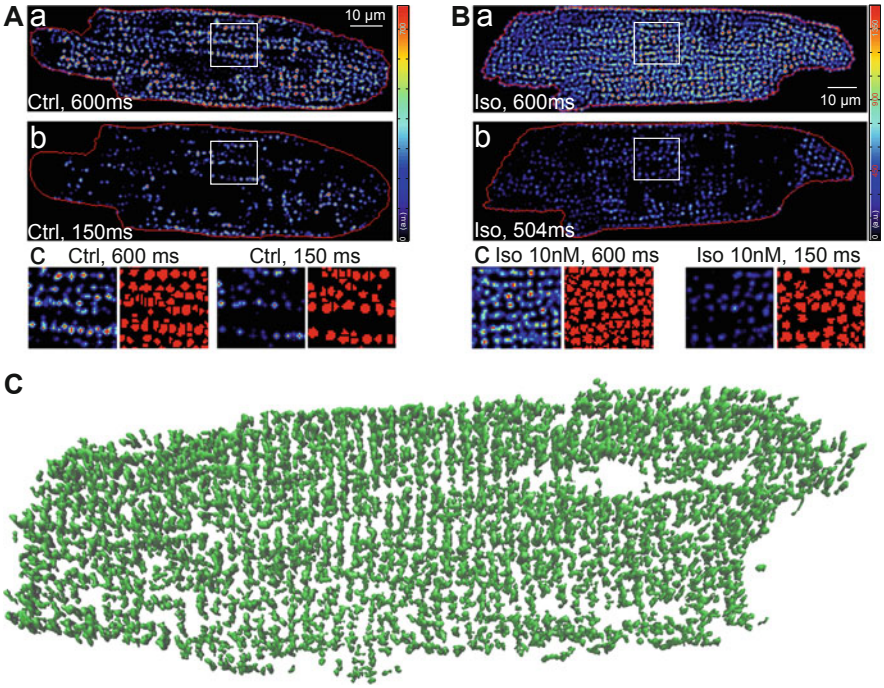

Fig. 4 Behavior of ECC couplons at variable stimulation frequencies and during β-adrenergic stimulation. Rat ventricular myocytes were electrically paced into steady state at the stimulation intervals given in the images. (**A**) The resulting CaCLEAN ECC couplon maps at 600 ms (**a**) and 150 ms (**b**) stimulation intervals under control conditions (Ctrl). Subcellular regions highlighted with white boxes were replotted at a high magnification (**c**) alongside with segmented ECC couplon sites (**c**, red). (**B**) Data similar to those in (**A**) but in a ventricular myocyte following β-adrenergic stimulation (10 nM isoproterenol, 5 min) (Iso). (**C**) Three-dimensional reconstruction of active ECC couplons in a naïve rat ventricular myocyte. Panels (**A**) and (**B**) are reproduced from [1], with permission from eLife Sciences Publications, Ltd

popular. Thus, if the chromophore requires, e.g., single photon excitation at 450 nm, the equivalent two-photon excitation wavelength would be 900 nm. For other multi photon processes this shift is multiplied by higher factors. One should be aware that the absorption cross-section of single photon and multi photon excitation can be quite different. The basic advantage of multi photon microscopy compared to single photon confocal imaging is reduced photobleaching in out-of-focus planes, since the multi photon excitation is restricted to the focal plane. For a thorough discussion of multi photon microscopy see [18]. Here, we solely mention two additional significant advantages of multi photon excitation. (a) Deeper penetration depth. Since excitation can be performed with red, far-red or even infrared light the penetration of the excitation light in living tissue is considerably increased in comparison to shorter wavelengths. Hence it is possible to image single cardiac myocytes in the intact heart as outlined in

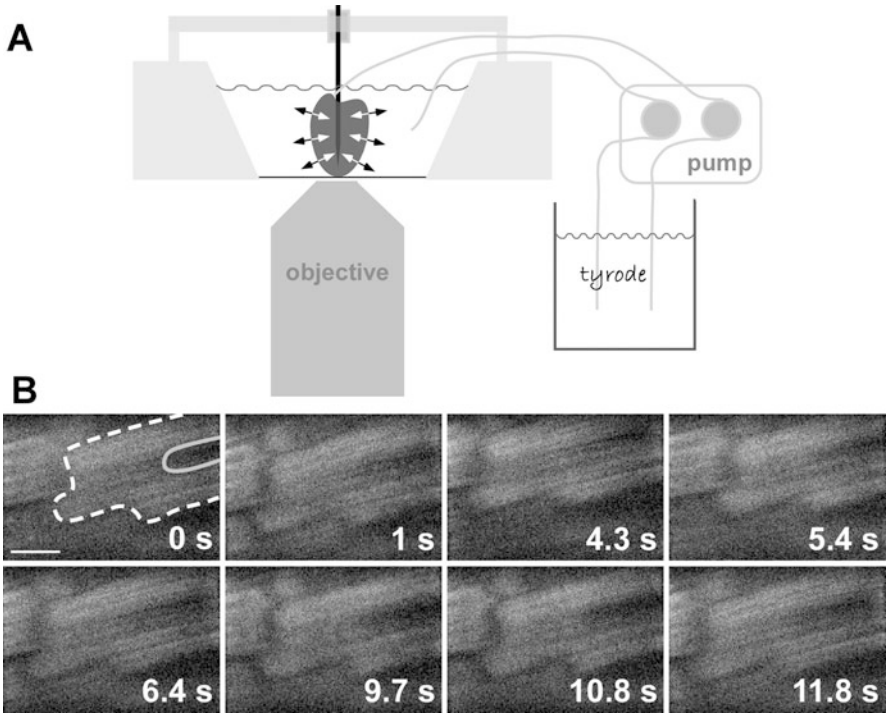

Fig. 5 Imaging of a perfused beating mouse heart. Panel (**A**) shows the design of the measuring chamber for use with an inverted microscope. In order to minimise motion artefacts the heart was fixed by a needle (black vertical line in panel A), the needle was placed exactly in the optical axis of the microscope objective. Since the heart was 'beating around' the needle (illustrated by the arrows) a virtually motion-free image could be recorded. A peristaltic pump was employed for continuous retrograde perfusion. Panel (**B**) depicts representative autofluorescence images of an identified myocyte throughout a recording period of 12 s (at video-rate). The scale bar represents 10 μm. The shape of the cell and the nucleus is highlighted in the first image by the dashed white line and the solid grey line, respectively. This Figure is reproduced from Kaestner and Lipp 2007 [28]

Fig. 5. It should be mentioned here that the maximal penetration depth is tissue dependent. One still has to consider that emission light scattering becomes more prominent with increasing penetration depth. (b) Intrinsic sectioning. As described above, the 'multi photon effect' is restricted to the core of the excitation light focus in the specimen due to the non-linear excitation probability. From this it follows that in contrast to single photon confocal scanners that employ optical sectioning on the 'emission' side (spatial filter, the pinhole(s)), scanners using multi photon excitation already generate sectioning on the excitation side. For single point scanners this translates into their liberation from de-scanning; all light emitted, originates exclusively from the excitation volume that is diffraction limited and thus light collection does not require the ability for spatial discrimination. Similar to single beam scanners, in multi photon microscopy the construction of a 2D image is also realised by a scanning

process. In the easiest of all cases scanning is performed by means of two galvanometer controlled mirrors with all the limitations discussed above. The application of fast AOD crystals for x-scanning is certainly more complex when using pulsed femtosecond light sources, because diffraction of AODs is wavelength dependent and fs-pulsed lasers produce a spectral band (e.g., with 75 fs pulses the bandwidth of the resulting spectrum can reach around 10 nm). This means that the degree of diffraction of the excitation light will be different for the 'red' and the 'blue' components of the excitation spectrum. Nevertheless, multiple approaches exist that offer possible solutions [19, 20]. In addition to that a multi photon multi point multi plexed scanner with up to 128 parallel excitation points arranged in a line is commercially available (TriM Scope II, LaVision BioTec, Bielefeld, Germany), where acquisition speed is practically limited by the frame rate of the camera attached.

SHG Imaging

SHG imaging can be performed in reflective and in transmission mode. This depends on the properties of the particular 'interaction material' as well as on the sample preparation. In most cases SHG imaging relies on intrinsic structures and hence no additional staining of cells or tissue is required. For example collagens give a strong reflective SHG signal. Since collagens are built up in the process of fibrosis and are also part of the vessels such parameters can be investigated in tissue sections, e.g., for human cardiac appendages as outlined in Fig. 6.

Another structure in cardiac myocytes providing a strong SHG-(transmission) signal is myosin [21], which can be used to measure sarcomere length [22] and hence to follow cellular contraction. This approach is especially interesting for stem cell derived cardiomyocytes, where the contractile structures are not as well organised as in adult cardiomyocytes and hence the classical cell length measurements [23] fail. Such SHG-imaging of contracting stem-cell derived cardiomyoctes can very well be used for functional phenotyping.

Light-Sheet Imaging

Light sheet imaging also known as selective plane imaging (SPIM) relies on the illumination of the sample by a light sheet perpendicular to the optical axis of the microscope. The recent revival of that technique [24] is based on a sample holder with a rotational axis parallel to the gravitation field that enables rotation while keeping the sample itself distortion-free. The implementation of this design became commercially available (Lightsheet Z.1, Zeiss, Jena, Germany). The serial optical sectioning is realised by moving the sample through the light sheet and for every position an image is collected. Although the lateral resolution is lower than with confocal techniques the biggest advantage of light sheet imaging is its ability to reach the same optical resolution in all three spatial dimensions. Similar but not identical to multi photon excitation light sheet excitation happens exclusively in

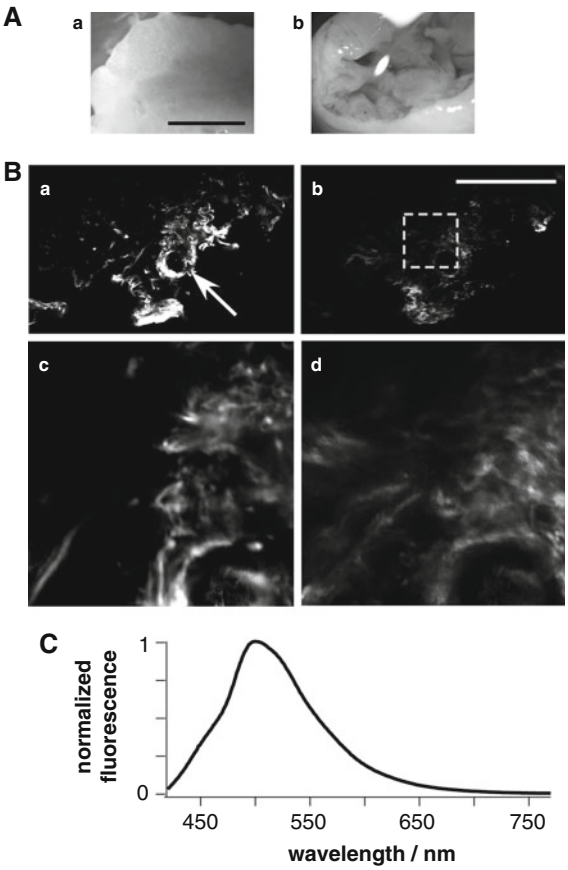

Fig. 6 Non-linear imaging of human auricles. Panel (**A**) shows the macroscopic appearance of the atrial appendages; (**Aa**)—from outside the heart (epicardial side) and (**Ab**) from inside the heart, where the surgical cut was performed. The scale bar represents 5 mm. Panel (**B**) depicts laser scanning images taken from inside an atrial appendage as shown in image (**Ab**). Images (**Ba**) and (**Bc**) display the SHG reflection signal indicating elastin and collagen fibres of the extracellular matrix, while images (**Bb**) and (**Bd**) represent the same image section viewed at the autofluorescence wavelengths. The spherical structure in (**Ba**) marked by the white arrow resembles a small vessel. The dashed square in image (**Bb**) shows the section that was scanned at a higher magnification for panels (**Bc**) and (**Bd**). The scale bar represents 50 μm for panels (**Ba**) and (**Bb**), and 10 μm for panels (**Bc**) and (**Bd**). Panel (**C**) provides a fluorescence spectrum of the autofluorescence from panels (**Bb**) and (**Bd**) upon excitation with 410 nm light. This Figure is reproduced from Kaestner and Lipp 2007 [28]

the focal plane, avoiding bleaching outside the focus. When imaging 3D-stacks, acquisition speed is limited, however, when imaging, e.g., dynamic processes, in a single plane, speed is only determined by the operation of the camera. Heavy computational power has to be invested before a 3D-reconstruction can be visualised, but also for this task reliable solutions are commercially available, e.g.,

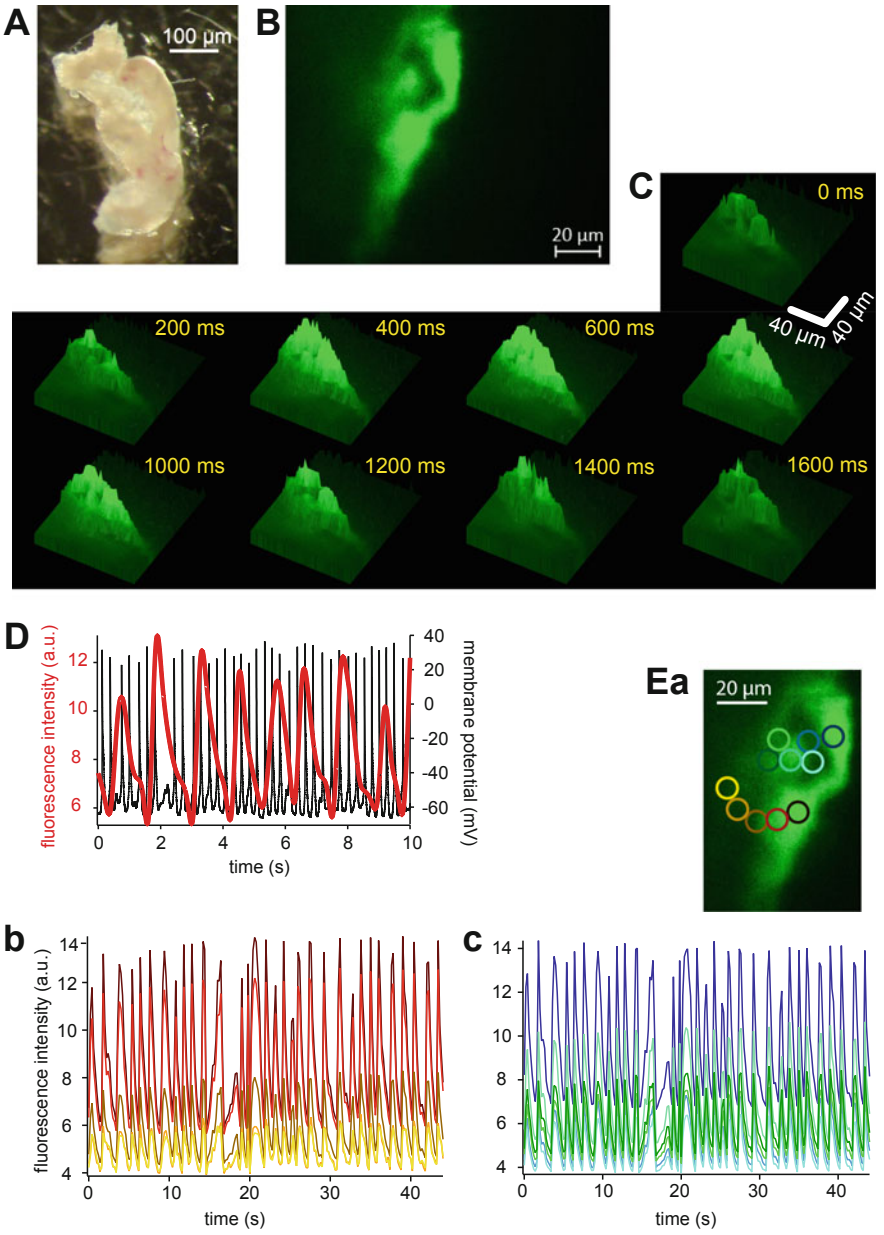

Fig. 7 Light sheet imaging of Ca^{2+}-signals in a sinoatrial node (SAN). (**A**) depicts a white light image of a SAN isolated from a mouse with tissue-specific expression (HCN4 KiT Cre) of the genetically encoded Ca^{2+} sensor GCaMP3. (**B**) shows a representative Light sheet recording of the SAN specific expression of GCaMP3 using a Zeiss Z.1 microscope. (**C**) presents a time series of surface plots of Ca^{2+}-signals of the autonomously beating SAN depicted in panels (**A**) and (**B**). The fluorescence activity of particular (pacemaker) cells can be identified. (**D**) compares the time course of the Ca^{2+}-signals of the SAN with action potentials measured by patch-clamp in isolated

Vision4D (arivis, Rostock, Germany). Although manipulation of the sample (e.g., by patch-clamp) is more complicated or impossible, the placement of the sample in 3D is easier and has more degrees of freedom than placing a sample on a coverslip like in conventional microscopy. An example where such an option is advantageous is given in Fig. 7, where a sinoatrial node (SAN) expressing a genetically encoded Ca^{2+} indicator (GCaMP3, compare chapter 'Optogenetic Tools in the Microscopy of Cardiac Excitation-Contraction Coupling'), was isolated from a mouse heart. In the current implementation of light-sheet imaging, excitation manipulation still needs to be synchronised with the camera, which is a major limitation of the acquisition speed that has the potential to increase in future.

Conclusions

Speaking about (diffraction limited) imaging speed, temporal resolution can always be increased by sacrificing spatial resolution. The first step in this concept would be the reduction of the number of pixels per image. This can be realised either by limiting the overall size of the image or by binning adjacent pixels or at its extreme by reducing image sizes to individual lines (line-scans). Going further—if the entire fluorescence signal of the microscope is detected in a point detector we speak about confocal spot measurements [25]. In this case sampling rates can be as high as several MHz. Nonetheless, even without any special optical spatial resolution, e.g., video imaging, the functional spatial resolution can originate from the experimental design (see FRET in the chapter 'Optogenetic Tools in the Microscopy of Cardiac Excitation-Contraction Coupling') and does not only exceed the diffraction limit but optical super-resolution.

As we described in this chapter, particular experimental designs in cellular cardiology exploring the cellular and molecular regulation of ECC, may require special high speed sectioning microscopy methods. All of them bear advantages and disadvantages and therefore need to be carefully selected, proscribing a general recommendation in favour of a particular technology and it's implementation.

Fig. 7 (continued) SAN-cells showing a higher frequency relative to the intact SAN. (**E**) provides a spatio-temporal analysis of Ca^{2+}-signals in the autonomously beating SAN. (**a**) shows the regions of interest (ROIs) analysed. ROIs are arranged in two groups with traces depicted in (**b**) and (**c**). The colour code of the ROIs in (**a**) corresponds with the colour traces in (**b**) and (**c**). The acquisition rate is too low to identify particular spots of Ca^{2+}-signal origin or a spatio-temporal spreading of the signals. However, there is a clear indication of an interconnection of the different ROIs, even between the two grouped ones, because any kind of arrhythmic episodes or major intensity changes are evident in all ROIs

References

1. Tian Q, Kaestner L, Schröder L, Guo J, Lipp P. An adaptation of astronomical image processing enables characterization and functional 3D mapping of individual sites of excitation-contraction coupling in rat cardiac muscle. Elife. 2017;6:665.
2. Quint S, et al. 3D tomography of cells in micro-channels. Appl Phys Lett. 2017;111:103701.
3. Kaestner L. Calcium signalling. Approaches and findings in the heart and blood. New York, NY: Springer; 2013.
4. Poulter NS, Pitkeathly WTE, Smith PJ, Rappoport JZ. The physical basis of total internal reflection fluorescence (TIRF) microscopy and its cellular applications. Methods Mol Biol. 2015;1251:1–23.
5. Micheletto R, et al. Observation of the dynamics of live cardiomyocytes through a free-running scanning near-field optical microscopy setup. Appl Optics. 1999;38:6648–52.
6. Carrington W, Fogarty K. 3-D molecular distribution in living cells by deconvolution of optical sections using light microscopy. In: Foster KR, editor. Proceedings of 13th Annual Northeast Bioengineering Conference. New York, NY: IEEE Press; 1987. p. 108–11.
7. Neil MA, Juskaitis R, Wilson T. Method of obtaining optical sectioning by using structured light in a conventional microscope. Opt Lett. 1997;22:1905–7.
8. Minsky M. Microscopy apparatus. 1957.
9. Lipp P, Kaestner L. In: Hüser J, editor. High throughput-screening in drug discovery. Weinheim: Wiley-VCH; 2006. p. 129–49.
10. Nipkow P. Elektrisches teleskop. 1884.
11. Egner A, Andresen V, Hell SW. Comparison of the axial resolution of practical Nipkow-disk confocal fluorescence microscopy with that of multifocal multiphoton microscopy: theory and experiment. J Microsc. 2002;206:24–32.
12. Bers DM. Cardiac excitation-contraction coupling. Nature. 2002;415:198–205.
13. Berridge MJ, Bootman MD, Lipp P. Calcium--a life and death signal. Nature. 1998;395:645–8.
14. Tian Q, et al. Functional and morphological preservation of adult ventricular myocytes in culture by sub-micromolar cytochalasin D supplement. J Mol Cell Cardiol. 2012;52:113–24.
15. Weiss JN, Nivala M, Garfinkel A, Qu Z. Alternans and arrhythmias: from cell to heart. Circ Res. 2011;108:98–112.
16. Laurita KR, Rosenbaum DS. Cellular mechanisms of arrhythmogenic cardiac alternans. Prog Biophys Mol Biol. 2008;97:332–47.
17. Högbom JA. Aperture synthesis with a non-regular distribution of interferometer baselines. Astron Astrophys Suppl. 1974;15:417–26.
18. Denk W, Piston DW, Webb WW. In: Pawley JB, editor. Handbook of biological confocal microscopy. New York, NY: Plenum Press; 1995. p. 445–58.
19. Bouzid A, Lechleiter J. Laser scanning fluorescence microscopy with compensation for spatial dispersion of fast laser pulses. Opt Lett. 2006;31:1091.
20. Roorda RD, Miesenbock G. Beam-steering of multi-chromatic light using acousto-optical deflectors and dispersion-compensatory optics. 2002.
21. Plotnikov SV, Millard AC, Campagnola PJ, Mohler WA. Characterization of the myosin-based source for second-harmonic generation from muscle sarcomeres. Biophys J. 2006;90:693–703.
22. Boulesteix T, Beaurepaire E, Sauviat M-P, Schanne-Klein M-C. Second-harmonic microscopy of unstained living cardiac myocytes: measurements of sarcomere length with 20-nm accuracy. Opt Lett. 2004;29:2031–3.
23. Viero C, Kraushaar U, Ruppenthal S, Kaestner L, Lipp P. A primary culture system for sustained expression of a calcium sensor in preserved adult rat ventricular myocytes. Cell Calcium. 2008;43:59–71.
24. Huisken J, Swoger J, del Bene F, Wittbrodt J, Stelzer EH. Optical sectioning deep inside live embryos by selective plane illumination microscopy. Science. 2004;305:1007–9.
25. Parker I, Ivorra I. Confocal microfluorimetry of Ca^{2+} signals evoked in Xenopus oocytes by photoreleased inositol trisphosphate. J Physiol. 1993;461:133–65.

26. Tian Q, Kaestner L, Lipp P. Noise-free visualization of microscopic calcium signaling by pixel-wise fitting. Circ Res. 2012;111:17–27.
27. Aistrup GL, et al. Pacing-induced heterogeneities in intracellular Ca^{2+} signaling, cardiac alternans, and ventricular arrhythmias in intact rat heart. Circ Res. 2006;99:E65–73.
28. Kaestner L, Lipp P. Non-linear and ultra high-speed imaging for explorations of the murine and human heart. Prog Biophys Mol Biol. 2007;8:66330K-1–66330K-10.

Quantitative Super-Resolution Microscopy of Cardiomyocytes

Christian Soeller and Izzy D. Jayasinghe

Background

Cardiomyocytes are among the largest of animal cell types. At ~20 μm in typical width and ~100 μm in length, these cells are intrinsically organised to contract rapidly and in synchrony in response to electrical activation. This excitation-contraction coupling (EC coupling) process is achieved through the synchronised opening of the primary calcium (Ca^{2+}) release channels of the sarcoplasmic reticulum (SR)—the ryanodine receptors (RyRs) [1]. A series of tubular membrane invaginations of the surface sarcolemma, known as the t-tubules, are the primary sites of this Ca^{2+} release deeper within the cell where RyRs are organised into clusters in quasi-crystalline patterns [2, 3]. Flanked between the t-tubule membrane and the SR membrane at the dyadic cleft, the cytoplasmic portions of these giant (29 nm × 29 nm) Ca^{2+} channel [4] are opened by the Ca^{2+} that enters the cleft through the voltage-gated L-type Ca^{2+} channel (LCC). This process, known as Ca^{2+} induced Ca^{2+} release (CICR) crucially relies on the restricted diffusion and the consequently elevated concentration of the cleft Ca^{2+} [5]. Described in the theory of local control of EC coupling, the Ca^{2+} released via RyRs is likely a steep function of the dimensions of the dyadic cleft and the trigger Ca^{2+} concentration [6]. The synchronisation of the contraction also relies heavily on the effectiveness of this Ca^{2+} in reaching and activating the contractile machinery (which forms the

C. Soeller (✉)
Living Systems Institute, University of Exeter, Exeter, UK

Department of Physiology, University of Auckland, Auckland, New Zealand
e-mail: C.Soeller@exeter.ac.uk

I. D. Jayasinghe
Biomedical Physics, University of Exeter, Exeter, UK

School of Biomedical Sciences, University of Leeds, Leeds, UK

L. Kaestner, P. Lipp (eds.), *Microscopy of the Heart*,
https://doi.org/10.1007/978-3-319-95304-5_3

myofibrils). Early light and electron micrographs have demonstrated that t-tubules and dyads are, to this end, organised all around the myofibrils to minimise the typical diffusional distance of the released calcium [7–10].

It is becoming increasingly clear that this organisation of Ca^{2+} release sites is vital to the healthy performance of the myocyte as sub-cellular scale remodelling is observed during a range of cardiac pathologies with concurrent disruptions in the Ca^{2+} signalling and the contractility of myocytes [11–13]. Notably, these observations have included remodelling of the t-tubules (including alteration of the abundance of transverse and longitudinal tubules and complete loss of tubules) leading to RyRs being 'orphaned' [12, 14]. This disruption to the dyad structure and function have highlighted a few key questions: (i) what is the native structure of the Ca^{2+} release sites and the intrinsic distribution of RyRs in cardiac myocytes; (ii) how are the t-tubules organised in relation to these sites and what are the structural features that ensure local control; (iii) what are the structural biomolecules that maintain this dyad structure and (iv) how does the molecular structure of the dyad allow us to interpret the functional (e.g. Ca^{2+}) data from myocytes of healthy and failing hearts.

Issues with Conventional Optical Imaging for Cardiac Studies

Addressing these questions immediately exposed a number of technical challenges. Both Nyström's first micrographs of t-tubules in the rabbit myocardium (1897) and Veratti's drawings in 1901 of Golgi-stained t-system in various striated muscles [15] were performed with optical microscopy [16]. However, much of the discoveries that followed, including dyads, the 'feet' (RyRs) [8], the SR and their relationship to other vital components such as myofibrils and mitochondria were all demonstrated with electron microscopy (EM) [8]. While EM offered angstrom-level resolution, it typically lacked the contrast and the molecular specificity that could usually be achieved with targeted staining methods such as immuno-stains or organic dyes for fluorescence microscopy [9, 17]. Due to the high contrast and specificity that can be achieved conventional fluorescence microscopies were therefore useful for cell-wide imaging of specific protein distributions (e.g. RyR, LCC, contractile proteins) as well as cellular organelles and membrane topologies (e.g. t-system, SR, mitochondria) with sufficient contrast for quantifying co-localisation [18, 19] and three-dimensional reconstruction [9, 18, 20]. However, resolution in optical far field microscopies is limited by diffraction as described by the Abbe limit [21]. Virtually all of the structures that are central to the EC coupling within cardiomyocytes are therefore poorly resolved in conventional fluorescence micrographs. These include dyads, t-tubules (particularly in some animal species), the SR, caveolae, components of the contractile machinery/cytoskeleton and essentially all of the proteins that drive this mechanism.

Optical Super-Resolution Imaging

More recent developments in fluorescence microscopy methods, collectively known as super-resolution microscopies, have circumvented this limitation and can visualise structures that were previously not detectable or not resolved. Broadly, super-resolution microscopies can be classed into three categories: (i) stimulated emission depletion (STED) microscopy where the focal volume of laser excitation is effectively reduced by selectively deactivating all fluorophores but those within the very centre of the laser spot [22]; (ii) structured illumination microscopy (SIM) where the sample is illuminated iteratively with a variable pattern of light and the fringes of the Moiré pattern in the resulting images exploited to computationally generate a super-resolution image (see e.g. review by Jost and Heintzmann [23]); (iii) and single molecule localisation microscopy (SMLM) where the fluorescence is stretched out in time and individual markers are localised with high precision.

Optical Super-Resolution Techniques Roundup

SMLM techniques (commonly known by acronyms such as PALM [24] or STORM [25], see reviews [26–28]) broadly rely on the stochastic photoswitching of fluorophores or marker molecules within the sample so that only a small subset of all fluorochromes is active at any one time, at sufficiently low density to computationally determine their in situ localisation at nanometre-scale precision from non-overlapping single-molecule fluorescence spots. Compared to the commercially-implemented STED (although achievable resolution is rapidly improving) and SIM which offers resolution of ~120 nm in-plane and ~250 nm axially, the SMLM method has allowed a more substantial improvement in resolution (as fine as 30 nm in imaging cardiac myocytes [29, 30]). Perhaps more importantly, the relatively complex hardware and optical alignment required for STED and SIM can prove to be challenging in implementing these methodologies in home-built microscope systems when considering the modest (although for some applications entirely sufficient) improvement in resolution that is on offer. In comparison, SMLM is straightforward to implement with non-specialised hardware. In fairness, STED and SIM may yet hold clear advantages in SMLM in terms of speed and versatility of imaging both living and fixed myocytes (e.g. [31]), but in our hands SMLM has offered versatility in imaging both isolated myocytes as well as tissue sections with molecular specificity and sensitivity to quantify Ca^{2+} handling proteins (e.g. RyRs) at near single channel resolution. Further, the adaptability of commonly used fluorophores for SMLM has made it a popular choice as compared to STED and SIM which have typically required either highly bleach-resistant or self-replenishing fluorophores.

The cursory discussion above of the pros and cons of various optical super-resolution approaches is necessarily incomplete and there is clearly no one modality that is superior for all applications in cardiac imaging. As is not uncommon when using sophisticated imaging approaches various trade-offs need to be made and this

may require selection of different modalities for different experiments. An additional complication is the current rapid progress in this area with the advent of novel hybrid methods, new tricks and commercial implementations at a rapid pace.

With these caveats in mind, in this chapter will focus on SMLM, due to its robust implementation and widespread availability. We will review the implementation and application of SMLM to overcome limitations previously encountered with diffraction-limited optical microscopy methods in examining structures that are central for EC coupling. We will initially discuss some of the new insight into cardiac structure-function relationships obtainable with SMLM before focussing on the methodological considerations that enable high quality SMLM with cardiac samples.

Applications of SMLM to Cardiac Preparations

To illustrate the utility of SMLM for investigating cardiac preparations we discuss below a number of findings that are a direct consequence of the higher resolution and contrast provided by SMLM.

Novel Insights into the Distribution of RyRs in Myocytes

RyRs are found clustered within dyads and were previously observed as bright punctate densities in high-resolution immunofluorescence micrographs in both wide-field [17, 32, 33] and confocal microscopies [10, 34, 35]. Application of deconvolution for image enhancement only resulted in a moderate improvement [18]. This often required the analysis of these labelling densities as puncta, i.e. essentially featureless domains [18], or voxels [17, 19, 32, 33] which were insensitive to the intrinsic variations in orientation and three-dimensional complexities in the dyad structure [10]. One of the key features of such analyses were the larger inter-punctum nearest neighbour distances estimated from confocal data of RyR [10, 18] compared to the EM estimates [8], which were not entirely explained by the methodological differences (e.g. shrinkage in the dehydration of tissue). Fluorometric calibration of puncta intensities, however, demonstrated a large range of cluster sizes, 95% of which ranged between 120 and 260 RyRs in rat cardiomyocytes [10]. Close examination of the integrated fluorescence density in TIRF micrographs of RyR immunolabelling within peripheral dyads of rat ventricular myocytes (e.g. Fig. 1a) also revealed heterogeneity in the labelling density from cluster to cluster which was insufficiently explained by the expected stochastic variations of antibody binding [18]. Taken collectively, these observations were suggesting a sub-structure of the punctate RyR densities in diffraction-limited images that was more heterogeneous in size and/or shape.

The adaptation of dSTORM for imaging immunofluorescence of RyR within peripheral couplons of enzymatically isolated rat cardiomyocytes provided a number of novel observations [29, 30]. Areas of labelling seen before as featureless punctate

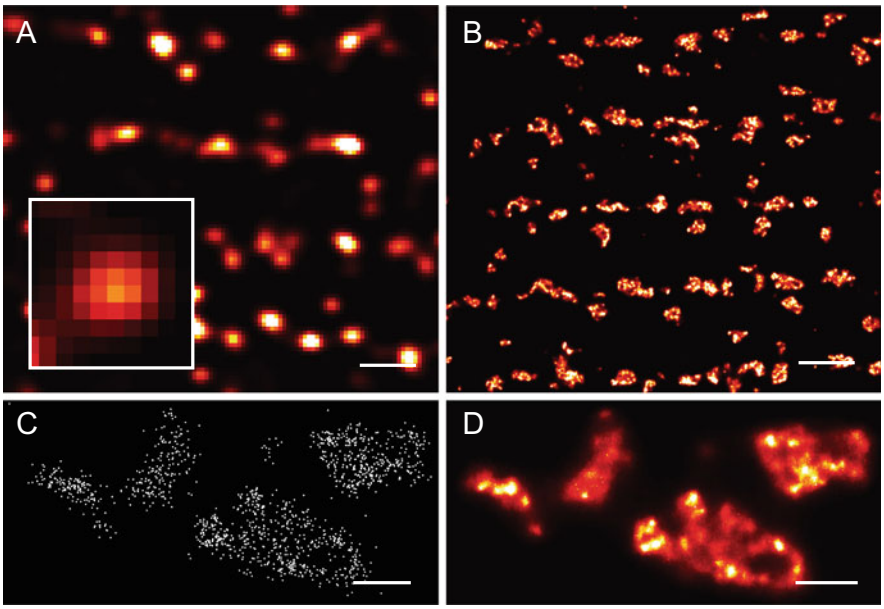

Fig. 1 Improved visualisation of RyR clusters within peripheral couplons of rat ventricular myocytes. (**a**) RyR immunolabelling imaged near the surface of rat ventricular myocytes with TIRF microscopy is typically punctate in morphology (magnified view in inset). (**b**) dSTORM image of the same region illustrates patches of RyR staining with varying sizes and shapes corresponding to the smooth punctate densities observed in the diffraction-limited image. (**c**) The magnified view reveals a small groups of RyR clusters corresponding to these patches as reported by single molecule localisation (white dots). (**d**) The raw marker positions can be rendered into a greyscale two-dimensional image which reports nanoscale event densities. Scale bars 1 μm (**a**, **b**); 200 nm (**c**, **d**). *Figure modified from Soeller & Baddeley 2012 JMCC*

labelling patterns (Fig. 1a; inset) that in shape resembled the point-spread function of the microscope (which can often be approximated by two-dimensional Gaussians) now appeared as densely labelled patches with more complex shapes and sub-structure (Fig. 1b). In each of these regions, a high density of single molecule events was observed, as illustrated in the event map (Fig. 1c) where each white dot represented a unique single molecule event. These maps can be rendered into greyscale 2D images whose pixel intensities now reflect the local event density (Fig. 1d) and more closely resemble conventional fluorescent micrographs. The striking feature of such greyscale rendered super-resolution image was the level of detail of the labelled areas of the RyR clusters with clearly delineated outlines. Calculating the typical number of RyRs within these patches was relatively straightforward with the assumption that receptors typically organise into ~30 × 30 nm quasi-crystalline two-dimensional arrays [4] within peripheral couplons are organised parallel to the surface sarcolemma [36] as schematically illustrated in Fig. 2a. This analysis revealed a near-exponential distribution of cluster sizes (Fig. 2b, stated as the number of receptors) which reported a mean cluster size of

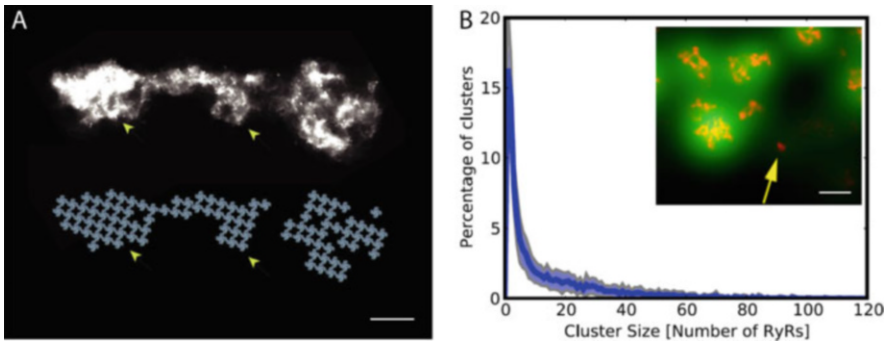

Fig. 2 Quantification of the size of RyR clusters resolved from dSTORM images. (**a**) The two-dimensional area of peripheral couplons as RyR labelling in dSTORM images (left) could be binarised to obtain cluster area and calculate the typical number of receptors from their anticipated arrangement (schematic on right), i.e. assuming a 30-nm centre-to-centre quasi-crystalline arrangement. (**b**) A histogram of the RyR cluster sizes (main panel) prominently features a large number of clusters consisting of a few receptors (arrow indicating dSTORM image; red in inset) that are not typically detected in the diffraction-limited image of the same region (shown as green overlay); *Modified from Baddeley et al 2009 PNAS*. Scale bars 50 nm (**a**), 250 nm (**b** inset)

~14 RyR and a large number of patches that corresponded to solitary receptors which were previously not observed with EM or diffraction-limited methods (Fig. 2b inset). The integral of this distribution however revealed that the majority of RyRs (as total fraction of all RyRs taken together) within peripheral couplons were still found within a subset of clusters that contained $\geq$25 RyRs. A key feature of this observation was that the shape of this observed cluster size distribution closely resembled that resulting from a relatively simplified Monte-Carlo simulation of cluster growth that relied on stochastic self-assembly. This suggested that the sizes of RyR clusters were the likely result of a stochastic growth process, balanced by receptor turnover.

RyR cluster shapes were complex and often non-circular while a number of patches showed notable gaps within the patches. Comparing the super-resolution image with the corresponding diffraction-limited image acquired at the beginning of the sequence, it was striking to find that labelling densities identified as single puncta in the latter often corresponded to multiple clusters that were now clearly resolved (Fig. 3). It was also noted that small clusters, corresponding to one or a few receptors often did not appear as discernible fluorescence density above background in the diffraction-limited images. Analysis of the edge-to-edge Euclidean distance of the new SMLM data revealed that the neighbouring clusters of $>$1/3 of the labelled patches were located within 50 nm—a distance that is well below diffraction-limited microscopies as well as other super-resolution approaches such as STED. Computer simulations predicting cytoplasmic Ca^{2+} concentrations as high as 10 μM in a zone 100 nm outside of dyads [37] were therefore compatible with the possibility that such closely located RyR clusters may co-activate during Ca^{2+} release. With this in

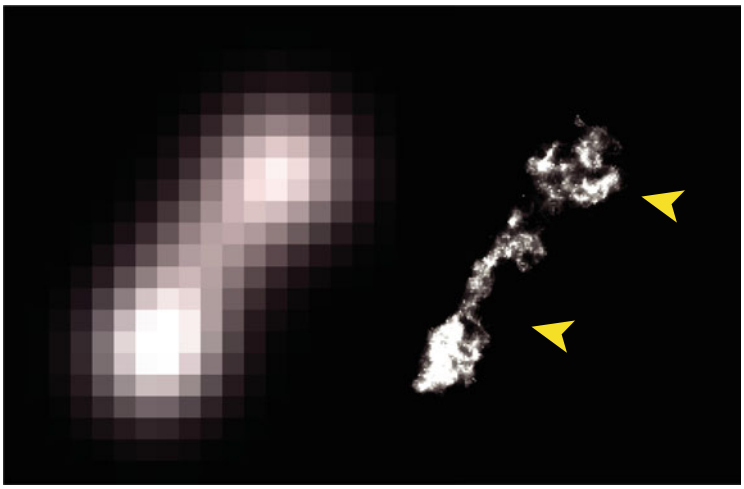

Fig. 3 Punctate labelling densities observed in diffraction-limited TIRF image (left) often corresponded to separate areas (arrowheads on right) of RyR labelling resolved by dSTORM, giving rise to the concept of RyR super-clusters. Scale bar 200 nm

mind, RyR clusters located within 100 nm of one another's edges were grouped into 'superclusters'. Superclusters typically consisted of 2–5 clusters with a mean ensemble of 21.6 RyRs and morphologically resembled the tomographic reconstructions of RyRs of the deeper dyads within mouse ventricular myocytes [38]. This observation led to the hypothesis that super-clusters may open in concert through a 'triggered saltatory' mechanism to give rise to a local Ca^{2+} spark provided that they are accessed by a similar luminal SR Ca^{2+} concentration in addition to the elevated cytoplasmic Ca^{2+} concentrations. This notion was supported by the general lack of closely abutting terminal cisterns or dyads in EM data, although the super-resolution data lacked a means to observe the local SR or dyad structure at the level provided by EM data.

Investigating the RyR distribution within dyads located deeper in the cell interior required a different strategy. As previous diffraction-limited analyses had demonstrated [10, 34], RyR clusters are located at sub-micron distances along the z-lines of the myocytes. While the standard implementation of dSTORM offered resolution as fine as 30–60 nm, its axial resolution was still limited by diffraction to ~600 nm. As demonstrated by Chen-Izu et al. [34] this limited axial resolution is partially overcome by imaging the z-line distributions of proteins in the transverse orientation of the myocytes (i.e. on end). This was best achieved by Hou et al. [11] by adapting the dSTORM RyR immunofluorescence protocols to thin (5–10 μm) cryosections of the rat ventricles where myocytes are transversely sectioned. The RyR labelling pattern in these cells consisted of densely labelled areas located in the inter-myofibrillar spaces (Fig. 4a, b). These areas of labelling represented 2D projections of the dyadic RyR clusters, however as a close approximation, the two-dimensional area of each labelled cluster was used for calculating the expected

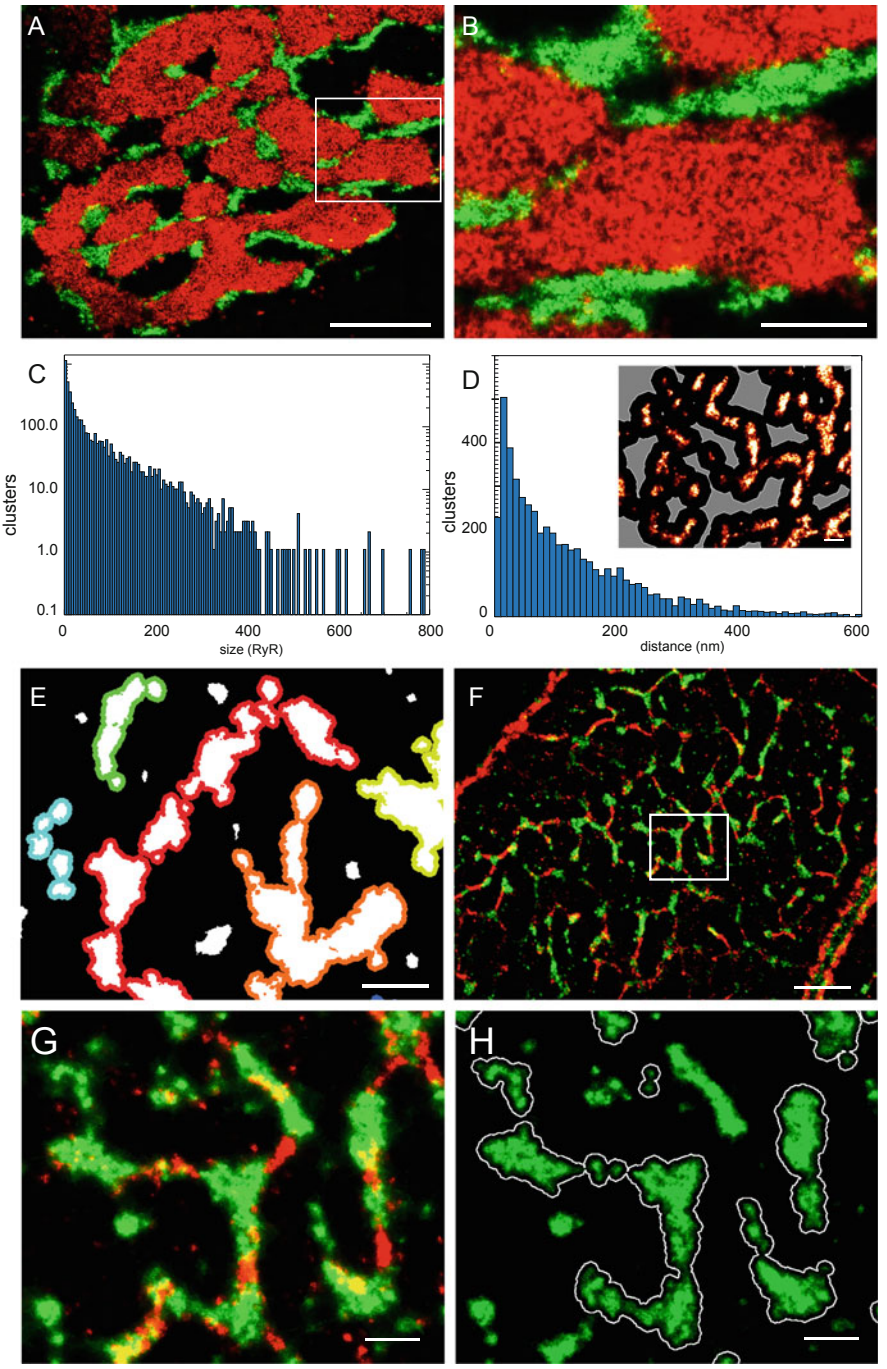

Fig. 4 Quantification of dSTORM images of RyR distribution in the interior of rat ventricular myocytes. RyR cluster localisation in relation to myofibrils and t-tubules. (**a**) Overlay of multicolour transverse dSTORM images of the myofibril marker α-actinin (red) and RyR (green)

number of RyRs assuming that the 2D area of occupancy for a single RyR was ~900 nm^2. This is clearly still a simplification that may underestimate cluster size but provides a lower bound and use of a suitable correction factor should further improve the estimate in the future. Similar to the observations of the peripheral couplons, the cluster size distribution in the interior resembled an exponential distribution. It was observed that labelled areas corresponded in size to single receptors or multiples ranging up to large clusters of >600 receptors (Fig. 4c). In contrast to peripheral RyR clusters, the interior dyad clusters were ~4 times larger (mean of ~63 RyRs/cluster) and typically more elongated along the cross-sectional boundaries of the myofibrils. Intriguingly, RyR labelling occupied a very consistent fraction (~57%) of the myofibril boundaries [11]. More than 60% of clusters were located at distances shorter than the mean inter-cluster distance of ~140 nm and virtually all clusters were within 500 nm of each other's edge (Fig. 4d and inset). The latter observation meets the distance criterion for the simulated propagation of a Ca^{2+} wave across the entire width of a myocyte starting from a spark at one RyR cluster [34]. Such inter-cluster co-activation will likely occur between superclusters (based on the 100 nm edge-to-edge distance criterion) which, on average consisted of ~102 RyRs as an ensemble of ~3.4 sub-clusters. Notably, the subcluster ensemble within superclusters appeared to group into highly extended formations (Fig. 4e) that broadly resembled the previously observed transverse view of t-tubules [18]. As evidence that superclusters may belong to the same dyad, SR terminal cistern or sarcolemmal subspace, they were observed on either the same or adjacent segments of t-tubules in two-colour dSTORM images that also visualised the local t-tubule nanoarchitecture (Fig. 4f–h).

While the super-resolution images of RyR consistently showed closer cluster arrangements and a larger range of cluster sizes than observed through confocal microscopy, it is important to reconcile these discrepancies. One can be assured that

Fig. 4 (continued) at the z-disks of a rat ventricular myocyte. (**b**) Magnified view of the box region in panel A illustrating the RyR clusters closely lining the myofibrillar bundles. (**c**) The frequency histogram of cluster sizes (notice log scale) exhibits a near-exponential size distribution with a mean size of 62.8 ± 2.98 RyRs (mean ± SEM) and a few notable clusters containing >500 receptors. (**d**) Frequency histogram (main panel) of the edge-to-edge nearest-neighbour distance shows that >60% of clusters are located at distances shorter than the mean inter-cluster distance of 139.5 ± 8.5 nm. In the inset, an overlay of a transverse dSTORM image of RyR labelling within a myocyte with a 250 nm distance contour measured from cluster edges (white lines) shows that nearly all clusters were within <500 nm distance of each other. Note that grey areas indicate distances >250 nm. (**e**) Magnified view of the box region illustrates grouping of RyR clusters into superclusters in which member clusters have edge-to-edge distances <100 nm (shown with surrounding distance bands of 50 nm. When these touch or overlap clusters are ≤100 nm apart; coloured to illustrate distinct superclusters). (**f**) Overlaid dSTORM images of RyR (green) and t-tubules labelled with a combination of anti-CAV3 and anti-NCX antibodies (red). (**g**) A magnified region illustrates the strong co-registration between the elongated axes of the RyR clusters and the local t-tubule geometry. Note large (>500 nm long) clusters co-locating with t-tubule branch points. (**h**) The RyR superclusters within the same region in panel (**e**) overlaid with 50 nm Euclidean contours to illustrate that supercluster grouping often grouped individual clusters that lined up along the same t-tubular connections. Scale bars 2 μm (**a**, **f**), 500 nm (**b**, **d** inset, **e**, **g**, **h**). *Adapted from Hou et al 2015 JMCC*

the dSTORM image morphologies of RyR were essentially the structures underlying the punctate structures seen in confocal images by visual comparison of the two types of images side by side (e.g. Figs. 1a, b and 3). For a more quantitative comparison, confocal images were simulated by convolving the dSTORM images of RyR with a confocal PSF (Fig. 5a, b). The resulting dSTORM images were characteristic of the punctate morphologies of RyR labelling throughout the entire width of the myocyte (at the z-line), as observed in earlier confocal images [10]. Analysis of this simulated confocal data using a matched filter centroid detection algorithm as previously described, it was observed that the locations of

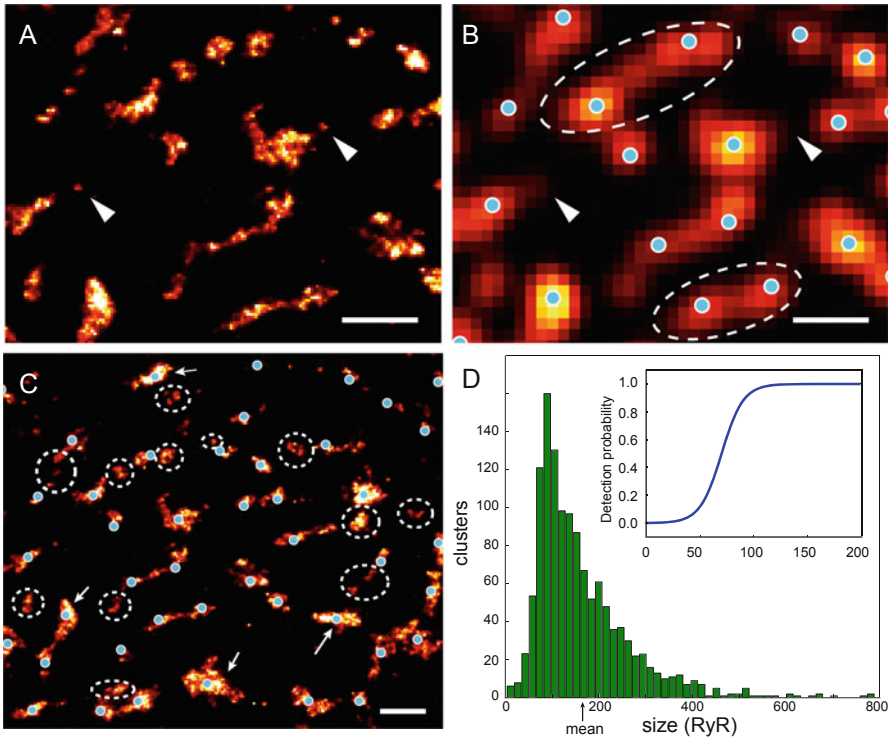

Fig. 5 Simulation of diffraction-limited imaging of RyR based on super-resolution images. (**a**) A transverse dSTORM image focused near the z-lines of a myocyte. (**b**) The equivalent confocal image was generated by convolving the localised marker positions with a confocal point spread function. Close examination revealed the lack of notable fluorescence from the small RyR clusters (arrowheads). Centroids of the punctate RyR labelling in confocal images (overlaid in **b**) had comparatively poor correlation with the number and shapes of some RyR clusters (e.g. region indicated by dashed lines). (**c**) Shown, is a larger overview of the super-resolved RyR image overlaid with the centroids of the detected puncta from the confocal data to illustrate the many clusters that were not detectable in the diffraction-limited approach. (**d**) The "apparent" RyR cluster size frequency histogram obtained by considering a detection function (inset) resulting in a mode at ~100 RyR with a mean apparent cluster size of ~165 RyRs. Scale bars: 500 nm. *Adapted from Hou et al 2015 JMCC*

the detected centroids of the clusters correlated poorly with the underlying features of the RyR distribution resolved by the super-resolution image. These observations were: (i) typically only larger clusters were detected; (ii) multiple detections were made on clusters that were elongated in shape, (iii) multiple clusters were incorrectly detected as a unitary cluster when located close together (dashed lines in Fig. 5b) and (iv) some clusters that showed lower intensity or smaller area of labelling were not detected (dashed lines in Fig. 5c). This apparent inability to detect RyR clusters smaller than ~50 receptors was captured with a detection probability function (Fig. 5d inset) which was multiplied with the super-resolution size histogram (Fig. 4c) to replicate the sharp drop-off in the histogram of cluster sizes (main panel Fig. 5d) deduced from deconvolved confocal data in previous experiments [10]. It was also apparent that as a consequence, the mean of the estimated cluster size was approximately twice as large as that in the super-resolution analysis.

As mentioned above quantification of RyR cluster sizes based on 2D dSTORM data is not straightforward as it does not often capture the three-dimensional features observed in EM tomograms [38]. The analysed images, which are essentially projections of the curved dyad topology, often would under-estimate the true area occupied by a RyR cluster. However the estimated cell-wide density of RyR of ~134 RyR/fL calculated with this method is in broad agreement with that (95 RyR/fL) calculated based on ryanodine binding experiments [39]. It is therefore possible that the single RyR packing densities in clusters may at least in some areas of the clusters deviate such that the 30 × 30 nm centre-to-centre distance used in the above analysis (Fig. 4c) could over-estimate the true receptor density within the dyads. However, even to observe single receptors within a flat cluster with 50 nm centre-to-centre receptor packing distance we would require a technique that would offer a minimum of ~20 nm in plane resolution. In the current implementation of dSTORM or PALM, this is often beyond the resolution that can be achieved in imaging optically-thick samples such as myocytes or cryosections.

Use of Multi-Colour and Quantitative dSTORM for Resolving Further Junctional Features

Junctophilin-2

Beyond the visualisation of nanoscale features of the RyR cluster structure, a number of innovations in super-resolution microscopy have provided significant new insights into the molecular machinery and the dyad architecture that surround the arrays of RyR. The primary advancement was made in the development of multi-colour dSTORM protocols. By adopting an imaging protocol where spectrally-similar fluorophores are simultaneously excitable at a single wavelength, it was possible to acquire super-resolution images of pairs of cellular structures in the same length of time that was required to acquire a single-colour dSTORM image. To this end, the emission of single molecule events within the sample were split with the utility of a dichroic mirror and translated onto two adjacent halves of the sensitive camera (e.g. EM-CCD) which could be computationally re-aligned post-hoc. The

ratio of the amplitudes of the fluorescence intensities of the two facsimiles of each event on the two halves of the image was unique to each fluorophore species and was used for determining their spectral identity which in principle allows distinguishing three or more fluorochromes by using just two channels [40, 41].

This method was exploited to analyse the nanoscale organisation of junctophilin-2 (JPH2) in relation to RyR clusters. A sensitive co-localisation analysis developed for the super-resolution images revealed a high fraction of co-localisation of JPH2 with RyR (~72%) in super-resolution images of the peripheral couplons of rat ventricular myocytes. Coinciding with this high proportion of co-localisation, striking similarities in the shape and area of the RyR clusters and the local area occupied by JPH2 were also observed (Fig. 6a). Strong alignment between their respective centres of intensity (within ~40 nm of each other at each cluster) was further evidence that the JPH2 molecules were broadly confined to the two-dimensional area occupied by the RyRs. Examining the same target pair in the deeper dyads in cryosections, a lower co-localisation of JPH2 with RyR was observed (<65%). Visual examination of dSTORM images however suggested that the differences in morphology of JPH2 and RyR staining, despite some minor heterogeneities (arrows in Fig. 6b), were minor. Control experiments and computer simulations where RyRs within rat ventricular tissue sections were double labelled with mouse and rabbit anti-RyR primary antibodies and two spectrally-different secondary antibody-fluorophore conjugates for dSTORM demonstrated that such heterogeneity was largely explained by stochastic variations in the antibody labelling efficiency and the photoswitching of the fluorophores within a given time window [11]. However, in both the surface couplons and interior dyads, the fraction of JPH2 co-localising with RyR was consistently lower than that observed in the above control experiments, which led to the conclusion that JPH is neither located in specialised anchoring domains at the dyad nor are they likely to interact with RyR at a 1:1 stoicheometry. The co-localisation estimates and the patterns of their labelling were most suggestive of an interspersed JPH2 arrangement that was confined to the RyR cluster area (Fig. 6c). It was therefore conceivable that a loss of JPH expression (e.g. when JPH2 expression is silenced [22]) could lead to an intrinsic destabilisation of the couplons across the RyR cluster area.

This hypothesis is well-supported by the loss of expression [13] or calpain-mediated cleavage [42] of JPH2 in cardiac pathologies and the concurrently diminished EC coupling. Super-resolution microscopy was further utilised to explore the functional changes that may accompany the loss of JPH2 from the dyads. Cardiac myocytes isolated from tamoxifen-inducible conditional knockdown mice of JPH2 were imaged using dSTORM to report an ~50% loss of sodium-calcium exchanger (NCX) localisation in the dyads. These mice experienced increase SR Ca^{2+} leak and severely altered Ca^{2+} spark properties either by the loss of NCX activity which adjusts the dyadic Ca^{2+} levels and/or the loss of the suspected direct modulation of RyR2 by JPH2 [43]. In addition to maintaining the correct organisation of the calcium handling proteins within the vicinity of the RyR cluster, it now appears that JPH expression also plays a role in determining the overall size and shape of the dyads. Mice overexpressing JPH2 who exhibited a highly expanded and convoluted

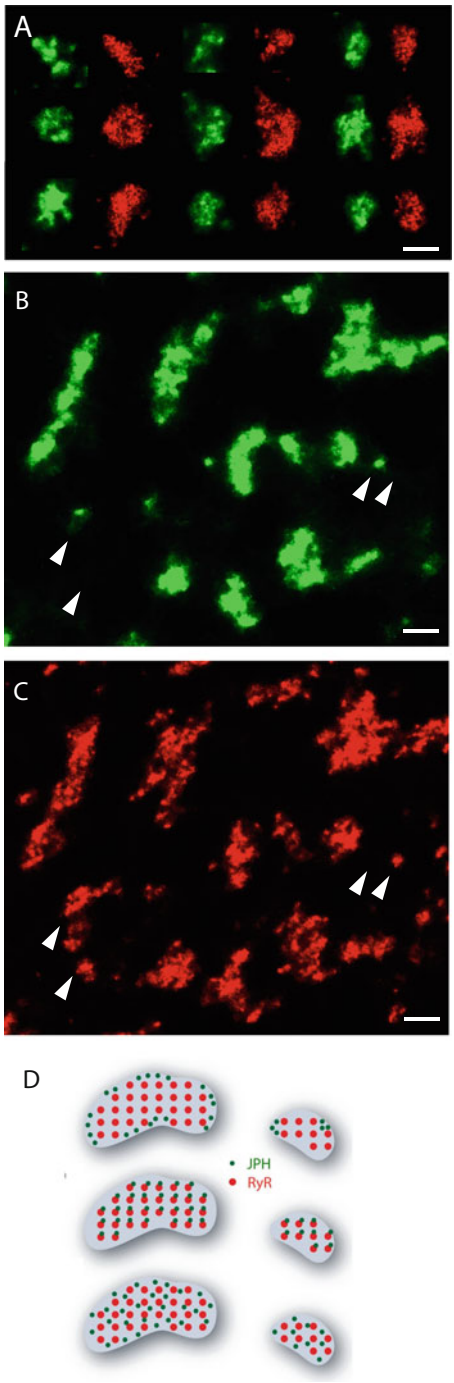

Fig. 6 Analysis of the spatial relationship between JPH2 organisation and RyR clusters in rat ventricular myocytes. (**a**) series of randomly chosen dSTORM image regions of JPH2 staining near the surface of enzymatically-isolated rat ventricular myocytes (green) and the corresponding dSTORM image of the local RyR staining (red) shown horizontally displaced to highlight the similarities in the area and shape of the labelled regions. Similarly, two-colour dSTORM images of the (**b**) JPH2 staining in the deep interior of a myocyte within a transverse section of the rat ventricle and the matching (**c**) RyR staining are shown. The morphologies of the labelling densities are broadly very similar although small regions were observed (arrowheads) where the labelling did not visually co-localise. (**d**) Schematic distributions of RyR and JPH2 organization that were considered include JPH2 confinement to distinct anchoring domains within or around the area of the RyR cluster (top) a direct interaction with RyRs at a 1:1 stoichiometry (middle) and, the more likely organisation based on the super-resolution data, a randomly dispersed arrangement of JPH2 within the junctions (bottom). Scale bars: 250 nm. Panels A&D *Adapted from Jayasinghe et al 2012 Biophys J; Panels B&C from Hou et al 2015 JMCC*

dyad structure, which incidentally protected the myocytes from a number of adverse remodelling that would have resulted from cardiac pressure overload [44]. Whether JPH2 determines the RyR cluster size (in terms of number of receptors within it) either as a cause or a consequence of its effect on the dyad structure remains to be seen.

T-system

By the time that the super-resolution imaging methods had become available a great deal of information on t-tubule structure had already been provided by both EM and diffraction-limited fluorescence microscopies. For example, Golgi stain-based EMs were highly effective in revealing intricate (nanometre-scale) details of skeletal muscle t-tubule structure [8, 45]. The Golgi-stain however was incompatible with EM of cardiomyocytes [8]. 3D reconstructions of deconvolved multi-photon images of extracellular infiltration of fluorescein-dextrans had revealed the three-dimensional complexity of the cardiac t-tubules; however, the resolution of these reconstructions was essentially limited by diffraction [9]. Soeller and Cannell [9], at the time, identified the limitation that t-tubules narrower than ~70 nm were not identifiable with a volumetric fluorescent marker such as fluorescein-dextran. Subsequent confocal studies often observed punctate or variable labelling densities in the immunofluorescence of calcium handling proteins (e.g. LCC or NCX) residing in the t-tubular membrane [17, 18], however it was inconclusive whether this morphology was a result of varying t-tubule nanostructure or a true heterogeneity in their distribution in the membrane.

The first super-resolution images of t-tubules were obtained via STED microscopy of ventricular myocytes stained with a lipophilic membrane dye [31] to demonstrate nanoscale dilatations in the t-tubules of the murine heart. While dilated t-tubules had been visualised in larger species with naturally larger t-tubules (e.g. human, canine [46–48]), this was one of the first clear demonstrations of nanometre-scale remodelling of t-tubules in a small (murine) species and could be performed in intact myocytes. This was also a noteworthy revelation that the t-tubule remodelling in cardiac pathologies are unlikely to be fully resolved by diffraction-limited microscopy methods, hence cannot be fully characterised by the 'regularity indeces' of the cell-wide t-tubule distributions (e.g. [49]).

Adapting SMLM methods for visualising the cardiac t-system is perhaps less straightforward than imaging distributions of a molecular species of interest (e.g. RyR or JPH). This is mostly the result of the lack of a robust intrinsic membrane stain that reliably reports all of the t-tubular membranes in all of the animal species. For example, wheat-germ agglutinin conjugates of photoswitchable fluorophores are consistent in staining t-tubules in larger species (e.g. horse, human), however reports an incomplete t-tubule morphology in smaller animals (e.g. mouse, rat and rabbit) [32, 33, 50, 51]. In smaller animals, caveolin-3 and NCX report extensive t-tubule labelling, however their distributions are weakly anti-correlated along the t-tubules. Therefore, a closer approximation of the t-tubule membrane can be obtained by dSTORM immunofluorescence imaging of a cocktail of antibodies targeting NCX and CAV3 [32, 33].

Combination of dSTORM with EM tomography was instrumental for demonstrating localised dilatations in the t-tubules in the vicinity of dyads within murine ventricular myocytes [52]. Independent tomography [53] and dSTORM studies [32, 33] have also confirmed localised dilatations in the t-tubules of rat myocytes. SMLM methods have also been useful for validating the indirect measurements of t-tubule diameters previously made with diffraction-limited microscopies [5] (see [32, 33], for review) and have offered a method to observe both micron- and nanometre-scale features of t-tubules in large sample areas (e.g. whole cells) with a throughput and level of effort that still not matched by the tomographic EM (which admittedly provides still much higher resolution). This feature of SMLM has allowed us to appreciate the fine features of the t-systems across a broad range of species (Fig. 7). For example, rat and mouse ventricular myocytes have intricate t-tubules of varying diameters that form a highly interconnected network which spans the cross-sectional area of the cell. In contrast, larger species such as rabbit, human and horse have wider tubules and fewer bifurcations that form a cross-sectional morphology that loosely resemble 'spokes on a wheel'. On first comparison with the diffraction-limited data, no new features of the t-tubules in larger species are obtained with the super-resolution. However, more recent dSTORM data of human cardiomyocytes have revealed its strength in being able to distinguish between t-tubule-coupled and uncoupled RyR clusters that are otherwise indistinguishable in diffraction-limited images [35] (Table 1).

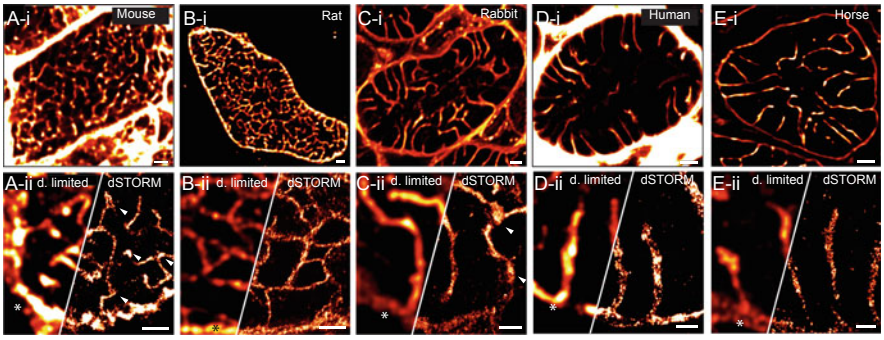

Fig. 7 Comparison of t-system micron- and nanometre-scale morphologies in adult mammalian cardiac myocytes. Transverse (i) Confocal and (ii) dSTORM images blurred with a 2D Gaussian PSF equivalent to a confocal PSF (left panels) and super-resolution image (right). Myocytes from (**a**) C57-BL/6 mouse and (**b**) Wistar rat were stained with a combination of NCX1 and CAV3. Fixed ventricular tissue sections from (**c**) New Zealand White rabbit, (**d**) Human (54-year old donor with normal echocardiogram) and (**e**) Horse (12-year old female New Forest pony) were stained with fluorescent wheat germ agglutinin to visualise the t-tubules. Note the nanometre- and micron-scale t-tubule dilatations in mouse and rabbit myocytes respectively (arrowheads). Cell surface in each example is indicated by asterisks. Scale bars: i-panels: 2 μm; ii: 1 μm. Adapted from *Jayasinghe et al. 2014 Eur J Trans Myol*

Table 1 Summary of key measurements made obtained by quantitative analysis of dSTORM imaging of RyR staining in rat cardiac ventricular myocytes

Measurement	Cell interior Mean ± SEM (n cells/ n animals) *From Hou et al 2015 JMCC*	Cell surface Mean ± SEM (n cells/ n animals) *From Baddeley et al 2009 PNAS and Jayasinghe et al 2012 Biophys J*
RyR cluster size (RyR)	62.8 ± 2.98 (13/3)	13.6 (22/3)
Cluster nearest-neighbour edge-to-edge transverse distance (nm)	139.53 ± 8.51 (13/3)	–
RyR density (RyR/μm^3)	133.86 ± 7.02 (6/3)	–
RyRs per supercluster	102.72 ± 3.54 (6/3)	21.6 (10/2)
Sub-clusters per supercluster	3.40 ± 0.73 (6/3)	–
RyR cluster density/μm^3, (n = 5 cells)	2.21 ± 0.30	–
Percentage of MF perimeter lined by RyR (%), (65 myofibrils, n = 3 cells)	57.18 ± 8.58	N/A
% of RyR labelling co-localising with JPH2 with 30 nm uncertainty distance criterion	77.94 ± 4.67 (10/3)	80.6 ± 3.1 (5/2)
% of JPH2 labelling co-localising with RyR with 30 nm uncertainty distance criterion	75.34 ± 4.95 (10/3)	90.4 ± 0.5 (5/2)

Methodological Considerations: Adaptating Localisation Microscopy for the Study of Cardiac Muscle

As outlined above with the examples of studying the cardiac dyad structures, SMLM offers a number of advantages that are well-suited to advancing our understanding of nanoscale signalling structures and their functional role in the heart. In practice, there are a number of key modalities of SMLM, known by their own respective acronyms that need to be considered carefully for their suitability for the experiment of interest. These include:

- PALM/fPALM (**p**hoto**a**ctivated **l**ocalization **m**icroscopy) [24, 54] which uses fluorescent probes that are initially dark (in the channel of interest) such as PA-GFP, mEos, or caged fluorescein. Exposure to low intensity UV light (typically at 405 nm) stochastically turns some molecules on which are then rapidly imaged and bleached by stronger excitation light (e.g. 488 nm).
- STORM (**st**ochastic **o**ptical **r**econstruction **m**icroscopy) [25] uses a pairing of two small molecule dyes, one of which is typically a Cy5 or Cy7 derivative and

fluoresces at the far red end of the spectrum, the other is typically a shorter wavelength excited dye used for activation (e.g. Cy3). Exposing the cyanine dye to intense illumination in the presence of thiols in the solution will cause a transition to a dark state, from which it can be effectively recovered by excitation of the shorter wavelength dye.

- dSTORM/RPM/GSDIM [29, 30, 36, 55] expand on the STORM concept, extending it both to a wider range of dyes and dispensing with need for a specific activator dye, instead relying on either thermal relaxation or a weak blue/uv absorption characteristic of the dark state for re-activation.

The most commonly used modality for mapping protein distributions in wildtype rat cardiomyocytes has been an adaptation of immunofluorescence labels for dSTORM. Therefore the remainder of this chapter will outline this basic approach and implications for imaging.

SMLM Imaging Principles: dSTORM

The key feature of dSTORM is the intrinsic stochastic photoswitching of a single species of fluorophores that is physically attached either to the target of interest or the marker molecule (see [56, 57] for a more detailed account of the mechanism). As schematically illustrated in a Jablonski diagram (Fig. 8a), the fluorophore is excited

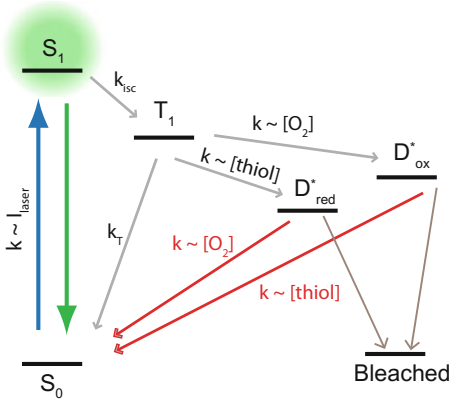

Fig. 8 Putative mechanisms behind dSTORM switching. Fluorescence is only observed when the molecule cycles between ground state S_0 and singlet excited state S_1. Occasionally, it may transition to a triplet state T_1. A long-lived dark state D^*_{red} is created by chemical reduction of the triplet excited state T_1. With recovery illumination, light typically of shorter wavelengths is absorbed by the fluorophores at the dark states (steps indicated in red) to return it to the S_0 ground state, but the transition back to S_0 also occurs spontaneously, a process often termed thermal relaxation. Availability of oxygen and primary thiols can affect the rates at which the transitions occur. *Re-drawn based on Vogelsang et al. 2009, van de Linde et al. 2011 and Dempsey et al. 2009*

from the singlet ground state (S_0) to the singlet excited electronic state (S_1) from which it can relax back to S_0 while emitting photons in the mechanism, the "normal" situation during which a fluorophore appears bright. However, intense light absorption can also promote intersystem crossing into a triplet state T_1 (because it rapidly cycles the molecule from the ground to the excited state increasing the chances of the less likely transition to stochastically occur) from which the molecule can form meta-stable radical anion intermediates D^*_{red} or D^*_{rox} depending on the availability of thiols or oxygen in the immediate environment of the fluorophore. These intermediate states can be long lasted (up to many seconds) and are stochastically may return back to S_0 or eventually enter a permanently photobleached state. By providing a chemical environment to the sample that promotes this cycling of the fluorophores via the dark anion intermediate states, it is possible to reversibly "darken" a large fraction of the fluorophores within the illuminated region allowing the detection of the momentary fluorescence of a small subset of fluorophores (from the rapid transition between S_1 to S_o until they re-enter the triplet and the reduced states; Fig. 8). These brief bursts are often referred to as 'blinking'. The blinking properties of the sample will determine the localisation of single marker molecules and the accuracy of this localisation process. Therefore, the sample preparation protocols, the hardware and imaging protocols are all adapted towards achieving fluorophore blinking that favours precise localisation and the overall image reconstruction. From our practical experience common challenges in dSTORM, assuming that the sample is well-labelled to start with, lie in the progression of the bulk of the fluorophores towards permanently photobleached states or reduced dark states that are not easily recoverable towards S_o, conditions the experimenter may refer to as failure to blink properly which can sometimes (but in our experience not always) be traced to changes in the composition of the so-called switching buffer, see below. As a bottom line, as SMLM brings with it further requirements for a successful imaging experiment than most diffraction-limited modalities, e.g. proper blinking, success rates tend to be lower than, say, confocal imaging and the experimenter in general has to work harder for a high quality result. This should not be surprising following the old adage "nothing is for free".

Fluorophores and Sample Preparation

Much of the popularity of dSTORM (also as opposed to the original STORM requiring activator dyes) has been the demonstration that virtually any organic fluorescent dye species can be tuned for the photoswitching required for dSTORM either by delivering sufficient excitation light intensity and/or a sample mounting buffer that is conducive to these dark state transitions. So far, the most promising class of dyes for buffer-induced switching are the near infrared emitting cyanine dyes such as Cy5 and Alexa 647 [25, 55, 58]. Extensive surveys of the blinking properties of various dyes in thiol buffers are given in [27, 58] and these are currently the go-to reference for dye and mountant suitability for super-resolution. An ideal fluorophore species exhibits both good photon yields and sufficiently long lived dark

states when imaged in buffer containing ~5–50 mM concentrations of a primary thiol acting as a reducing agent. In addition to the thiol reductant it is advantageous to reduce the level of dissolved oxygen in the buffer through the use of an oxygen scavenging system such as glucose oxidase and catalase. Practically speaking, another great advantage of such dyes being very suitable is the fact that these had been widely used for convential diffraction-limited imaging prior to the advent of super-resolution imaging. This ensured that these dyes are readily commercially available conjugated to a wide range of biological markers.

In our own work to date we have frequently used Alexa 680 and Alexa 750 as a pair of fluorochromes with broadly compatible switching behaviour in buffers containing β-Mercaptoethylamine (MEA) as a reducing agent. This pair makes a suitable combination for dual-colour super-resolution images with very low cross-talk [40, 41]. Cardiac muscle samples (isolated and fixed myocytes or fixed cryosections) are thicker than the typical samples subject to SMLM (e.g. cultured cell lines such as COS7). Imaging at depths of 5–15 μm is common in these experiments which therefore require better refractive index matching than offered by aqueous switching buffers to reduce the effect of spherical aberration and light scattering on the localisation of single fluorophores. This is achieved by basing the mounting medium on glycerol as exemplified by the following recipe:

1) Make a 1 M stock of MEA in 10× PBS and pH to 7.5. This stock is stable for 1–2 weeks in the fridge, or for several months at −20 °C (thawing and re-freezing should be avoided by aliquoting). We find that the HCL salt is somewhat easier to deal with than straight MEA.
2) Dilute the 1 M stock to 100 mM with 10× PBS.
3) Mix 1 part of diluted stock with 9 parts glycerol. Mixing should be performed using a rocker table or similar and should continue until no 'schlieren' are visible.

Both diluted stock and final mountant should be made fresh before each imaging session.

We recommend a number of chemical checks of the mounting medium to ensure proper switching, see also Crossman et al. [35]. It is noteworthy that the optimal range of MEA concentration that is conducive to acceptable blinking (i.e. one that maximises $k_{[thiol]}$) may be specific to the fluorophore(s) selected for a particular sample. Further, oxygen scavenging mechanisms that rely on enzyme systems (e.g. glucose oxidase and catalase) are inefficient in media that are based on glycerol as the enzyme activity crucially rely on the availability of an aqueous environment. We note, however, that due to the higher viscosity, oxygen availability is greatly reduced which has a similar effect as reducing free oxygen in aqueous samples.

The most common far-field implementation of SMLM is a form of widefield microscopy (see details below). As is typically the case with widefield microscopy, this often involves poor contrast of the sample from out of focus fluorescence, particularly when dealing with "thick" samples as is generally the case with cardiac cells and tissue. Even when the fluorophores within the intense illumination cone have been forced into the triplet and reduced dark states, autofluorescence from the

tissue may still manifest in a substatitial background signal which can either completely or partially obscure the fluorescence from single markers which compromises both event detection and localisation precision. This problem is compounded by the 'optically-thick' nature of cardiac muscle samples as cells are typically 10–20 μm in thickness. One of two strategies may be adopted depending on the cellular location of the structure of interest. Structures located on the longitudinal surface of the cell or those only observable in living cells are best imaged in enzymatically-isolated myocytes that have been adhered or settled onto the coverslip. In these scenarios the illumination may be adjusted to total internal reflection fluorescence (TIRF) mode or as a compromise, the focal plane levelled with the interface between the cell surface and coverslip. Using TIRF illumination, however, is somewhat problematic since the rapid decay of illumination intensity from the coverslip surface greatly reduces the ability to push out-of-focus fluorochromes into a dark state. As a net effect this leads to more background than using a "near-TIRF" configuration, which helps ensure that a narrow sheet of light escapes into the sample. This is often used and known as a HILO configuration [59].

For all structures within the cell interior, high-quality cryosections that are 5–15 μm in thickness are recommended in order to limit the out of focus widefield fluorescence. It is also recommended to select stains that provide high contrast and little or no non-specific staining. Basic immunofluorescence labelling protocols are sufficiently robust to achieve dense and specific labelling that is acceptable for dSTORM, in our experience. However, it is recommended that the reagents that are used are of molecular grade and the coverslips/slides/dishes used for mounting the sample have minimal intrinsic fluorescence in the spectral windows used for collecting single molecule emission.

Anatomy of an SMLM Apparatus

The hardware requirements to perform single molecule based super-resolution imaging are surprisingly straightforward, consisting of little more than a conventional widefield fluorescence microscope equipped with a high numerical aperture objective, a very sensitive camera, and a source of intense illumination, typically a laser. This relative "simplicity" has contributed to the relative popularity of localisation microscopies among optical super-resolution methods. The two principle areas where localization microscopy demands significant improvements over the specifications of a standard fluorescence microscope are in light sensitivity and mechanical stability.

Optimal light sensitivity is crucial to localising single fluorophore fluorescence. The primary component to maximising the light-gathering capacity is a high numerical aperture (NA) objective, typically 1.45 NA or higher. It is often beneficial to also have a correction collar option that can compensate for sample refractive index, which even with a glycerol-based medium, is lower than that of glass. A second crucial component is a sensitive light detector which offers high quantum efficiency in the range of emission spectra of the fluorescence species that are routinely imaged.

Among the most commonly-used options, electron multiplying CCDs (EMCCDs) and scientific CMOS (sCMOS) cameras are noteworthy. EMCCDs have been the preferred choice due to their extremely low readout noise and comparatively fast speed. The introduction of sCMOS cameras, which offer better readout speed and essentially the same effective QE as emCCDs (since the reduced nominal QE of sCMOS cameras is offset by the absence of the multiplicative noise associated with emCCDs) with only a very moderate increase in readout noise (as compared to EMCCDs) has the potential to change this preference. sCMOS cameras, however, suffer from pixel to pixel variations in gain and readout noise which must be accounted for in the design and implementation of analysis algorithms [60, 61]. Also a consideration in developing a customised imaging apparatus is the approximately fourfold difference in the price between EMCCD and sCMOS cameras which may need to be weighed against the typical photon yields that are routinely achieved from single molecule blink events within the sample.

In order to obtain a high quality super-resolution image, a large number of molecules must be independently localised. This requires the collection of a large number of image frames (typically on the order of 20–50,000). If collecting data at a reasonably typical rate of 20 FPS, this corresponds to 15–40 min. Any instrumental drift over this time period will result in a corresponding degradation of the resulting images. As conventional microscope hardware will typically experience several microns of drift over this time span, it is obviously a critical issue for localisation microscopy. There are two principle approaches to coping with drift—adapting the microscope hardware to minimise drift, and measuring and correcting the drift after data acquisition. Most localisation microscopes combine aspects of both approaches; attempting to make the hardware as stable as possible and then correcting any residual drift in post-processing (see Image Analysis section for post-hoc drift correction). However, as focus drift is very hard to correct in post-processing, some form of active focus compensation is often employed (e.g. active microscope stabilization in three dimensions using image correlation [62]).

Additional considerations in the development of a system include user control of illumination intensity (achievable with a combination of computer controlled shutters, filter revolvers containing neutral density filters and internal or external acousto-optic modulators to the laser modules). Excitation laser lines ideally should have a sufficient power output to achieve a sample illumination intensity of 10^7–10^9 W/m^2 [29, 30], in practice laser modules with 100–400 mW of max output power are suitable. Often the illumination spot consists of a non-uniform (typically Gaussian) power distribution, which may be adjusted by passing the beam through a precisely aligned aperture and only allowing a central, more uniform, part of the beam profile to propagate. The most useful illumination configuration is somewhere between the extremes of widefield and TIRF, with both highly inclined (HILO; [59]) and light sheet illumination [63] being good options for thick samples like isolated myocytes. Of the two, HILO is our favourite as it is easy to implement and is compatible with standard slide mounting techniques. It offers an acceptable compromise between far-field imaging capabilities (unlike TIRF) and better imaging contrast than in widefield because of the ~3–5 μm-thick axial thickness of illumination.

Multi-colour dSTORM protocols may vary depending on the fluorophores and samples of interest. Straightforward dual-colour dSTORM is achieved by using two fluorophores with overlapping absorption spectra which allow simultaneous excitation by a single laser line, as outlined above. A single illumination line minimises chromatic shifts between planes of illumination and can be implemented easily with a single long-pass dichroic filter. Separating the emission from the different fluorophores from within the same image series however requires an emission splitting device which uses a dichroic mirror and a train of mirrors to focus the two resulting versions of the image onto adjacent halves of the same camera. To avoid introducing any distortions at this splitter device, it is recommended that a thick-substrate dichroic mirror (to ensure flatness) is used. Any magnification differences between the two images can be physically corrected by placing a set of lenses on the two halves of the splitter or can be taken into account in the software analysis of the data. While this approach effectively halves the size of the imaging area, the multicolour dSTORM information is essentially captured in the same length of time required for a single colour image series.

3D super-resolution imaging with dSTORM can be achieved through a number of strategies. The most common approach is the 'PSF engineering' which aims to encode sub-micron-scale axial position of the emitter in relation to the focal plane by making the lateral shape of the PSF characteristic of this defocus. Among these, two methods have been predominantly used for imaging cardiomyocytes. Firstly, by positioning a weak cylindrical lens at a the Fourier plane in front of the detector, an astigmatism can be introduced to the PSF [64]. The second method, known as phase-ramp imaging is achieved by introducing a linear phase gradient across the midpoint of the objective rear aperture which splits the PSF into two lobes which shift in relation to each other depending on the sub-micron-scale defocus [40, 41].

Finally, no SMLM apparatus is complete without a computer which drives all or most of the aforementioned components. Vitally, the PC must support fast input ports (e.g. USB3 for rapid image acquisition from the camera) and sufficient disk space to record multiple datasets (each around 10,000–50,000 frames at a speed of $>$20 Hz in a 16-bit format, typical file sizes of several Gb), ideally using fast disk technology that supports sustained high write speeds, these days SSD technology and beyond. Most custom-built systems should consist of live analysis and display options which may require a powerful multi-core processor, sufficient memory and optionally a secondary graphics processing unit (GPU) to achieve this, all requirements that can be fulfilled with modern hardware at fairly moderate cost (in comparison to the costs of the other microscope components). Certainly, it is not an area where one should try to reduce costs by adopting a meagre system specification.

The basic components and how they fit together are schematically shown in Fig. 9a which illustrates a typical system layout.

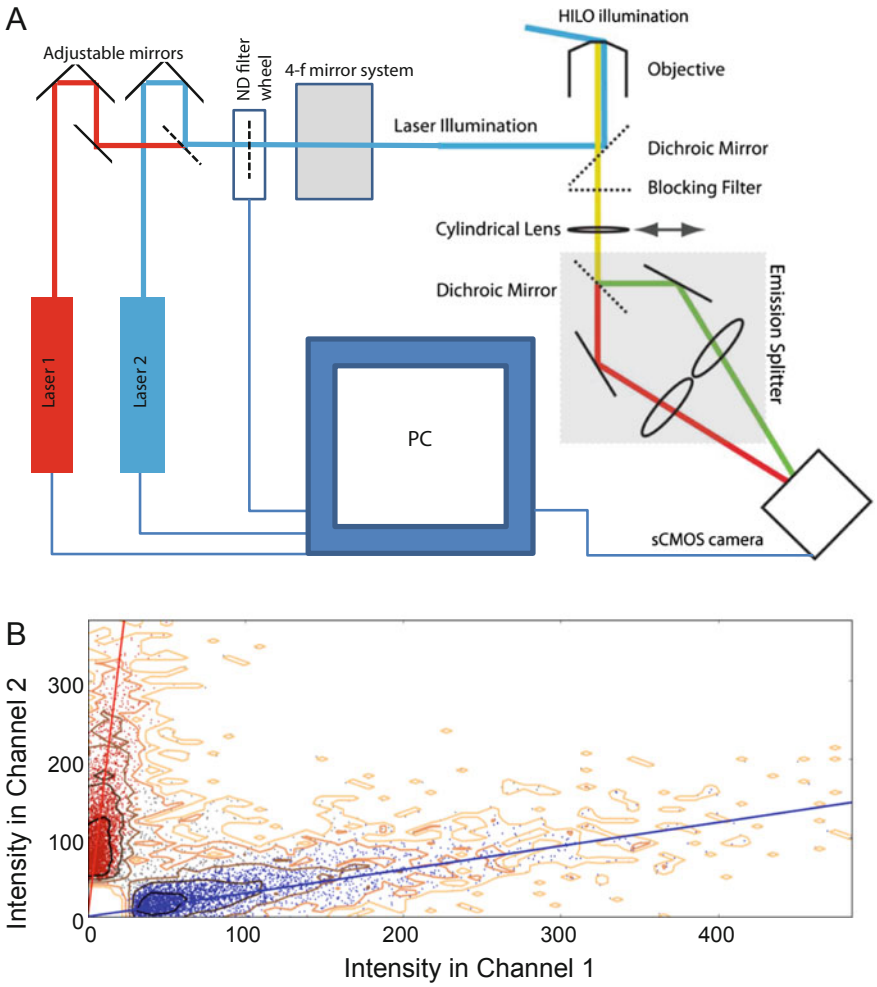

Fig. 9 The basic components of a multi-colour dSTORM-capable microscope system: (**a**) Shown are the configuration of two laser lines (chosen depending on the fluorophores of interest), a mirror train to align them into the microscope, a neutral density filter revolver for secondary control of the power input into the sample, a 4f optical relay system to allow decoupled adjustment of the incident light angle and lateral position in the sample, a dichroic mirror to separate excitation light from emission, a high NA objective which focuses the light into the sample in TIRF or HILO configuration, an emission filter to separate excitation and emission light wavelengths, an optional cylindrical lens (or alternative phase modulating insert, e.g. a phase ramp in PRILM) to enable 3D localisation, an emission splitter unit consisting of a dichroic mirror, additional mirrors and lenses to re-align and adjust the position and magnification of the split emission, a sensitive camera such as an sCMOS camera, a PC to perform image acquisition and control of the camera, laser light sources (power adjustment and internal shutters), filter wheels and (optionally) the three-dimensional positioning of the stage where the sample is mounted. *Re-drawn from Baddeley et al 2011 PLoS One.* (**b**) In dual-colour dSTORM, the image intensities of each event which had been split into the two halves of the camera are plotted against each other on a scattergram. Typically, the spectral signature of each fluorophore species forms a distinct point cloud and molecular identity can be assigned based on position of an event in the scattergram (red or blue), for details see *Baddeley et al 2011 PLoS One*

Image Analysis for Obtaining Super-Resolution Images

The image analysis is perhaps as important for super-resolution as the image acquisition. Nearly a decade-on from the invention of SMLM, a number of pre-tested programs and algorithms are available for free use. However, careful consideration to the fluorophore localisation procedure and its rationale is important for achieving the best resolution from the acquired data. The most reliable method that we have employed consists of two steps—the event detection and fitting. The detection involves a brief adaptive background estimation for each image frame (typically by averaging within a moving time window) which can be then subtracted to identify (i.e. detect) bright single molecule events that are unique to each frame. Once detected, a weighted least squares fit of a parametric model (e.g. a 2D Gaussian or more complex function for 3D localisation) is performed within a small (e.g. 11×11 pixel, depending on sampling and PSF size) local window centred on each detected event. This statistical approach to event fitting with the consideration of a rigorous noise model automatically computes variables that are additional to the x-y position of the marker (e.g. fit error and sigma of the model) which can be used for additional post-hoc filtering to retain only the in-focus and bright single-molecule events. In 3D dSTORM protocols that utilise the PSF engineering, the fitting may be performed based on a model of the depth-encoded PSF reconstructed from images of small sub-resolution (e.g. 100 nm Ø) fluorescent beads that are readily commercially available. In multi-colour imaging, the two facsimiles of the same event are fitted simultaneously on the two halves of the read-out image, often with the use of an alignment map that encodes and intrinsically corrects local shifts and magnification differences that often require prior calibration measurements [40, 41].

Detected events may be displayed by constructing a map of the x-y (and z) positions of the detected events. It may be necessary to post-filter events based on the extra parameters obtained in the fitting step. For example, somewhat clearly out of focus events may be discarded by filtering the events by the estimated diameters (sigma values when using Gaussian functions) of the fits. Similarly, stochastically-overlapping events (e.g. multiple events that are not resolvable in a given frame) can shift the localised position; these can be removed by excluding events whose apparent amplitude are larger than say the 99th percentile of the fit amplitude distribution. Alternatively, multi-emitter fitting approaches can be adopted in an attempt to correctly deal with overlapping emitter images [65]. If correct temporal sampling is achieved, most events will last multiple frames. Analysis of each image of the same event in consecutive frames as independent events is often problematic, especially if the data will be later interpreted for quantitative estimates. In these situations, images of the same event through consecutive frames can be coalesced (e.g. by averaging or integrating) into one event and as a by-product achieving a lower fit error. In multi-colour experiments, the pairs of the event images can be further analysed to plot the fit amplitudes in the two facsimiles of the same event to observe the characteristic ratio that is expected for each fluorophore species between the two images (Fig. 9b). Each event, appearing as a point in a ratio scattergram, is therefore assigned the spectral identity of the respective fluorophore which can be conducted in a statistically informed approach by calculating

the probability of belonging to species X using an appropriate model [40, 41]. In cases of distinctly-differing ratios, the effective crosstalk in this spectral unmixing process can be $<1\%$ [40, 41].

Post-processing based drift correction comes in two flavours—either using fiduciary markers such as gold beads embedded in the sample to track drift (e.g. [24]), or attempting to infer drift from the structure being imaged (e.g. [66]). Most open-source and commercially-available image analysis software contain algorithms that use one or both methods. However, it is noteworthy that sample drift or thermal drift of the apparatus components are often not linear and it may be difficult to accurately estimate drift trajectory, resulting in uncorrected motion blur. Therefore, it is vital that sources of drift are identified and addressed prior to or during image acquisition as much as possible.

Finally, the localised fluorophore maps need to be rendered into greyscale images that can reflect the nanometre-scale local fluorophore density and/or the localisation error which creates uncertainty in the localisations. The most common method of rendering includes a Gaussian rendering where each point is convolved with a Gaussian kernel whose sigma is proportional to the localisation error. However, this Gaussian rendering sacrifices some resolution, particularly apparent at closely-spaced structures [67]. This is overcome by improved rendering methods, such as one based on an iterative Delaunay triangulation [67] which we frequently use for cardiac muscle super-resolution imaging. For analysis of event data (e.g. for co-localisation analysis or quantification of cluster sizes), it may be useful to construct a binary mask of the super-resolution data as a further processing of the greyscale rendering, here used to delineate clusters in the data. Figure 10 illustrates this visualisation procedure with an example of RyR1 imaging in a rat skeletal muscle tissue section.

Considerations in Achieving Super-Resolution Imaging

Achieving the super-resolution promised by SMLM requires consideration of several aspects with respect to sample preparation and imaging protocols. The effective resolution in the image is ultimately dependent on the localisation error and the effective labelling density of the underlying structure. The localisation error is approximately proportional to $\sigma/\sqrt{N}$ where σ is the standard deviation of the best fit Gaussian (i.e. the diameter of the PSF) and N the number of photons collected from the event [68]. Maximising N is typically achieved by increasing the excitation (which speeds up the electronic transition of the fluorophores between S_0 and S_1), integrating events lasting multiple frames, chemically increasing the lifetime of the fluorophore events and generally using an optical detection path that aims to maximise collection efficiency. However, in a sample that has substantial background fluorescence (e.g. very high labelling densities or out of focus fluorescence, typically in 'thick' samples) the localisation error rises with the background intensity [69]. As a practical guide, we have demonstrated that SMLM is compatible with isolated cardiomyocytes [29, 30, 50–52], single skeletal muscle fibres [70] and 'thin'

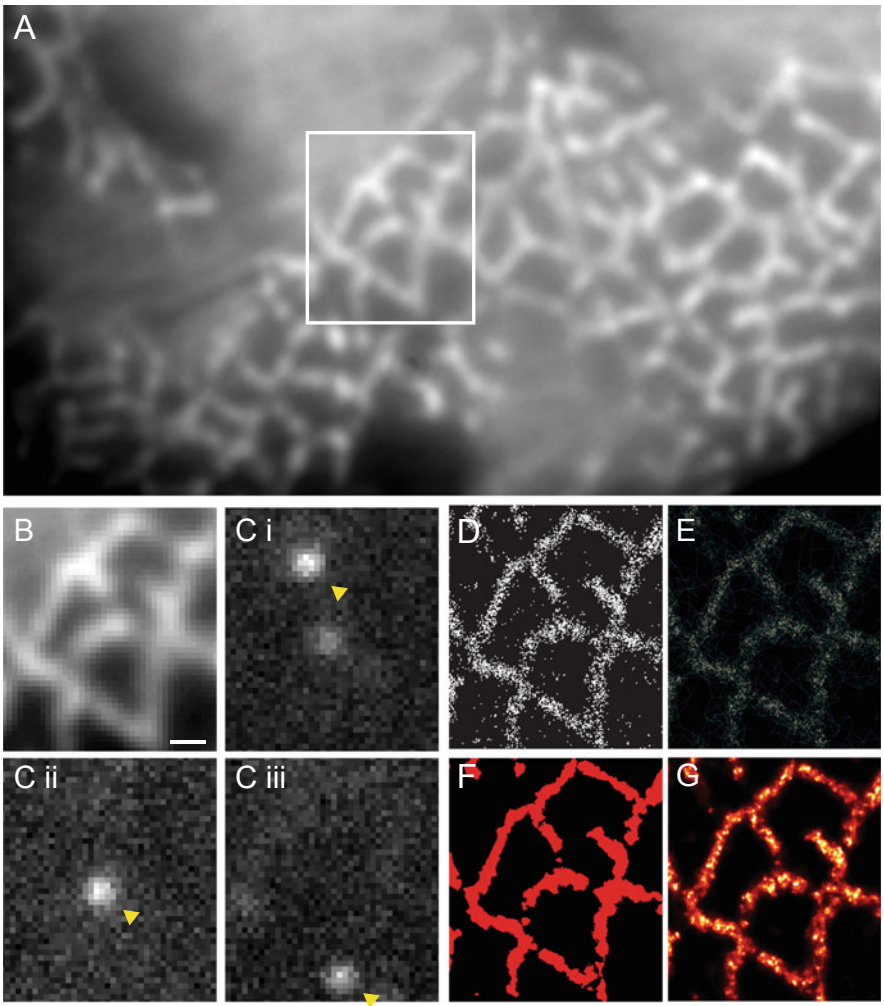

Fig. 10 Visualisation of dSTORM data. (**a**) An example of RyR1 labelling in a transverse tissue section of a rat EDL muscle visualised using HILO illumination. (**b**) Magnified view of the region in panel A indicated by the box. (**c** i–iii) Flashes of fluorescence (arrowheads) corresponding to single molecule photoblinking within the same region that were localised. (**d**) Indicated by the white dots, are the localized single molecule events in dSTORM. (**e**) For visualization and binarization of this data, Delaunay triangulation was performed on the point data. (**f**) The triangles longer than the effective image resolution (30 nm) were discarded while shorter triangles were merged into a binary mask that reliably captured areas of positive labelling. (**g**) These localization data could also be rendered into greyscale images using the algorithm previously described by Baddeley et al. [67] where intensity was proportional to the local event density. Scale bar 200 nm. *Adapted from Jayasinghe et al 2014 J Royal Soc Interface*

(by confocal standards, i.e. 5–10 μm) tissue sections of ventricular muscle [11, 71] to achieve ~30–60 nm resolution in well labelled samples.

Related to the last point, a potentially serious and frequently encountered issue is "under-labelling" which reduces the detectability of nanoscale features of t-tubules. This becomes a particularly concerning issue during 3D SMLM where sufficient fluorophore densities in the axial dimension are also critical for achieving a high-quality super-resolution 3D image. Figure 11 illustrates this point by showing a simulation that summarises the effect of labelling density and background fluorescence on the reconstructed super-resolution image. It is noteworthy that in an equivalent confocal micrograph under each condition, the structural features appear often unaffected and mainly result in a dimmer image (which will, however, affect the signal-to-noise ratio, but may be overcome to some extent by "turning up the laser", increasing integration time or slightly opening the pinhole). This underscores the greater emphasis that SMLM places on the quality of the samples for achieving super-resolution. Table 2 collates a summary of (our view on) advantages, technical considerations and limitations of SMLM with a particular view towards imaging in muscle.

Considerations in Quantifying Structures and Labelling Densities

Aside from the visual improvement in the contrast and the level of spatial detail as a result of the improved resolution in SMLM, these images hold a great capacity for quantitative analysis. We and others have demonstrated this repeatedly in quantifying protein densities, co-localisation and clustering properties (e.g. [11, 29, 30, 50, 51, 72]). Briefly, we here outline a few key considerations that need to be made to ensure that the analysis (a) is meaningful for addressing the biological question at hand and (b) captures the uncertainties of the imaging experiment.

- The resolution achieved in the super-resolution images must be assessed and used as a margin of uncertainty in the measurements made. The simplest way to assess this is to examine the distribution of localisation fit error values whose mean multiplied by a factor of ~2.4 is an upper bound to the resolution of the image. A more precise method is the Fourier ring correlation protocol [73] which is emerging as a measure of data quality assurance that is requested by many journals.
- Creating binary masks of labelled regions is more straightforward than in diffraction-limited data (e.g. punctate RyR labelling in [18]). Exploiting the essentially 'background-free' nature of the super-resolution data, a global threshold can be used for distinguishing labelled regions from background. However, a consistent criterion needs to be adopted (e.g., a method based on Delaunay triangulation [29, 30], Voronoï tessellation [74] or intensity percentile thresholding [11]) to minimise user bias.

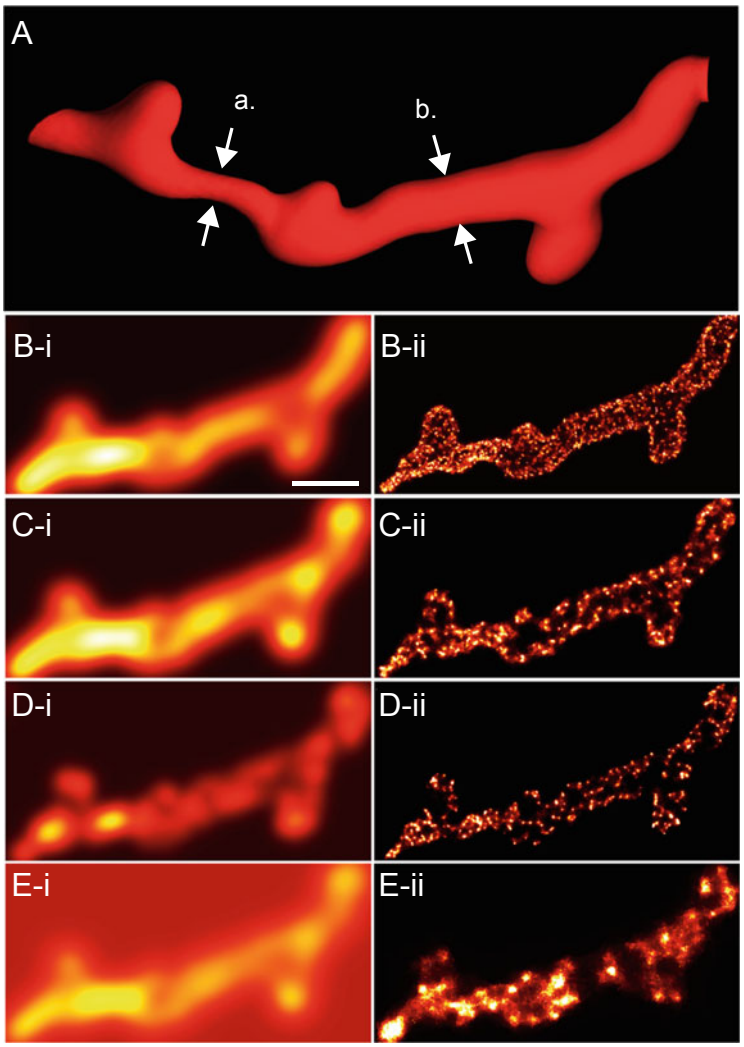

Fig. 11 Simulating the effect of labelling densities and background fluorescence on diffraction-limited and SMLM images. (**a**) A phantom t-tubule with a varying diameter (a = 130 nm and b = 280 nm) and a 20 nm-thick layer of fluorescent markers (similar to the combined thickness of a layer of primary and secondary antibodies bound to a t-tubular protein; e.g. caveolin-3) is simulated in (i) confocal micrographs and (ii) typical 2D dSTORM images. Images were simulated for labelling densities of (**b**) 0.12/nm^2, typical of very high fluorophore densities, (**c**) 0.008/nm^2, typically achieved in experimental samples and (**d**) 0.0005/nm^2 to simulate a 15-fold poorer labelling than typical. Notice the gradual loss of detail in the dSTORM images with the diminishing labelling density and little observable difference between the confocal images (**b**-i, **c**-i). To simulate the effect of higher background intensity (**e**), the background intensity was set to 50% of the foreground intensity and a foreground labelling density comparable to the simulation in panel (**c**). Notice the lack of detail in the dSTORM image (**e**-ii compared to **c**-ii) while little change is seen in the morphologies in the confocal images (**e**-i compared to **c**-i) apart from the increase in background intensity. Note the background rejection in the dSTORM image (**e**-ii) which is characteristic of SMLM. Scale bar: 500 nm. *Adapted from Jayasinghe et al. 2014 Eur J Trans Myol*

Table 2 Features of localisation microscopy techniques and their advantages and limitations with particular emphasis on imaging cardiac/skeletal myocytes

Features	Advantages	Limitations
Nanometre resolution across sub-millimetre sized areas	• >10 fold improvement over diffraction-limited fluorescence techniques • Direct measurement of subcellular structures • Minimises over-estimation of protein co-localisation due to optical blurring	• Resolution is only limited by detectable light yield from a single event, size of the fluorescent label/complex and the local density of the fluorescent probes.
Can be performed in aqueous and non-aqueous sample environments	• Compatible with correlative imaging with EM and other light microscopies • Minimise shrinkage artefacts • Customisable mounting medium to optimise photoswitching	–
Fluorophore photoswitching kinetics are adjustable	• Can be modulated by excitation intensity, chemical constituents in the mounting buffer and/or a secondary activation laser. • Optimal photoswitching rate can be achievable depending on the densities of the underlying fluorophores in the samples. • Ability to improve localisation accuracy by avoiding simultaneous photoswitching of overlapping fluorophores or suppressing background/out of focus molecules	• Abbreviating the fluorophore ON time further than a few milliseconds reduces photon yield, compromising the localisation accuracy. • Prolonging the ON and/or OFF time prolongs the image acquisition time and the image file size. The latter may limit the speed of real-time image reconstruction. • Potentially many parameters and variables to choose from; may be confusing to non-specialist users
Image is generated based on localised map of fluorophore position and localisation error	• Images are (in principle) quantifiable for *in situ* biochemical analysis • Minimises geometry-dependent non-linearities in fluorescence intensity in diffraction-limited imaging • Robust clustering or image binerisation methods based on local event densities	• Quantifiability of image data hinges on accurate localisation of overlapping events and correcting for local fluorophore density dependence of repeated photoswitching or limited yields of the molecules.
Single molecule events consist of a unique spectral signature	• Spectral filtering can 'unmix' between multiple fluorophores or autofluorescence to achieve greater specificity in visualising the target structure.	-

(continued)

Table 2 (continued)

Features	Advantages	Limitations
Reconstructed greyscale images are "background free"	• More robust binarisation of images • Local intensity is less dependent on gradients/ patterns in the background compared to standard fluorescence microscopies	• Any background fluorescence limits localisation accuracy (hence, resolution) • Non-specific binding of fluorescent probes or antibodies are indistinguishable from specific binding; hence requiring appropriate control experiments (an issue common to all marker binding methods)
Ability to resolve structures in "thick" samples	• Compatible with immunocytochemistry and tissue samples sectioned with standard microtomes (typically 10–20 μm in thickness)	• Light scattering, spherical aberration and out of focus fluorescence typically seen in thick samples diminish the localisation accuracy. Therefore, thin samples are ideal (e.g. cultured cells). The native t-tubule structure is poorly preserved in cultured myocytes or myoblasts.
3D localisation	• Suitable for resolving the three-dimensional complexities of t-tubles	• Thin samples (<10 μm) with dense t-tubule labelling with low background fluorescence work best.
Photoswitchability of endogenous, genetically encoded or introduced fluorophores in aqueous physiological saline environments	• Compatible with real-time imaging t-tubules in living/ functional preparations • Conducive to photo-tracking of labelled receptor/protein/ lipid mobility in t-tubules	• Photodamage to the cells/ fibres from prolonged intense light exposure and oxidants generated from the photoswitching (but yet to be quantified if any worse than other imaging approaches) • Spatial distortions from drift or local contractures of the cells are difficult to correct for. • Visualisation of fast events (protein trafficking, t-tubule membrane remodelling) may be limited by fluorophore photobleaching and photoswitching rates.

Adapted from Jayasinghe et al. 2014 Eur J Trans Myol

- Morphology of substructure within densely-labelled regions may need to be verified with the use of an independent label (e.g. separate antibody with a spectrally-different fluorophore). Non-agreement of morphologies can confirm that such substructure is the result of the stochastic nature of the photoswitching and antibody binding.

- Co-localisation measurements should ideally be stated as a fraction of the overall target population [11, 50, 51]. Such a measure is easier to interpret than the co-clustering algorithms [75] or Pierson's correlation coefficient, in our view. However, it should be noted that co-localisation is a complex subject where strong opinions abound.
- The uncertainties in the co-localisation analysis (for example, the maximum detectable co-localisation due to marker binding variability or spatial error due to the resolution uncertainty) should be demonstrated with control experiments and considered in the discussion.
- The local event density within a labelled patch can be proportional to the underlying protein distribution. However, estimating this will require adopting a very strict imaging protocol that standardises the time of image acquisition, imaging parameters such as excitation light intensity, thiol and oxygen availability within the sample, depth of imaging, post-hoc event filtering protocols and the three-dimensional shape/orientation of the labelled nanodomains [32, 33]. The methods of quantifying underlying target density based on single molecule event numbers depend crucially on the photoswitching properties adopted. For example, the same dSTORM fluorophore may re-appear up to 10-times before being permanently photobleached [58] while this cyclical transition of electronic states in PALM fluorophores is less pronounced [76]. This means that some methods may be more susceptible to over-counting than others. It also needs to be considered fluorescent proteins used most-commonly in PALM can have a detection efficiency significantly less than 100% (e.g. ~80% for GFP [77]). Therefore, these uncertainties may require additional corrections.
- In connection with the previous point, quantitative imaging and super-resolution are still rapidly developing and introducing new methods. Here, we briefly mention the recently introduced DNA-PAINT paradigm [78] that may lead to a quantitative interpretation less prone to artefacts as has been recently proposed (qPAINT [79]). We expect this trend to have a broad impact on quantitative cardiac imaging.
- Where orientation of the structure or reference to a local compartment is uncertain, it is advisable to adopt a correlative imaging approach. For example, a correlative EM/dSTORM experiment can verify spatial scale of the observed structures such as the size of the nuclear pore complex [80] or correlative confocal/dSTORM can provide a reference to the 3D orientation of t-tubule extensions in interpreting RyR cluster sizes and shapes [35].

Outlook

Predicting the detailed further development of super-resolution (even if limited to the area of cardiac imaging) is bound to fail just as any other predictions of the future generally do. We will therefore only mention a few general trends that we currently see and that we expect to have impacts on cardiac studies in the near future.

- The safe bet: super-resolution is going to become more and more pervasive in biological research and cardiac investigations will be no exception; it seems fairly safe to assume that one or other type of super-resolution instrument and technique will be as widely employed as confocal microscopy is now. In connection with this point, the differences are becoming already blurred as illustrated by the recent introduction of scanning microscopy with an array detector, variously known as image scanning microscopy (ISM) [81], Airy scanning [82] etc. These instruments mostly behave like a confocal microscope but are capable of increasing spatial resolution by nearly a factor of 2 in all dimensions; this may seem moderate but can reveal critical additional detail in many practically relevant scenarios.
- In connection with this point, we have not focussed on functional super-resolution imaging in this chapter; this is an area where rapid development is ongoing and new modalities, tricks and approaches are appearing all the time. The main challenge is the time resolution that may be required which can be as demanding as a few milliseconds. Techniques that increase spatial resolution only moderately and trade that for time resolution will be the easiest to establish in practice (which tends to be a truism in imaging—one can trade spatial resolution for time resolution and vice versa). ISM is an example that comes to mind and other structured illumination methods will have similar advantages; STED microscopy, particularly if performed in small regions of interest is another possibility, particularly with ongoing developments in both instrument simplification and improved fluorochromes (both organic dyes and fluorescent proteins). It seems likely that functional super-resolution imaging is an area in which we will see both rapid development and increased uptake by researchers.
- This chapter has focussed on immuno-labelling of largely fixed samples. Intrinsic labelling with genetically encoded fluorescent proteins is an attractive alternative and is well-developed from the point of view of super-resolution technology and suitable photo-switchable proteins [83]. A difficulty for those interested in physiological detail has been that short-term culture of cardiac myocytes for transient expression is still often associated with cellular re-modelling and de-differentiation that makes particularly the study of nanoscale structural detail problematic. The development of genetically modified animal strains, improved whole-organ and whole-animal transfection approaches will likely all help to alleviate this limitation and provide in addition an excellent synergy for functional super-resolution imaging.
- New hybrid and flexible methods: as mentioned new concepts in light-microscopy have been abundant in recent years and combinations of approaches for new super-resolution imaging modalities will keep springing up in many areas. These will be targeted to improve time resolution, signal-to-noise ratios, ease of use and compatibility with more complex biological preparations (e.g. the whole heart). This will likely include (and already does) approaches such as light-sheet methods, new marker technologies as well as continuously improving imaging hardware in the form of cameras, light shaping tools and computer power.

Conclusion

This chapter summarises and discusses advancements in understanding cardiac cell biology by employing emerging super-resolution methods with a particular focus on SMLM. The improvement in the resolution offers unprecedented levels of insight into the nanoscale molecular arrangements in cardiac myocytes, in particular proteins central for EC coupling. With the emergence of versatile commercial instruments and protocols to perform super-resolution imaging, it may be tempting to replace most other existing microscopy techniques with novel super-resolution approaches. As outlined above, achieving resolution improvement in SMLM methods requires taking the full range of factors (hardware, mounting media, fluorophores, sample properties and analysis parameters) into proper consideration. We regularly inspect 'super-resolution' images recorded by inexperienced or not well trained users that have resolution no better than the original diffraction-limited techniques. The emerging trend of using resolution tests may need to be embraced as a quality assurance and validation measure, although no existing resolution test procedure is without its own intrinsic issues that can result from incorrect application or interpretation. A slightly more challenging (and probably not always feasible) approach that also can improve biological insight is the use of correlative imaging to provide, in addition to super-resolution data, further information from other imaging modalities, especially EM. As a bottom line, SMLM, when controlled well, can provide a level of quantitative information that generally surpasses other diffraction-limited optical microscopies (and at least some of the other super-resolution approaches). In general, super-resolution imaging approaches, regardless of the specific modality chosen, hold exciting future possibilities for many areas of cardiac biology and cardiac biophysics.

References

1. Bers DM. Cardiac excitation-contraction coupling. Nature. 2002;415(6868):198–205.
2. Asghari P, Scriven DR, Sanatani S, Gandhi SK, Campbell AI, Moore ED. Nonuniform and variable arrangements of ryanodine receptors within mammalian ventricular couplons. Circ Res. 2014;115(2):252–62.
3. Franzini-Armstrong C, Protasi F. Ryanodine receptors of striated muscles: a complex channel capable of multiple interactions. Physiol Rev. 1997;77(3):699–729.
4. Yin CC, Lai FA. Intrinsic lattice formation by the ryanodine receptor calcium-release channel. Nat Cell Biol. 2000;2(9):669–71.
5. Soeller C, Cannell MB. Numerical simulation of local calcium movements during L-type calcium channel gating in the cardiac diad. Biophys J. 1997;73(1):97–111.
6. Stern MD. Theory of excitation-contraction coupling in cardiac muscle. Biophys J. 1992;63 (2):497–517.
7. Fawcett DW, McNutt NS. The ultrastructure of the cat myocardium. I. Ventricular papillary muscle. J Cell Biol. 1969;42(1):1–45.
8. Franzini-Armstrong C, Protasi F, Ramesh V. Shape, size, and distribution of Ca(2+) release units and couplons in skeletal and cardiac muscles. Biophys J. 1999;77(3):1528–39.

9. Soeller C, Cannell MB. Examination of the transverse tubular system in living cardiac rat myocytes by 2-photon microscopy and digital image-processing techniques. Circ Res. 1999;84 (3):266–75.
10. Soeller C, Crossman D, Gilbert R, Cannell MB. Analysis of ryanodine receptor clusters in rat and human cardiac myocytes. Proc Natl Acad Sci U S A. 2007;104(38):14958–63.
11. Hou Y, Jayasinghe I, Crossman DJ, Baddeley D, Soeller C. Nanoscale analysis of ryanodine receptor clusters in dyadic couplings of rat cardiac myocytes. J Mol Cell Cardiol. 2015;80:45–55.
12. Song LS, Sobie EA, McCulle S, Lederer WJ, Balke CW, Cheng H. Orphaned ryanodine receptors in the failing heart. Proc Natl Acad Sci U S A. 2006;103(11):4305–10.
13. Wei S, Guo A, Chen B, Kutschke W, Xie YP, Zimmerman K, Weiss RM, Anderson ME, Cheng H, Song LS. T-tubule remodeling during transition from hypertrophy to heart failure. Circ Res. 2010;107(4):520–31.
14. Crossman DJ, Ruygrok PN, Soeller C, Cannell MB. Changes in the organization of excitation-contraction coupling structures in failing human heart. PLoS One. 2011;6(3):e17901.
15. Veratti E. Investigations on the fine structure of striated muscle fiber read before the Reale Istituto Lombardo, 13 March 1902. J Biophys Biochem Cytol. 1961;10(4, Suppl):1–59.
16. Guo A, Zhang C, Wei S, Chen B, Song LS. Emerging mechanisms of T-tubule remodelling in heart failure. Cardiovasc Res. 2013;98(2):204–15.
17. Scriven DR, Dan P, Moore ED. Distribution of proteins implicated in excitation-contraction coupling in rat ventricular myocytes. Biophys J. 2000;79(5):2682–91.
18. Jayasinghe ID, Cannell MB, Soeller C. Organization of ryanodine receptors, transverse tubules, and sodium-calcium exchanger in rat myocytes. Biophys J. 2009;97(10):2664–73.
19. Scriven DR, Asghari P, Schulson MN, Moore ED. Analysis of Cav1.2 and ryanodine receptor clusters in rat ventricular myocytes. Biophys J. 2010;99(12):3923–9.
20. Soeller C, Jayasinghe ID, Li P, Holden AV, Cannell MB. Three-dimensional high-resolution imaging of cardiac proteins to construct models of intracellular Ca^{2+} signalling in rat ventricular myocytes. Exp Physiol. 2009;94(5):496–508.
21. Abbe E. Beiträge zur Theorie des Mikroskops und der mikroskopischen Wahrnehmung. Arch Mikrosk Anat. 1873;9(1):413–8.
22. Landstrom AP, Kellen CA, Dixit SS, van Oort RJ, Garbino A, Weisleder N, Ma J, Wehrens XH, Ackerman MJ. Junctophilin-2 expression silencing causes cardiocyte hypertrophy and abnormal intracellular calcium-handling. Circ Heart Fail. 2011;4(2):214–23.
23. Jost A, Heintzmann R. Superresolution multidimensional imaging with structured illumination microscopy. Annu Rev Mat Res. 2013;43(1):261–82.
24. Betzig E, Patterson GH, Sougrat R, Lindwasser OW, Olenych S, Bonifacino JS, Davidson MW, Lippincott-Schwartz J, Hess HF. Imaging intracellular fluorescent proteins at nanometer resolution. Science. 2006;313(5793):1642–5.
25. Rust MJ, Bates M, Zhuang X. Sub-diffraction-limit imaging by stochastic optical reconstruction microscopy (STORM). Nat Methods. 2006;3(10):793–5.
26. Betzig E. Single molecules, cells, and super-resolution optics (Nobel Lecture). Angew Chem Int Ed. 2015;54(28):8034–53.
27. Klein T, Proppert S, Sauer M. Eight years of single-molecule localization microscopy. Histochem Cell Biol. 2014;141(6):561–75.
28. Toomre D, Bewersdorf J. A new wave of cellular imaging. Annu Rev Cell Dev Biol. 2010;26:285–314.
29. Baddeley D, Jayasinghe ID, Cremer C, Cannell MB, Soeller C. Light-induced dark states of organic fluochromes enable 30 nm resolution imaging in standard media. Biophys J. 2009a;96 (2):L22–4.
30. Baddeley D, Jayasinghe ID, Lam L, Rossberger S, Cannell MB, Soeller C. Optical single-channel resolution imaging of the ryanodine receptor distribution in rat cardiac myocytes. Proc Natl Acad Sci U S A. 2009b;106(52):22275–80.

31. Wagner E, Lauterbach MA, Kohl T, Westphal V, Williams GS, Steinbrecher JH, Streich JH, Korff B, Tuan HT, Hagen B, Luther S, Hasenfuss G, Parlitz U, Jafri MS, Hell SW, Lederer WJ, Lehnart SE. Stimulated emission depletion live-cell super-resolution imaging shows proliferative remodeling of T-tubule membrane structures after myocardial infarction. Circ Res. 2012;111(4):402–14.
32. Jayasinghe ID, Clowsley AH, Munro M, Hou Y, Crossman DJ, Soeller C. Revealing t-tubules in striated muscle with new optical super-resolution microscopy techniques. Eur J Transl Myol. 2014a;25:4747.
33. Jayasinghe ID, Munro M, Baddeley D, Launikonis BS, Soeller C. Observation of the molecular organization of calcium release sites in fast- and slow-twitch skeletal muscle with nanoscale imaging. J R Soc Interface. 2014b;11(99)
34. Chen-Izu Y, McCulle SL, Ward CW, Soeller C, Allen BM, Rabang C, Cannell MB, Balke CW, Izu LT. Three-dimensional distribution of ryanodine receptor clusters in cardiac myocytes. Biophys J. 2006;91(1):1–13.
35. Crossman DJ, Hou Y, Jayasinghe I, Baddeley D, Soeller C. Combining confocal and single molecule localisation microscopy: a correlative approach to multi-scale tissue imaging. Methods. 2015;88:98–108.
36. Folling J, Bossi M, Bock H, Medda R, Wurm CA, Hein B, Jakobs S, Eggeling C, Hell SW. Fluorescence nanoscopy by ground-state depletion and single-molecule return. Nat Methods. 2008;5(11):943–5.
37. Sobie EA, Guatimosim S, Gomez-Viquez L, Song LS, Hartmann H, Saleet Jafri M, Lederer WJ. The Ca^{2+} leak paradox and rogue ryanodine receptors: SR Ca^{2+} efflux theory and practice. Prog Biophys Mol Biol. 2006;90(1-3):172–85.
38. Hayashi T, Martone ME, Yu Z, Thor A, Doi M, Holst MJ, Ellisman MH, Hoshijima M. Three-dimensional electron microscopy reveals new details of membrane systems for Ca^{2+} signaling in the heart. J Cell Sci. 2009;122(Pt 7):1005–13.
39. Bers DM, Stiffel VM. Ratio of ryanodine to dihydropyridine receptors in cardiac and skeletal muscle and implications for E-C coupling. Am J Physiol. 1993;264(6 Pt 1):C1587–93.
40. Baddeley D, Cannell M, Soeller C. Three-dimensional sub-100 nm super-resolution imaging of biological samples using a phase ramp in the objective pupil. Nano Res. 2011a;4(6):589–98.
41. Baddeley D, Crossman D, Rossberger S, Cheyne JE, Montgomery JM, Jayasinghe ID, Cremer C, Cannell MB, Soeller C. 4D super-resolution microscopy with conventional fluorophores and single wavelength excitation in optically thick cells and tissues. PLoS One. 2011b;6(5):e20645.
42. Murphy RM, Dutka TL, Horvath D, Bell JR, Delbridge LM, Lamb GD. Ca^{2+}-dependent proteolysis of junctophilin-1 and junctophilin-2 in skeletal and cardiac muscle. J Physiol. 2013;591(Pt 3):719–29.
43. Wang W, Landstrom AP, Wang Q, Munro ML, Beavers D, Ackerman MJ, Soeller C, Wehrens XH. Reduced junctional Na+/Ca^{2+}-exchanger activity contributes to sarcoplasmic reticulum Ca^{2+} leak in junctophilin-2-deficient mice. Am J Physiol Heart Circ Physiol. 2014;307(9):H1317–26.
44. Guo A, Zhang X, Iyer VR, Chen B, Zhang C, Kutschke WJ, Weiss RM, Franzini-Armstrong C, Song L-S. Overexpression of junctophilin-2 does not enhance baseline function but attenuates heart failure development after cardiac stress. Proc Natl Acad Sci. 2014;111(33):12240–5.
45. Franzini-Armstrong C, Peachey LD. A modified Golgi black reaction method for light and electron microscopy. J Histochem Cytochem. 1982;30(2):99–105.
46. Cannell MB, Crossman DJ, Soeller C. Effect of changes in action potential spike configuration, junctional sarcoplasmic reticulum micro-architecture and altered t-tubule structure in human heart failure. J Muscle Res Cell Motil. 2006;27(5-7):297–306.
47. Sachse FB, Torres NS, Savio-Galimberti E, Aiba T, Kass DA, Tomaselli GF, Bridge JH. Subcellular structures and function of myocytes impaired during heart failure are restored by cardiac resynchronization therapy. Circ Res. 2012;110(4):588–97.

48. Shang W, Lu F, Sun T, Xu J, Li LL, Wang Y, Wang G, Chen L, Wang X, Cannell MB, Wang SQ, Cheng H. Imaging Ca^{2+} nanosparks in heart with a new targeted biosensor. Circ Res. 2014;114(3):412–20.
49. Guo A, Song LS. AutoTT: automated detection and analysis of T-tubule architecture in cardiomyocytes. Biophys J. 2014;106(12):2729–36.
50. Jayasinghe I, Crossman D, Soeller C, Cannell M. Comparison of the organization of T-tubules, sarcoplasmic reticulum and ryanodine receptors in rat and human ventricular myocardium. Clin Exp Pharmacol Physiol. 2012a;39(5):469–76.
51. Jayasinghe ID, Baddeley D, Kong CH, Wehrens XH, Cannell MB, Soeller C. Nanoscale organization of junctophilin-2 and ryanodine receptors within peripheral couplings of rat ventricular cardiomyocytes. Biophys J. 2012b;102(5):L19–21.
52. Wong J, Baddeley D, Bushong EA, Yu Z, Ellisman MH, Hoshijima M, Soeller C. Nanoscale distribution of ryanodine receptors and caveolin-3 in mouse ventricular myocytes: dilation of t-tubules near junctions. Biophys J. 2013;104(11):L22–4.
53. Pinali C, Kitmitto A. Serial block face scanning electron microscopy for the study of cardiac muscle ultrastructure at nanoscale resolutions. J Mol Cell Cardiol. 2014;76C:1–11.
54. Hess ST, Girirajan TP, Mason MD. Ultra-high resolution imaging by fluorescence photoactivation localization microscopy. Biophys J. 2006;91(11):4258–72.
55. Heilemann M, van de Linde S, Schüttpelz M, Kasper R, Seefeldt B, Mukherjee A, Tinnefeld P, Sauer M. Subdiffraction-resolution fluorescence imaging with conventional fluorescent probes. Angew Chem Int Ed. 2008;47(33):6172–6.
56. van de Linde S, Sauer M. How to switch a fluorophore: from undesired blinking to controlled photoswitching. Chem Soc Rev. 2014;43(4):1076–87.
57. Vaughan JC, Dempsey GT, Sun E, Zhuang X. Phosphine quenching of cyanine dyes as a versatile tool for fluorescence microscopy. J Am Chem Soc. 2013;135(4):1197–200.
58. Dempsey GT, Vaughan JC, Chen KH, Bates M, Zhuang X. Evaluation of fluorophores for optimal performance in localization-based super-resolution imaging. Nat Methods. 2011;8(12):1027–36.
59. Tokunaga M, Imamoto N, Sakata-Sogawa K. Highly inclined thin illumination enables clear single-molecule imaging in cells. Nat Methods. 2008;5(2):159–61.
60. Huang F, Hartwich TMP, Rivera-Molina FE, Lin Y, Duim WC, Long JJ, Uchil PD, Myers JR, Baird MA, Mothes W, Davidson MW, Toomre D, Bewersdorf J. Video-rate nanoscopy using sCMOS camera-specific single-molecule localization algorithms. Nat Methods. 2013;10(7):653–8.
61. Lin R, Clowsley AH, Jayasinghe I, Soeller C. Single-molecule localization microscopy with sCMOS cameras. Biophotonics. 2016;110:161a.
62. McGorty R, Kamiyama D, Huang B. Active microscope stabilization in three dimensions using image correlation. Optic Nanosc. 2013;2(1):3. https://doi.org/10.1186/2192-2853-1182-1183.
63. Cella Zanacchi F, Lavagnino Z, Faretta M, Furia L, Diaspro A. Light-sheet confined super-resolution using two-photon photoactivation. PLoS One. 2013;8(7):e67667.
64. Huang B, Jones SA, Brandenburg B, Zhuang X. Whole-cell 3D STORM reveals interactions between cellular structures with nanometer-scale resolution. Nat Methods. 2008;5(12):1047–52.
65. Baddeley D. Efficient ROI selection for multi-emitter fitting approaches in single-molecule super-resolution microscopy. Biophys J. 2014;106(2):605a.
66. Mlodzianoski MJ, Schreiner JM, Callahan SP, Smolkova K, Dlaskova A, Santorova J, Jezek P, Bewersdorf J. Sample drift correction in 3D fluorescence photoactivation localization microscopy. Opt Express. 2011;19(16):15009–19.
67. Baddeley D, Cannell MB, Soeller C. Visualization of localization microscopy data. Microsc Microanal. 2010;16(1):64–72.
68. Mortensen KI, Churchman LS, Spudich JA, Flyvbjerg H. Optimized localization analysis for single-molecule tracking and super-resolution microscopy. Nat Methods. 2010;7(5):377–81.

69. Thompson RE, Larson DR, Webb WW. Precise nanometer localization analysis for individual fluorescent probes. Biophys J. 2002;82(5):2775–83.
70. Jayasinghe ID, Launikonis BS. Three-dimensional reconstruction and analysis of the tubular system of vertebrate skeletal muscle. J Cell Sci. 2013;126:4048.
71. Hou Y, Crossman DJ, Rajagopal V, Baddeley D, Jayasinghe I, Soeller C. Super-resolution fluorescence imaging to study cardiac biophysics: alpha-actinin distribution and Z-disk topologies in optically thick cardiac tissue slices. Prog Biophys Mol Biol. 2014;115:328.
72. Shim S-H, Xia C, Zhong G, Babcock HP, Vaughan JC, Huang B, Wang X, Xu C, Bi G-Q, Zhuang X. Super-resolution fluorescence imaging of organelles in live cells with photoswitchable membrane probes. Proc Natl Acad Sci. 2012;109(35):13978–83.
73. Banterle N, Bui KH, Lemke EA, Beck M. Fourier ring correlation as a resolution criterion for super-resolution microscopy. J Struct Biol. 2013;183(3):363–7.
74. Levet F, Hosy E, Kechkar A, Butler C, Beghin A, Choquet D, Sibarita JB. SR-Tesseler: a method to segment and quantify localization-based super-resolution microscopy data. Nat Methods. 2015;12:1065.
75. Rossy J, Cohen E, Gaus K, Owen DM. Method for co-cluster analysis in multichannel single-molecule localisation data. Histochem Cell Biol. 2014;141(6):605–12.
76. Shivanandan A, Deschout H, Scarselli M, Radenovic A. Challenges in quantitative single molecule localization microscopy. FEBS Lett. 2014;588(19):3595–602.
77. Ulbrich MH, Isacoff EY. Subunit counting in membrane-bound proteins. Nat Methods. 2007;4 (4):319–21.
78. Jungmann R, Avendano MS, Woehrstein JB, Dai M, Shih WM, Yin P. Multiplexed 3D cellular super-resolution imaging with DNA-PAINT and Exchange-PAINT. Nat Methods. 2014;11 (3):313–8.
79. Jungmann R, Avendano MS, Dai M, Woehrstein JB, Agasti SS, Feiger Z, Rodal A, Yin P. Quantitative super-resolution imaging with qPAINT. Nat Methods. 2016;13(5):439–42.
80. Loschberger A, van de Linde S, Dabauvalle MC, Rieger B, Heilemann M, Krohne G, Sauer M. Super-resolution imaging visualizes the eightfold symmetry of gp210 proteins around the nuclear pore complex and resolves the central channel with nanometer resolution. J Cell Sci. 2012;125(Pt 3):570–5.
81. Müller CB, Enderlein J. Image scanning microscopy. Phys Rev Lett. 2010;104(19):198101.
82. Huff J. The Airyscan detector from ZEISS: confocal imaging with improved signal-to-noise ratio and super-resolution. Nat Methods. 2015;12:1205.
83. Sengupta P, van Engelenburg SB, Lippincott-Schwartz J. Superresolution imaging of biological systems using photoactivated localization microscopy. Chem Rev. 2014;114(6):3189–202.

Caged Compounds: Applications in Cardiac Muscle Research

Ernst Niggli and Natalia Shirokova

Introduction

As detailed in several other chapters of this book, numerous imaging techniques have been devised to allow the observation of structures of the heart on all levels of organization and over a vast range of spatial resolutions, from the organ to the tissue level, but also with cellular, subcellular and even near molecular resolution [1]. When such imaging methods are applied to follow the evolution of structures or signals over time and with appropriate temporal resolution, they become very powerful tools to examine the cardiac function on all these levels of complexity.

In the context of in-vitro functional cardiac studies, it is often an advantageous experimental strategy to perturb a given steady-state and to analyze the readjustments of subsequent regulatory signaling events following such a perturbation. With this approach, it becomes possible to define the dynamics and kinetics of signaling networks in great detail, and to elucidate their pathways, cross-talks and interconnections.

A frequently employed procedure to perturb a biological system is by altering the concentration of a substrate, of a regulatory substance or of a pharmacological tool. The evolution of resulting functional modifications will provide information about the biological response downstream of that perturbation, but generally only when the experimental perturbation occurs much faster than the biological response. Unfortunately, concentration changes in experimental solutions are limited by slow convection and diffusion. When examining mechanisms on the cellular level, this limitation

E. Niggli (✉)
Department of Physiology, University of Bern, Bern, Switzerland
e-mail: niggli@pyl.unibe.ch

N. Shirokova
Department of Pharmacology, Physiology and Neuroscience, Rutgers, The State University of New Jersey, Newark, NJ, USA

L. Kaestner, P. Lipp (eds.), *Microscopy of the Heart*,
https://doi.org/10.1007/978-3-319-95304-5_4

becomes especially challenging when concentrations inside a cell should be changed experimentally.

The technique of light-induced concentration changes has been applied successfully to overcome such temporal limitations [2, 3]. The photo-conversion of an inactive chemically engineered precursor molecule (a.k.a. "caged compound") into its biologically active form is a powerful way to overcome this dilemma (see Fig. 1). The inert caged compound can be introduced into the cytosol of cells, ideally without causing any perturbation of the mechanism under study. After loading of the cell, a pulse or flash of light initiates the photo-conversion, and the biologically active compound is released into the cytosol. The quickness of the resulting concentration change is then only limited by the chemical kinetics of the light-induced breakdown, also called photochemical dark reaction, and not by convection or diffusion. With most available caged compounds, this leads to a very rapid concentration jump in the microsecond to millisecond time domain [4].

Since these concentration jumps are initiated by light, controlling the intensity, timing and location of the applied light provides researchers with a unique toolbox and multiple additional degrees of freedom to control experimental parameters

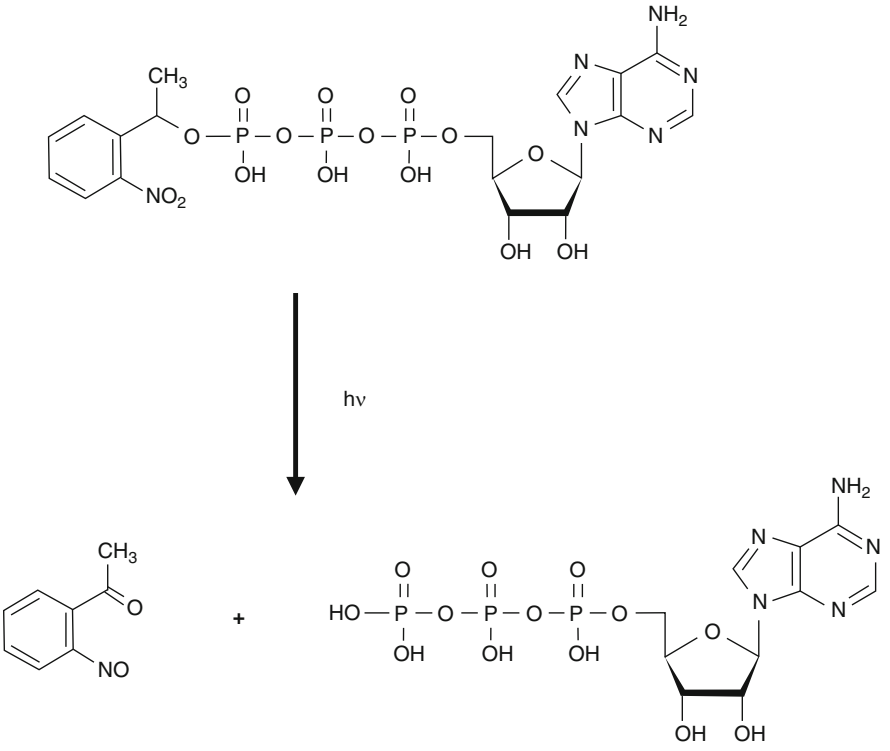

Fig. 1 Photolysis of NPE-caged ATP results in the production of ATP and the photolytic by-product nitrosoacetophenone

temporally and spatially. This still holds true for uncaging approaches in which the kinetics are not necessarily rapid (e.g. caged RNA, DNA and caged proteins).

Caged Compounds: General Properties

A large collection of compounds is commercially available from various suppliers. This includes several second messengers (such as Ca^{2+}, cAMP and $InsP_3$), caged Ca^{2+} buffers (e.g. Diazo-2), neurotransmitters (e.g. glutamate, GABA), metabolites (ATP, phosphate, NO, H^+), even caged fluorescent dyes (e.g. fluorescein). Sometimes, the same biologically active compound is available with an assortment of light sensitive caging groups, a feature which may change spectral as well as kinetic properties of the caged compound. In addition to commercially available chemicals, many caged compounds have been developed for specific applications by individual research groups. Some of these highly specialized niche products have been employed in cardiac muscle research (e.g. caged caffeine, caged SERCA inhibitors), and may be available upon request or in the framework of collaborations. Ideally, a caged compound will be biologically inactive (before photolysis), have a long shelf-life, a good efficiency (strong absorbance and high quantum yield) and fast kinetics. In addition, the photoproducts should have no toxicity and no off-target effects, neither biological nor chemical, a requirement which is often not perfectly fulfilled [5]. For each new experimental application of a caged compound, many of these requirements need to be tested under the conditions of an individual experimental protocol, with appropriate positive and negative control experiments.

Applications of Caged Compounds in Cardiac Muscle Research

Several comprehensive and detailed reviews have been published covering a wide application spectrum of caged compounds in numerous areas of research, in various tissues and cell types, but also details of their synthesis and photochemistry (for example see [2, 3, 6]). Here we will provide a short overview covering caged compounds particularly suitable and well established for cardiac muscle research. In this review, the chapters are individually structured for specific research applications (e.g. Ca^{2+} signaling, muscle contraction, regulation). Each chapter will briefly introduce compounds relevant for that particular application, followed by a summary of selected biological problems that were successfully tackled with approaches employing photolysis of caged compounds. The intention of this particular chapter structure is to facilitate new ideas for innovative applications of caged compounds among the readers, based on the knowledge of already established and proven protocols. Finally, we will provide a collection of generally applicable information related to the methods, techniques and potential problems when using these compounds.

Ca^{2+} Signaling

Caged Ca^{2+} Compounds

While photolysis of caged compounds has been used as a strategy to address a variety of biological problems and biophysical questions in cardiac muscle research, the vast majority of these studies was, in one way or another, concerned with cardiac muscle Ca^{2+} signaling and excitation-contraction (EC) coupling. EC-coupling refers to the cellular and subcellular events linking the electrical activity of the cardiomyocyte (i.e. the action potential) to the transient elevation of the cytosolic Ca^{2+} concentration, that enables mechanical activity and muscle contraction. Many of the Ca^{2+} signaling processes concerned are either driven, regulated or inactivated by changes of the Ca^{2+} concentration itself.

Nowadays, various caged compounds releasing Ca^{2+} are readily available (e.g. DM-nitrophen (a.k.a. DMNP-EDTA) [7], NP-EGTA [8], nitr-5 [9], see Table 1). Complementary to these tools, there is also a caged Ca^{2+} buffer (Diazo-2 [10]), which will rapidly reduce the Ca^{2+} concentration upon its photolysis, by releasing the Ca^{2+} buffer BAPTA [11]. Besides the commonly applicable quality requirements for caged compounds listed above, additional specific features are important for caged Ca^{2+} compounds. The Ca^{2+} affinity before photolysis is ideally very high, such that the compound is fully saturated with Ca^{2+}, even at the low resting cytosolic Ca^{2+} concentration of around 100 nM prevailing in cardiomyocytes. Further, the Ca^{2+} affinity of the photolytic products should be very low, to allow rapid and complete release of the complexed Ca^{2+}. Specificity for Ca^{2+} (e.g. over Mg^{2+}) is another desirable attribute. Unfortunately, so far the compound perfectly meeting all these requirements does not yet exist, and the shortcomings of each compound need to be considered when designing the experimental protocol. For details, see below.

Example Studies with Caged Ca^{2+} Compounds

L-type Ca^{2+} Current

In cardiac muscle cells, a small Ca^{2+} influx via voltage-dependent L-type Ca^{2+} channels represents an initial step of EC-coupling, which is subsequently amplified several fold by release of Ca^{2+} from the sarcoplasmic reticulum (SR) via channels known as ryanodine receptors (RyRs). The amplification occurs by a mechanism referred to as Ca^{2+}-induced Ca^{2+} release (CICR) [12]. Since all these processes involving Ca^{2+} movements are tightly intertwined by their Ca^{2+} dependence, they are difficult to examine individually, despite some available pharmacological tools. To define the role of various parameters on either the L-type Ca^{2+} current itself or the activation and inactivation of the resulting CICR independently of one another, the use of caged Ca^{2+} compounds has repeatedly been instrumental and some examples are summarized below.

Besides carrying the flux of Ca^{2+} into the cytosol early during the action potential, the L-type Ca^{2+} channels are also inactivated (and facilitated) by elevations of cytosolic Ca^{2+} concentrations. During physiological activity of cardiomyocytes

Table 1 Selected commercially available caged compounds with applications in cardiac muscle research

Compound	**Kinetics (τ)**	**Absorption**	**Rate (s^{-1})**		**Quantum yield**		
NPE ATP	7 ms	260 nm	86		0.63		
DMNPE ATP	39 ms	355 nm	18		0.07		
NPE cAMP	165 ms	260 nm	4.2		0.39		
DMNB cAMP	4 ms	338 nm	200		–		
DEACM cAMP	ns	401 nm	–		0.25		
NPE IP_3	–	260 nm	250		0.65		
	K_d before	**K_d after**	**K_d ratio**	**K_d Mg^{2+}**	**Quantum yield**	**Rate (s^{-1})**	**2P-Cross-section (GM)**
DM-nitrophen	5 nM	3 mM	600,000	2.5 μM	0.18	38,000	0.01
NP EGTA	80 nM	1 mM	12,500	9 mM	0.23	68,000	0.001
nitr-5	145 nM	6.3 μM	54	8.5 mM	0.035	2500	0.01
Diazo-2	2.2 μM	73 nM	300	5.5 mM	0.03	2500	N.D.

For details see text

this occurs with every heart beat as a consequence of the substantial SR Ca^{2+} release into the nanodomain of the dyadic cleft, where RyRs and L-type Ca^{2+} channels colocalize. Based on evidence partly obtained from studies with genetically modified L-type Ca^{2+} channels, facilitation is considered to be a vital mechanism for the regulation of Ca^{2+} currents, while the inactivation of the L-type Ca^{2+} channels is thought to represent an important negative feed-back element to restrain the inflow of Ca^{2+} ions into the myocyte [13, 14]. Before these seminal structure-function studies clarified many molecular details of the L-type Ca^{2+} channel modulation by Ca^{2+}, photochemical approaches have paved the way to further dissect and analyze these mechanisms. Elevations of Ca^{2+} by photorelease from nitr-5 or DM-nitrophen were found to affect the Ca^{2+} current in a complex fashion. While the current was facilitated on longer time scales (over several seconds) [15], larger and short-lived Ca^{2+} concentration jumps generated by DM-nitrophen, but also by nitr-5, rapidly reduced the current amplitude, presumably via channel inactivation and without immobilizing the gating charge movement [16, 17]. These studies established the role of the Ca^{2+} concentration in both, current facilitation and inactivation.

Na^+-Ca^{2+} Exchange Current

A range of membrane currents is activated (or inhibited) by Ca^{2+}. In cardiac muscle the main current that can be recorded after photorelease of Ca^{2+} has been identified to be the Na^+-Ca^{2+} exchange current (I_{NCX}). After a Ca^{2+} concentration jump, one Ca^{2+} ion is extruded from the cell in exchange for three Na^+ ions, thereby generating an inward current [18]. In the physiological range of Ca^{2+} concentrations, the I_{NCX} shows a fairly linear dependence on the Ca^{2+} concentration, and can thus be used to estimate the amplitude and time-course of cellular Ca^{2+} signals [19, 20]. The rapid and highly synchronized initiation of molecular reaction steps of all NCX molecules in a given cardiomyocyte by flash-photolytic Ca^{2+} concentration jumps allowed the recording and characterization of pre-steady state kinetic currents. These electrogenic partial reaction steps of the NCX transport cycle could be resolved when the complete cycling of the transporter was prevented experimentally [21, 22].

Activation of CICR

A series of further studies has analyzed CICR itself using flash-photolytic Ca^{2+} release as a substitute trigger, frequently under experimental conditions where the physiological trigger, i.e. the L-type Ca^{2+} current, would be unacceptably variable or could not be activated at all (e.g. [23–26]).

As the mechanisms underlying EC-coupling were unraveled over a time span of many years, functional and structural similarities between skeletal and cardiac muscle have generally been very helpful. The structural similarities were stunning, from the subcellular to the molecular level of the EC-coupling machinery, often just making use of a different isoform of the same Ca^{2+} signaling proteins. Over time, each of the two related research fields has benefitted from the progress made in the other. While stimulating further research, in several instances, it has turned out to be more difficult to firmly establish functional differences between the two muscle types than to confirm similarities. One such example relates to the key mechanism of

EC-coupling, voltage-dependent activation of SR Ca^{2+} release (VACR) via allosteric coupling between the voltage sensors of the sarcolemma and the RyR1 in skeletal muscle [27], versus Ca^{2+}-induced activation of RyR2 in cardiac muscle (CICR). In some circumstances, experimental observations were made in cardiac muscle that could have been explained readily by the presence of some voltage-dependent features of cardiac SR Ca^{2+} release, such as the ability to terminate Ca^{2+} release prematurely by early repolarizations [28], or the observation of substantial SR Ca^{2+} release with almost all Ca^{2+} entry pathways blocked [29].

Based on these observations, the sarcolemmal membrane potential was suspected to have repercussions on the activation (or termination) of SR Ca^{2+} release in cardiac muscle, similar to skeletal muscle. To trigger CICR in cardiomyocytes independently of the membrane potential flash photolysis of DM-nitrophen seemed to be an ideal approach. This allowed to carry out such experiments at various, even extreme, membrane potentials. As it turned out, the resulting Ca^{2+} signals recorded as single cell mechanical activity were essentially independent of the membrane potential. This finding suggested that CICR was the main mechanism for cardiac muscle EC-coupling and that mechanisms other than the membrane voltage would be required to control (and terminate) SR Ca^{2+} release [25].

After the discovery of elementary Ca^{2+} signaling events, Ca^{2+} sparks, initially in cardiac [30] but later also in skeletal muscle [31, 32] (for review see, [33]), attempts were made to elicit these signals using flash-photolysis of caged Ca^{2+}. Even though in cardiac myocytes SR Ca^{2+} release could be elicited with such Ca^{2+} concentration jumps, the Ca^{2+} signals remained subcellularly homogeneous and were not composed of Ca^{2+} sparks [34, 35]. Later, Ca^{2+} release events smaller than typical Ca^{2+} sparks could be resolved with two-photon photolysis of caged Ca^{2+} and were termed "Ca^{2+} quarks" [36]. Ca^{2+} quarks are now thought to carry a significant fraction of the invisible SR Ca^{2+} leak in cardiac myocytes [37].

Termination of CICR

In the meantime we have learned a great deal about the activation of CICR in cardiac muscle. However, it has turned out to be more challenging to understand the mechanisms governing CICR termination. Originally, a hypothesis has been forwarded based on early experiments carried out in permeabilized single cardiac myocytes with a micro-injection system. In these ingenious experiments, rapid injections of trigger Ca^{2+} led to much larger Ca^{2+} release signals from the SR than slow injections, consistent with the presence of some form of Ca^{2+}-induced inactivation of Ca^{2+} release [12]. However, subsequent research using flash-photolytic Ca^{2+} release in intact myocytes found no evidence for the presence of Ca^{2+}-induced inactivation, at least in the experimentally accessible range of Ca^{2+} concentrations [24]. After the discovery of local control mechanisms and Ca^{2+} sparks as elementary signaling events underlying these local control mechanisms, alternative hypotheses for termination of Ca^{2+} release were proposed, such as stochastic attrition [38] and RyR desensitization by SR Ca^{2+} depletion [39], or possibly a cooperation of these two mechanisms, termed "pernicious attrition" or "induction decay" [40, 41].

To obtain further insight into the mechanism terminating Ca^{2+} release, flash photolytic techniques were applied and the recovery of CICR from refractoriness following Ca^{2+} release termination was examined. Using paired-pulse experiments, the recovery of SR Ca^{2+} release appeared to depend on the refilling of the SR via SERCA, but only in the case of whole-cell photolysis [20]. Such paired trigger pulses at short intervals of equal amplitude can only be generated with photolytic techniques, because the Ca^{2+} current itself displays a slow recovery from inactivation after the first current in a pair. Analogous to these whole-cell experiments, highly localized subcellular SR Ca^{2+} release events were elicited using two-photon excitation photolysis (see below for details of this technique). These local events recovered much faster than the whole-cell signals, presumably via rapid local SR refilling by diffusion of Ca^{2+} inside the SR network from neighboring and not depleted sites (Fig. 2) [19]. Together, these findings allowed the conclusion that the Ca^{2+} concentration inside the SR plays an important role in terminating SR Ca^{2+} release and in recovery from CICR refractoriness.

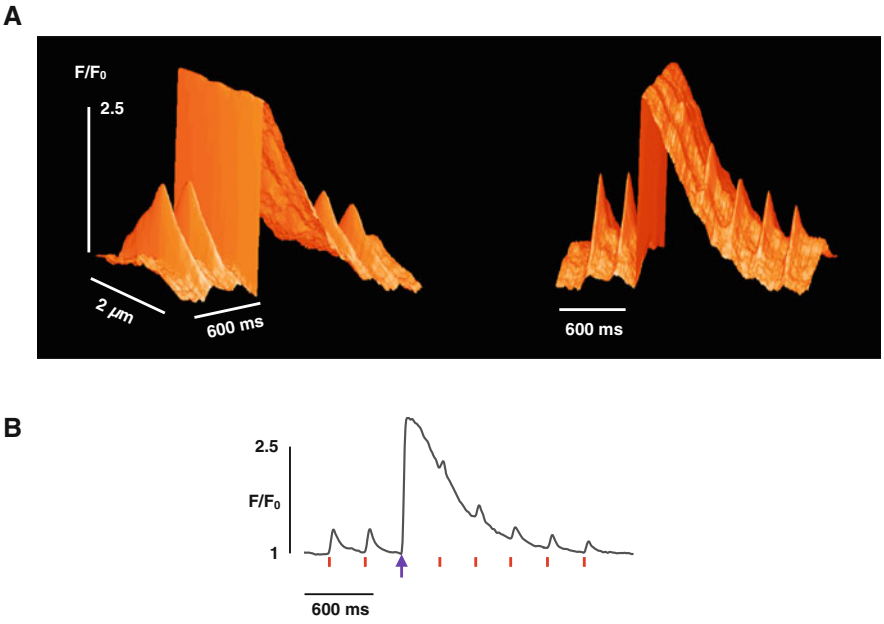

Fig. 2 Combined and simultaneous application of UV-flash and two-photon excitation photolysis of caged Ca^{2+} (DM-nitrophen) in a single cardiomyocyte. (**a**) Ca^{2+} concentration was recorded with Fluo-3 as confocal line-scan images and is shown as surface-plot representations (same recording seen from two different angles). Spatially limited Ca^{2+} transients with rapid decay (due to Ca^{2+} diffusion) represent two-photon signals. The larger concentration jump throughout the myocyte was elicited with a whole-cell UV flash. Its decay is governed by Ca^{2+} removal via the Na^{+}-Ca^{2+} exchanger and SERCA. (**b**) A trace extracted from the line-can image shows a train of two-photon photolytic stimulations (red lines), interspersed with a UV-flash (arrow)

An additional candidate mechanism for release termination was observed in experiments where single RyRs were reconstituted in artificial lipid bilayers and exposed to flash-photolytic Ca^{2+} concentration jumps [42, 43]. After an initial burst of high open probability, the channel activity gradually declined despite the continued presence of an elevated Ca^{2+} concentration, consistent with Ca^{2+}-induced inactivation of the RyRs. In stark contrast to classical Ca^{2+}-induced inactivation, these channels could be fully re-activated by a second Ca^{2+} concentration jump to an even more elevated level. This behavior was termed Ca^{2+}-induced "RyR adaptation".

Regulation and Pathology of CICR

During the last decade, several research laboratories examined the putative importance of RyR phosphorylation in the physiological regulation of cardiac Ca^{2+} signaling. Of interest was also the relevance of this post-translational RyR modification for both, precipitating arrhythmias and contributing to heart failure. In single cell experiments, changes of RyR phosphorylation were experimentally provoked by brief or long lasting stimulation of β-adrenergic receptors, mimicking the hormonal situation during physical exercise as well as emotional stress, or the chronic β-adrenergic receptor stimulation during heart failure. However, this maneuver leads to the experimentally challenging situation that a multitude of proteins involved in Ca^{2+} signaling change their phosphorylation status. Importantly, as a functional consequence of this the L-type Ca^{2+} current typically grows around threefold larger in amplitude, which by itself will lead to dramatic changes of the Ca^{2+} influx and the Ca^{2+} signals for triggering CICR, essentially masking any more subtle changes that might result from RyR phosphorylation. One approach to solve this dilemma has been to activate CICR using photorelease of Ca^{2+} as a means to generate a trigger that is invariant to β-AR stimulation [44, 45]. Using this approach, a small but significant increase of the Ca^{2+} transient was observed when the SR load was kept constant. Further spatio-temporal analysis of the triggered Ca^{2+} signals on a single-sarcomere level revealed that β-AR stimulation had improved the intersarcomeric synchronization of the release signals, thereby contributing to the somewhat larger amplitude. This enhanced synchronization could result from a rise in the Ca^{2+} sensitivity of the RyRs.

The comparison of CICR triggered by global (i.e. whole-cell) UV-flash illumination before and during β-AR stimulation with analogous signals triggered locally using two-photon photolysis of caged Ca^{2+} has allowed further conclusions about the underlying processes [44]. When triggering a series of Ca^{2+} signals in resting cardiomyocyte with UV-flashes, their amplitude slowly declined during β-AR stimulation, over a time window of approximately 5 min. This was later found to be caused by an SR Ca^{2+} depletion resulting from an increase in the number of spontaneous Ca^{2+} sparks, essentially representing a leak of Ca^{2+} out of the SR [45, 46]. However, the amplitude of the Ca^{2+} signals triggered by two-photon photolysis of caged Ca^{2+} paradoxically increased, despite the decline of SR Ca^{2+} content, suggesting either a change in the number of activated RyRs or a change of their gating properties during these events. Both possibilities would be consistent with functional changes of the RyRs resulting subsequent to their phosphorylation.

Muscle Contraction and Related Compounds

A substantial amount of research has been undertaken to correlate the biochemical reactions of the cross-bridge cycle and their kinetics with the mechanical function and biophysics of contracting muscle, both skeletal and cardiac. Since some of the reaction steps are very fast, flash-photolytic concentration jumps of the ATP concentration have been a valuable tool. Caged ATP and related nucleotide compounds are often available with a variety of photosensitive caging groups (e.g. NPE-ATP, DMNPE-ATP, see Table 1). The caging group mainly affects the absorbance, the position of the peak in the absorbance spectrum, the quantum yield and the kinetics of the ATP release following the flash. Most of these studies were carried out with skeletal muscle fibers, because they are much easier to handle for measurements of mechanical parameters than isolated single cardiomyocytes. But a few mechanical measurements were carried out using permeabilized cardiac muscle trabeculae.

ATP Hydrolysis, Activation of Tension and Rigor Force Decay

One series of these experiments investigated tension development after flash-photolytic liberation of ATP in the presence of Ca^{2+} and the kinetics of rigor tension decrease in the absence of Ca^{2+} in permeabilized cardiac muscle trabeculae [47, 48]. Steady-state ATP hydrolysis rates and the decrease of rigor tension in cardiac trabeculae were approximately 10 times slower than in fast-twitch skeletal muscle, but similar to slow-twitch muscle, suggesting similarities in the cross bridge cycle between slow twitch skeletal and cardiac muscle. These studies also provided quantitative information about ATP-induced rigor cross-bridge detachment rates. Interestingly, a small transient contraction before the tension decay was observed. This was caused by Mg^{2+}-ADP bound cross-bridges, which suppressed the normal thick filament inhibition of contraction and briefly allowed cross-bridge rebinding and force production early during relaxation from rigor.

While isolated cardiomyocytes have been used in numerous electrophysiological and Ca^{2+} signaling studies, their small size and delicate structure has made mechanical studies very challenging (but see [49]). Even though the readily observed contraction of isolated cardiomyocytes has been termed “unloaded shortening”, it is obvious that this contraction has to overcome internal restoring forces of the myocytes and their cytoskeletal proteins. Estimates of the internal forces have been obtained by following the relengthening of cardiomyocytes from rigor contractions, after rapid photorelease of ATP [50]. The results indicated that at sarcomere lengths longer than ~1.45 μm complete relengthening could be observed and most of the restoring forces were elastic in nature, with only a small contribution from viscous damping, depending on the velocity.

ATP-Sensitive K^+ Channels

In the experiments described above, rigor was induced by means of metabolic inhibition, by exposing the cells to NaCN and 2-deoxyglucose. This reduced the intracellular ATP concentration within a few minutes to a level where rigor bridges formed. Simultaneously, the ATP-sensitive K^+ channels became active. Photorelease of ATP to induce rigor decay inactivated these channels again. However, the rate of block was suspiciously slow, 100 times slower than the expected rate of ATP photorelease.

Investigating this oddity further, it was found that the caged ATP compound itself also blocked the ATP-sensitive channels, albeit with a lower efficiency than ATP itself. Thus, after an ATP concentration jump the caged ATP had to dissociate first from the channels, before ATP could bind and block more efficiently. Therefore, the rate of current block observed was limited by the dissociation of caged ATP from the channels rather than by the photoproduction of ATP (but see [51]).

Cardiac Regulatory Mechanisms and Related Compounds

There are several caged second messengers and regulators of cellular function available that have been used to examine the biology of cardiac myocytes. Most notably caged variants of cAMP and $InsP_3$ (see Table 1), some of which are also accessible as cell membrane permeable compounds (e.g. $InsP_3$ as PM esters).

Caged cAMP

The second messenger cAMP is involved in the activation of signaling pathways linking β-adrenergic receptor stimulation to the activation of PKA (and EPAC). Caged versions of this second messenger were instrumental in characterizing the kinetics of post-receptor events in cardiomyocytes [52]. L-type currents were recorded as read-outs of PKA activation. A lag phase of ~3 s, usually observed after β-adrenergic receptor stimulation, was absent after flash photolytic liberation of cAMP, suggesting the activation of adenylate cyclase and synthesis of cAMP were rate limiting steps and responsible for the lag. Using the same approach, analogous observations were made while recording Cl^- currents in cardiomyocytes [53].

The existence of subcellular concentration gradients for cAMP has been known for quite some time (see [54] for review). Using a combination of direct cAMP imaging with a FRET based probe and flash-photolytic liberation of cAMP it was possible to quantify spatiotemporal features of cAMP diffusion and PKA activation [55].

Caged $InsP_3$

The role of the second messenger $InsP_3$ and the $InsP_3$ receptor Ca^{2+} release channels ($InsP_3Rs$) in cardiac myocytes is not yet entirely clear, both in ventricular myocytes and in atrial myocytes, where the $InsP_3Rs$ are more abundant. $InsP_3$ and $InsP_3Rs$ have been implicated in various cardiac pathologies, including hypertrophy, heart failure and atrial fibrillation [56, 57] and in excitation-transcription coupling [58]. In addition, a participation in or at least modulation of CICR and RyRs by Ca^{2+} released via $InsP_3Rs$ has been suggested. This notion was also based on small contractions that could be elicited by photorelease of $InsP_3$ in permeabilized trabeculae [23] and on the observation of Ca^{2+} signals in cultured neonatal cardiomyocytes [59]. In a recent confocal imaging study, flash-photolytic liberation of $InsP_3$ in isolated mouse atrial myocytes was found to induce noticeable Ca^{2+} efflux from the SR, which was able to trigger Ca^{2+} sparks, but was itself "eventless" in nature [60]. In atrial myocytes from a rabbit heart failure (HF) animal model

$InsP_3R$ overexpression was found to boost CICR at low cytosolic $InsP_3$ concentrations. However, upon photolytic release of $InsP_3$ in HF cells the resting cytosolic Ca^{2+} concentration gradually increased while the amplitude of the Ca^{2+} transients declined, suggesting the activation of a substantial SR Ca^{2+} leak via the overexpressed $InsP_3Rs$ by high concentrations of $InsP_3$ [61]. Together, these studies using caged $InsP_3$ compounds demonstrate that photolytic $InsP_3$ concentration jumps are a powerful tool to obtain further insight into the role of $InsP_3Rs$ in cardiac muscle Ca^{2+} signaling, both in health and disease.

Various Caged Compounds

Other caged compounds with potential use for cardiac research have been occasionally reported. These compounds are often not available commercially, but may be accessible in the framework of scientific collaborations. For example the caged SERCA inhibitor Nmoc-DBHQ has been used to analyze mechanisms of Ca^{2+} wave propagation in cardiomyocytes [62]. Localized photolysis of caged caffeine has been applied to initiate local Ca^{2+} release signals from the SR [63]. A caged mitochondrial uncoupler (AG10) has also been developed [64], as well as caged cyclic cADP-ribose, a putative RyR modulator [65].

General Considerations for the Use of Caged Compounds

Light Sources and Illumination

Presently available caged compounds require illumination by UV or near UV light (200–360 nm) to initiate photolysis (but see paragraph on new developments below). For compounds with very fast reaction kinetics (faster than milliseconds), it is advantageous to use a pulsed illumination (flashes lasting nanoseconds to milliseconds) to make full use of the kinetic features of such compounds, particularly when used to probe biological processes that are also happening on a fast time scale. For more slowly evolving phenomena, shuttered illuminations can also be feasible (milliseconds to seconds). The light sources can be coupled to the fluorescent port of almost any microscope in an epi-illumination arrangement. Coupling is frequently implemented by using liquid filled light-guides or fused silica optical fibers. Alternatively, a direct illumination of the preparation with a focusing lens system or proximity focusing are possible.

Flash Lamps

Xenon flash lamps are frequently used as a relatively inexpensive technique to generate short pulses of intense UV light [66] and several systems are commercially available. Compared to pulsed lasers, high-power UV flash-lamps usually have limited repetition rates and somewhat longer flash durations (~1 ms). Several systems can overcome the limitation of a low repetition rate by integrating two flash lamps units into one system. The two lamps can then be fired at any desirable interval, to create paired-pulse stimulation protocols, for example to document the time-course of a signal recovering subsequent to its inactivation.

Pulsed Lasers

In the early days of laser-flash photolysis frequency-doubled ruby lasers were often employed (e.g. [67]). They have a wavelength of 347 nm and a pulse duration of around 50 ns in their Q-switched version. More recently, frequency-tripled Nd:YAG lasers have become the photolytic light sources of choice because of their easy availability and high efficiency. They generate UV flashes at 355 nm wavelength and can have high repetition rates even in high-power versions (up to 200 Hz). The short duration of their pulses (~10 ns) can be a disadvantage, because the peak power is extremely high and the generated dense electromagnetic field can lead to cell membrane break-down and cell damage.

A variety of pulsed nitrogen lasers are commercially available, but are also fairly easy to build as a low-cost solution [68]. They have a wavelength of 337 nm and a pulse duration of a few nanoseconds. The comparatively short wavelength may need special microscope objectives when using epi-illumination, since many types of glass used in microscope objectives absorb substantially at wavelengths below 340 nm.

Diode Lasers and Light Emitting Diodes (LED)

With the advent of a wide spectrum of solid-state lasers, the availability of gated or shuttered UV-diode lasers has become more widespread [69]. They are available at several UV and blue wavelengths, from 261 to 405 nm and longer. It is even possible to use UV-LEDs (e.g. 365 nm) for photolysis [70]. With most of these approaches the pulse duration for photolysis is typically longer than with high-energy pulsed UV-lasers (illumination of several milliseconds). An example is shown in Fig. 3, where $InsP_3$ was photoreleased in He-La cells with a pulse from a 405 nm blue laser.

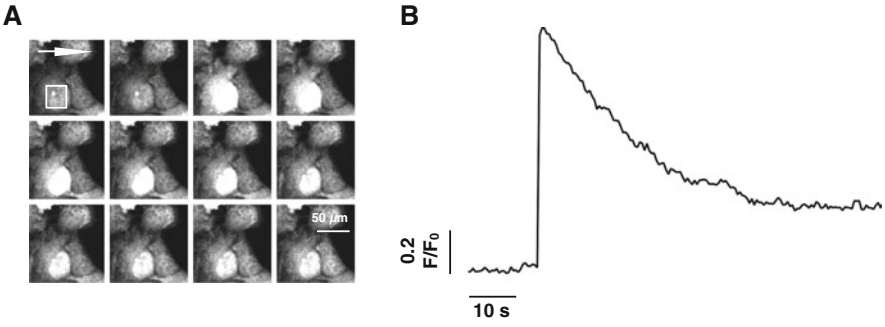

Fig. 3 Uncaging using a low-power 405 nm solid-state laser. For slower biological signals, a CW solid-state laser can be a convenient tool, also because it is pre-installed on many confocal microscopes. But this low-power light source requires photolytic illumination times of several tens to hundreds of milliseconds. (**a**) Confocal image sequence of signals recorded from confluent HeLa cells loaded with the PM ester form of caged $InsP_3$. After the second frame light from a 405 nm laser was applied as a spiral shaped scan for 200 ms. Subsequently, the photoreleased $InsP_3$ activated Ca^{2+} release from the endoplasmic reticulum. (**b**) Ca^{2+} signal trace extracted from the region of interest marked with a white square in the first frame of panel (**a**)

Localized and Two-Photon Excitation

With the recognition of the relevance of subcellular micro- and nanodomains for signaling it became desirable to carry out photolysis in a highly localized fashion. To reach this goal, several techniques have been utilized to confine, focus and steer the UV illumination as tiny spots or complex illumination patterns, often with the help of fiber-optic light-guides [71, 72] or arrays of tiltable micro-mirrors [73].

Two-photon excitation is yet another tool which allows highly localized excitation of caged compounds, with good resolution also in the vertical *z*-direction. Unlike local excitation with UV-light, photorelease only occurs in the focal plane of the ultrafast laser, because only there the photon flux is sufficiently high to reach an adequate probability for the chromophore to absorb two photons within a few femtoseconds and to become excited. Thus, to allow two-photon excitation with a reasonable efficiency, the laser pulses need to be in the range of 100 fs to 1 ps and ultrafast lasers are required. The most frequently applied laser systems for two-photon confocal microscopy and photolysis are mode-locked Ti:sapphire lasers. They generate the required ultrashort pulses at a frequency of around 80 MHz. The wavelength is tunable from 690 to 1050 nm, corresponding to 345–525 nm for single photon excitation. While these lasers can essentially create diffraction-limited point-sources of photoreleased substances, it turned out that countless presently available caged compounds exhibit a very small two-photon absorbance cross-section, rendering them very inefficient for two-photon photolysis (but see paragraph on "New Developments").

Loading of the Cells with Caged Compounds

Patch Pipette

The loading of caged compounds into cells is virtually identical to the procedures used for loading of fluorescent indicators. Most compounds are not membrane permeable and are therefore introduced into the cytosolic space by injection or dialysis via a patch-clamp pipette, together with a defined electrode filling solution which mimics the intracellular environment. In the case of caged Ca^{2+} compounds, the free concentration of Ca^{2+} before photolysis needs to be calculated to avoid overloading of the cells with Ca^{2+}. For all caged compounds, a concentration has to be determined which, upon photolysis of a certain set-up specific fraction, will result in the desired final concentration of the biologically active product. Besides properties of the caged compound itself (e.g. absorbance, extinction coefficient, quantum yield), the performance of the entire flash-photolysis setup needs to be considered (e.g. light source, light losses along the optical path, flash duration, available light intensity on the cell).

Cell Permeant Caged Compounds

For a few selected caged Ca^{2+} and other compounds, membrane permeant ester forms are available (e.g. NP-EGTA, nitr-5, $InsP_3$). These compounds will enter the

myocytes and cellular esterases will subsequently produce the caged Ca^{2+} compound, which will remain trapped inside the cell. With this approach, the experimenter can load multiple cells simultaneously but has no direct control over the extent of loading and the composition of the intracellular milieu. To complex the caged compound with Ca^{2+} once it has entered the cells, sufficient Ca^{2+} influx needs to be activated across the cell membrane. In the case of cardiac myocytes, this can be easily achieved, for example by eliciting action potentials by field stimulation. In addition, the AM-ester loading technique is problematic with DM-nitrophen because of its high affinity for Mg^{2+}. While in a pipette solution the Mg^{2+} concentration can be lowered when dialyzing DM-nitrophen, this is not possible with AM-ester loading. As a consequence of this, a significant fraction of DM-nitrophen, once formed by the cell, will have Mg^{2+} bound, converting it mostly into a caged Mg^{2+} compound [74].

Limitations of the Technique and the Compounds

Stability and Shelf Life

Obviously, all caged compounds are very light sensitive and need to be protected from light during storage and handling. The chemical stability of the various compounds is known to differ vastly. Some are very stable, while some undergo quite rapid break-down, particularly when in solution (e.g. by hydrolysis). Frozen storage is therefore generally recommended.

Formation of Phototoxic By-Products

Upon photolysis of caged compounds, not only the desired biologically active substance is liberated, but also phototoxic by-products [75], such as reactive nitroso-ketones and aldehydes, which can have unwanted side effects, either by affecting the mechanism under investigation, or attacking other cellular targets. These by-products can also contaminate the caged compounds before photolysis is performed, for example after extended storage. Nitroso-ketones have been reported to inhibit ATPases, such as the Na^+-K^+-ATPase [76] and the acto-myosin ATPase [77], and to block membrane channels, such as the ATP-sensitive K^+-channels [78]. By including scavenging thiol compounds into the patch-pipette solution, like dithiothreitol (DTT) or reduced glutathione (GSH), the side effects of by-products can generally be reduced.

The caged compounds and their photoproducts may also interact chemically with any fluorescent indicators that are used simultaneously. Such interactions could alter the recorded signals [5]. For any new combination of dyes and caged compounds the necessary control experiments therefore need to be carried out to either exclude such interactions, or to correct the recorded signals for them [79].

Absorbance and Quantum Yield

Besides the kinetics of the photolysis, the extinction coefficient and quantum yield are important determinants for the efficiency of a given caged compound and have

practical implications in their everyday use. Since these compounds are often used in quite high concentrations (~millimolar), the fraction of light absorbed by the dye in the cytosol can be significant, particularly in large cells, such as cardiomyocytes [5]. This may lead to a gradient in the portion of photolyzed compound across the cell, such that the surface facing the light-source experiences a much larger concentration jump than the membrane on the far side of the cell, leading to heterogeneous biological signals. The problem of spatial gradients is less pronounced in the case of two-photon excitation with pulsed infra-red light, which is not absorbed by the caged compound. However, as mentioned before, the two-photon absorbance cross section, measured in units of Goeppert-Mayer (1 GM = 10^{-50} cm^4 s $photon^{-1}$), has been disappointingly low for many available compounds, making the application of this technique quite challenging (but see section "New Developments" below).

New Developments: Outlook

Enhanced Caging Groups and Probes Optimized for Two-Photon Photolysis

Substantial progress has been made in the design and synthesis of caged compounds in recent years. One area of development concerns the improvement of the optical and chemical properties of the compounds and their chromophore towards more efficient photolysis and higher light sensitivity. Examples are caging groups based on coumarin, such as DEACM [80], on nitrobenzodifuran (NDBF) [81], nitroveratryl [82, 83] or bisstyrylthiophene (BIST) [84]. Such developments turned out to be particularly relevant for caged compounds to be used in combination with two-photon excitation photolysis. As far as commercially available compounds are concerned, it was realized that the DMNPE caging group absorbs two-photon excitation reasonably well (e.g. DM-nitrophen with 0.01 GM), while the NP two-photon absorbance was so small that it could not be reliably determined, for example with NP-EGTA [85]. Because of this problem caged compounds like NP-EGTA and NPE-$InsP_3$ could not be readily used with two-photon excitation.

New Spectral Windows for Multicolor Excitation Photolysis

Traditional caging groups have the peak of the absorbance spectrum in the UV range of wavelengths (e.g. NPE ~260 nm), with DMNPE being shifted towards longer wavelengths (~360 nm). More recently, caged compounds with much longer wavelengths have been engineered, up to around 400–450 nm [80, 84, 86]. These compounds also offer excellent two-photon absorption (e.g. 350 GM for BIST-2EGTA). A toolbox of caging groups absorbing at sufficiently separate wavelengths opens the intriguing possibility to photorelease two (or more) different biologically active molecules using different wavelengths of light. The technique has been called "two-color uncaging", but so far has not yet been applied in cardiac muscle research [87].

Optogenetics

Caged compounds can be regarded as optical actuators. As such, they have been considered to be a parent technology for optogenetics and optopharmacology, both of which apply the same basic experimental paradigm and are being applied to cardiac research (see [88] for review). These modern but complex technologies combine many of the advantages of caged compounds (e.g. spatio-temporal control by light) with advantages borrowed from molecular biology approaches (e.g. targeting of the optical actuator to specific cells or subcellular domains). In the future, the two fields may inspire each other and lead to more wide-spread use of the classical photolysis techniques, partly because the basic biophysical instrumentation for the two techniques is almost identical. In other words, more and more laboratories using optogenetics approaches will become well equipped and ready to photolyze caged compounds and thus consider this approach as an easily accessible experimental technique. This is particularly true for novel caged compounds that can be photolyzed in the visible range of wavelengths [84] with lasers that are already available in most optogenetics laboratories.

Acknowledgements This work was supported by the Swiss National Science Foundation (31-132689 and 31-156375 to E.N.), by the National Institutes of Health (NIH; R01AR053933 and R01HL093342 to N.S), by the Swiss Foundation for Research on Muscle diseases and by the Microscopy Imaging Center (MIC) of the University of Bern (to E.N. and N.S.).

References

1. Severs NJ. The cardiac muscle cell. Bioessays. 2000;22:188–99. https://doi.org/10.1002/(SICI)1521-1878(200002)22:2<188::AID-BIES10>3.0.CO;2-T.
2. Ellis-Davies GCR. Caged compounds: photorelease technology for control of cellular chemistry and physiology. Nat Methods. 2007;4:619–28. https://doi.org/10.1038/nmeth1072.
3. McCray JA, Trentham DR. Properties and uses of photoreactive caged compounds. Annu Rev Biophys Biophys Chem. 1989;18:239–70. https://doi.org/10.1146/annurev.bb.18.060189.001323.
4. Escobar AL, Velez P, Kim AM, et al. Kinetic properties of DM-nitrophen and calcium indicators: rapid transient response to flash photolysis. Pflugers Arch. 1997;434:615–31. https://doi.org/10.1007/s004240050444.
5. Zucker RS. Effects of photolabile calcium chelators on fluorescent calcium indicators. Cell Calcium. 1992;13:29–40.
6. Brieke C, Rohrbach F, Gottschalk A, et al. Light-controlled tools. Angew Chem Int Ed Engl. 2012;51:8446–76. https://doi.org/10.1002/anie.201202134.
7. Kaplan JH, Ellis-Davies GCR. Photolabile chelators for the rapid photorelease of divalent cations. Proc Natl Acad Sci U S A. 1988;85:6571–5.
8. Ellis-Davies GCR, Kaplan JH. Nitrophenyl-EGTA, a photolabile chelator that selectively binds Ca^{2+} with high affinity and releases it rapidly upon photolysis. Proc Natl Acad Sci U S A. 1994;91:187–91.
9. Adams SR, Kao JPY, Grynkiewicz G, et al. Biologically useful chelators that release Ca^{2+} upon illumination. J Am Chem Soc. 1988;110:3212–20. https://doi.org/10.1021/ja00218a034.
10. Adams SR, Kao JPY, Tsien RY. Biologically useful chelators that take up Ca^{2+} upon illumination. J Am Chem Soc. 1989;111:7957–68. https://doi.org/10.1021/ja00202a042.

11. Lipp P, Lüscher C, Niggli E. Photolysis of caged compounds characterized by ratiometric confocal microscopy: a new approach to homogeneously control and measure the calcium concentration in cardiac myocytes. Cell Calcium. 1996;19:255–66.
12. Fabiato A. Time and calcium dependence of activation and inactivation of calcium-induced release of calcium from the sarcoplasmic reticulum of a skinned canine cardiac Purkinje cell. J Gen Physiol. 1985;85:247–89.
13. Peterson BZ, DeMaria CD, Adelman JP, Yue DT. Calmodulin is the Ca^{2+} sensor for Ca^{2+} -dependent inactivation of L-type calcium channels. Neuron. 1999;22:549–58.
14. Zühlke RD, Pitt GS, Deisseroth K, et al. Calmodulin supports both inactivation and facilitation of L-type calcium channels. Nature. 1999;399:159–62. https://doi.org/10.1038/20200.
15. Gurney AM, Charnet P, Pye JM, Nargeot J. Augmentation of cardiac calcium current by flash photolysis of intracellular caged-Ca^{2+} molecules. Nature. 1989;341:65–8. https://doi.org/10.1038/341065a0.
16. Bates SE, Gurney AM. Ca^{2+}-dependent block and potentiation of L-type calcium current in guinea-pig ventricular myocytes. J Physiol. 1993;466:345–65.
17. Hadley RW, Lederer WJ. Ca^{2+} and voltage inactivate Ca^{2+} channels in guinea-pig ventricular myocytes through independent mechanisms. J Physiol. 1991;444:257–68.
18. Niggli E, Lederer WJ. Activation of Na-Ca exchange current by photolysis of caged calcium. Biophys J. 1993;65:882–91. https://doi.org/10.1016/S0006-3495(93)81105-6.
19. DelPrincipe F, Egger M, Niggli E. Calcium signalling in cardiac muscle: refractoriness revealed by coherent activation. Nat Cell Biol. 1999;1:323–9. https://doi.org/10.1038/14013.
20. Szentesi P, Pignier C, Egger M, et al. Sarcoplasmic reticulum Ca^{2+} refilling controls recovery from Ca^{2+}-induced Ca^{2+} release refractoriness in heart muscle. Circ Res. 2004;95:807–13. https://doi.org/10.1161/01.RES.0000146029.80463.7d.
21. Kappl M, Nagel G, Hartung K. Voltage and Ca^{2+} dependence of pre-steady-state currents of the Na-Ca exchanger generated by Ca^{2+} concentration jumps. Biophys J. 2001;81:2628–38. https://doi.org/10.1016/S0006-3495(01)75906-1.
22. Niggli E, Lederer WJ. Molecular operations of the sodium-calcium exchanger revealed by conformation currents. Nature. 1991a;349:621–4. https://doi.org/10.1038/349621a0.
23. Kentish JC, Barsotti RJ, Lea TJ, et al. Calcium release from cardiac sarcoplasmic reticulum induced by photorelease of calcium or Ins(1,4,5)P_3. Am J Physiol. 1990;258:H610–5.
24. Näbauer M, Morad M. Ca^{2+}-induced Ca^{2+} release as examined by photolysis of caged Ca^{2+} in single ventricular myocytes. Am J Physiol. 1990;258:C189–93.
25. Niggli E, Lederer WJ. Voltage-independent calcium release in heart muscle. Science. 1990;250:565–8.
26. Valdeolmillos M, O'Neill SC, Smith GL, Eisner DA. Calcium-induced calcium release activates contraction in intact cardiac cells. Pflugers Arch. 1989;413:676–8.
27. Shirokova N, Rios E. Small event Ca^{2+} release: a probable precursor of Ca^{2+} sparks in frog skeletal muscle. J Physiol. 1997;502:3–11.
28. Cannell MB, Berlin JR, Lederer WJ. Effect of membrane potential changes on the calcium transient in single rat cardiac muscle cells. Science. 1987;238:1419–23.
29. Hobai IA, Howarth FC, Pabbathi VK, et al. "Voltage-activated Ca release" in rabbit, rat and guinea-pig cardiac myocytes, and modulation by internal cAMP. Pflugers Arch. 1997;435:164–73.
30. Cheng H, Lederer WJ, Cannell MB. Calcium sparks: elementary events underlying excitation-contraction coupling in heart muscle. Science. 1993;262:740–4.
31. Klein MG, Cheng H, Santana LF, et al. Two mechanisms of quantized calcium release in skeletal muscle. Nature. 1996;379:455–8. https://doi.org/10.1038/379455a0.
32. Shirokova N, García J, Rios E. Local calcium release in mammalian skeletal muscle. J Physiol (Lond). 1998;512:377–84.
33. Niggli E, Shirokova N. A guide to sparkology: the taxonomy of elementary cellular Ca^{2+} signaling events. Cell Calcium. 2007;42:379–87. https://doi.org/10.1016/j.ceca.2007.02.010.

34. Lipp P, Niggli E. Submicroscopic calcium signals as fundamental events of excitation--contraction coupling in guinea-pig cardiac myocytes. J Physiol (Lond). 1996;492:31–8.
35. Shirokova N, Niggli E. Studies of RyR function in situ. Methods. 2008;46:183–93. https://doi.org/10.1016/j.ymeth.2008.09.017.
36. Lipp P, Niggli E. Fundamental calcium release events revealed by two-photon excitation photolysis of caged calcium in Guinea-pig cardiac myocytes. J Physiol (Lond). 1998;508:801–9.
37. Brochet DXP, Xie W, Yang D, et al. Quarky calcium release in the heart. Circ Res. 2011;108:210–8. https://doi.org/10.1161/CIRCRESAHA.110.231258.
38. Stern MD. Theory of excitation-contraction coupling in cardiac muscle. Biophys J. 1992;63:497–517. https://doi.org/10.1016/S0006-3495(92)81615-6.
39. Terentyev D, Viatchenko-Karpinski S, Valdivia HH, et al. Luminal Ca^{2+} controls termination and refractory behavior of Ca^{2+}-induced Ca^{2+} release in cardiac myocytes. Circ Res. 2002;91:414–20.
40. Gillespie D, Fill M. Pernicious attrition and inter-RyR2 CICR current control in cardiac muscle. J Mol Cell Cardiol. 2013;58:53–8. https://doi.org/10.1016/j.yjmcc.2013.01.011.
41. Laver DR, Kong CHT, Imtiaz MS, Cannell MB. Termination of calcium-induced calcium release by induction decay: an emergent property of stochastic channel gating and molecular scale architecture. J Mol Cell Cardiol. 2013;54:98–100. https://doi.org/10.1016/j.yjmcc.2012.10.009.
42. Györke S, Fill M. Ryanodine receptor adaptation: control mechanism of Ca^{2+}-induced Ca^{2+} release in heart. Science. 1993;260:807–9.
43. Valdivia HH, Kaplan JH, Ellis-Davies GCR, Lederer WJ. Rapid adaptation of cardiac ryanodine receptors: modulation by Mg^{2+} and phosphorylation. Science. 1995;267:1997–2000.
44. Lindegger N, Niggli E. Paradoxical SR Ca^{2+} release in guinea-pig cardiac myocytes after beta-adrenergic stimulation revealed by two-photon photolysis of caged Ca^{2+}. J Physiol (Lond). 2005;565:801–13. https://doi.org/10.1113/jphysiol.2005.084376.
45. Ogrodnik J, Niggli E. Increased Ca^{2+} leak and spatiotemporal coherence of Ca^{2+} release in cardiomyocytes during beta-adrenergic stimulation. J Physiol (Lond). 2010;588:225–42. https://doi.org/10.1113/jphysiol.2009.181800.
46. Gutierrez DA, Fernandez-Tenorio M, Ogrodnik J, Niggli E. NO-dependent CaMKII activation during β-adrenergic stimulation of cardiac muscle. Cardiovasc Res. 2013;100:392–401. https://doi.org/10.1093/cvr/cvt201.
47. Barsotti RJ, Ferenczi MA. Kinetics of ATP hydrolysis and tension production in skinned cardiac muscle of the guinea pig. J Biol Chem. 1988;263:16750–6.
48. Martin H, Barsotti RJ. Relaxation from rigor of skinned trabeculae of the guinea pig induced by laser photolysis of caged ATP. Biophys J. 1994;66:1115–28. https://doi.org/10.1016/S0006-3495(94)80892-6.
49. Iribe G, Ward CW, Camelliti P, et al. Axial stretch of rat single ventricular cardiomyocytes causes an acute and transient increase in Ca^{2+} spark rate. Circ Res. 2009;104:787–95. https://doi.org/10.1161/CIRCRESAHA.108.193334.
50. Niggli E, Lederer WJ. Restoring forces in cardiac myocytes. Insight from relaxations induced by photolysis of caged ATP. Biophys J. 1991b;59:1123–35. https://doi.org/10.1016/S0006-3495(91)82327-X.
51. Il'ichev YV, Schwörer MA, Wirz J. Photochemical reaction mechanisms of 2-nitrobenzyl compounds: methyl ethers and caged ATP. J Am Chem Soc. 2004;126:4581–95. https://doi.org/10.1021/ja039071z.
52. Frace AM, Méry PF, Fischmeister R, Hartzell HC. Rate-limiting steps in the beta-adrenergic stimulation of cardiac calcium current. J Gen Physiol. 1993;101:337–53.
53. Nakashima Y, Ono K. Rate-limiting steps in activation of cardiac Cl^- current revealed by photolytic application of cAMP. Am J Physiol. 1994;267:H1514–22.

54. Fischmeister R, Castro LRV, Abi-Gerges A, et al. Compartmentation of cyclic nucleotide signaling in the heart: the role of cyclic nucleotide phosphodiesterases. Circ Res. 2006;99:816–28. https://doi.org/10.1161/01.RES.0000246118.98832.04.
55. Saucerman JJ, Zhang J, Martin JC, et al. Systems analysis of PKA-mediated phosphorylation gradients in live cardiac myocytes. Proc Natl Acad Sci U S A. 2006;103:12923–8. https://doi.org/10.1073/pnas.0600137103.
56. Nakayama H, Bodi I, Maillet M, et al. The IP_3 receptor regulates cardiac hypertrophy in response to select stimuli. Circ Res. 2010;107:659–66. https://doi.org/10.1161/CIRCRESAHA.110.220038.
57. Yamada J, Ohkusa T, Nao T, et al. Up-regulation of inositol 1,4,5 trisphosphate receptor expression in atrial tissue in patients with chronic atrial fibrillation. J Am Coll Cardiol. 2001;37:1111–9. https://doi.org/10.1016/S0735-1097(01)01144-5.
58. Wu X, Zhang T, Bossuyt J, et al. Local $InsP_3$-dependent perinuclear Ca^{2+} signaling in cardiac myocyte excitation-transcription coupling. J Clin Invest. 2006;116:675–82. https://doi.org/10.1172/JCI27374.
59. Jaconi M, Bony C, Richards SM, et al. Inositol 1,4,5-trisphosphate directs Ca^{2+} flow between mitochondria and the endoplasmic/sarcoplasmic reticulum: a role in regulating cardiac autonomic Ca^{2+} spiking. Mol Biol Cell. 2000;11:1845–58.
60. Horn T, Ullrich ND, Egger M. "Eventless" $InsP_3$-dependent SR-Ca^{2+} release affecting atrial Ca^{2+} sparks. J Physiol (Lond). 2013;591:2103–11. https://doi.org/10.1113/jphysiol.2012.247288.
61. Hohendanner F, Walther S, Maxwell JT, et al. Inositol-1,4,5-trisphosphate induced Ca^{2+} release and excitation-contraction coupling in atrial myocytes from normal and failing hearts. J Physiol (Lond). 2015;593:1459–77. https://doi.org/10.1113/jphysiol.2014.283226.
62. Keller M, Kao JPY, Egger M, Niggli E. Calcium waves driven by "sensitization" wave-fronts. Cardiovasc Res. 2007;74:39–45. https://doi.org/10.1016/j.cardiores.2007.02.006.
63. Ni J, Auston DA, Freilich DA, et al. Photochemical gating of intracellular Ca^{2+} release channels. J Am Chem Soc. 2007;129:5316–7. https://doi.org/10.1021/ja069361q.
64. Avlonitis N, Chalmers S, McDougall C, et al. Caged AG10: new tools for spatially predefined mitochondrial uncoupling. Mol Biosyst. 2009;5:450–7. https://doi.org/10.1039/b820415m.
65. Guo X, Laflamme MA, Becker PL. Cyclic ADP-ribose does not regulate sarcoplasmic reticulum Ca^{2+} release in intact cardiac myocytes. Circ Res. 1996;79:147–51.
66. Rapp G, Güth K. A low cost high intensity flash device for photolysis experiments. Pflugers Arch. 1988;411:200–3.
67. Walker JW, Somlyo AV, Goldman YE, et al. Kinetics of smooth and skeletal muscle activation by laser pulse photolysis of caged inositol 1,4,5-trisphosphate. Nature. 1987;327:249–52. https://doi.org/10.1038/327249a0.
68. Engert F, Paulus GG, Bonhoeffer T. A low-cost UV laser for flash photolysis of caged compounds. J Neurosci Methods. 1996;66:47–54. https://doi.org/10.1016/0165-0270(95)00157-3.
69. Trigo FF, Corrie JET, Ogden D. Laser photolysis of caged compounds at 405 nm: photochemical advantages, localisation, phototoxicity and methods for calibration. J Neurosci Methods. 2009;180:9–21. https://doi.org/10.1016/j.jneumeth.2009.01.032.
70. Bernardinelli Y, Haeberli C, Chatton J-Y. Flash photolysis using a light emitting diode: an efficient, compact, and affordable solution. Cell Calcium. 2005;37:565–72. https://doi.org/10.1016/j.ceca.2005.03.001.
71. Sobie EA, Kao JPY, Lederer WJ. Novel approach to real-time flash photolysis and confocal [Ca^{2+}] imaging. Pflugers Arch. 2007;454:663–73. https://doi.org/10.1007/s00424-007-0229-z.
72. Wang SS, Augustine GJ. Confocal imaging and local photolysis of caged compounds: dual probes of synaptic function. Neuron. 1995;15:755–60.
73. Shkryl VM, Maxwell JT, Blatter LA. A novel method for spatially complex diffraction-limited photoactivation and photobleaching in living cells. J Physiol. 2012;590:1093–100. https://doi.org/10.1113/jphysiol.2011.223446.

74. Ellis-Davies GCR. DM-nitrophen AM is caged magnesium. Cell Calcium. 2006;39:471–3. https://doi.org/10.1016/j.ceca.2006.02.002.
75. Pelliccioli AP, Wirz J. Photoremovable protecting groups: reaction mechanisms and applications. Photochem Photobiol Sci. 2002;1:441–58. https://doi.org/10.1039/b200777k.
76. Kaplan JH, Forbush B, Hoffman JF. Rapid photolytic release of adenosine 5′-triphosphate from a protected analogue: utilization by the Na:K pump of human red blood cell ghosts. Biochemistry. 1978;17:1929–35.
77. Goldman YE, Hibberd MG, Trentham DR. Relaxation of rabbit psoas muscle fibres from rigor by photochemical generation of adenosine-5′-triphosphate. J Physiol (Lond). 1984;354:577–604.
78. Nichols CG, Niggli E, Lederer WJ. Modulation of ATP-sensitive potassium channel activity by flash-photolysis of "caged-ATP" in rat heart cells. Pflugers Arch. 1990;415:510–2.
79. Hadley RW, Kirby MS, Lederer WJ, Kao JPY. Does the use of DM-nitrophen, nitr-5, or diazo-2 interfere with the measurement of indo-1 fluorescence? Biophys J. 1993;65:2537–46. https://doi.org/10.1016/S0006-3495(93)81328-6.
80. Hagen V, Bendig J, Frings S, Eckardt T. Highly efficient and ultrafast phototriggers for cAMP and cGMP by using long-wavelength UV/VIS-activation. Angew Chem Int Ed Engl. 2001;40(6):1045. https://doi.org/10.1002/1521-3773(20010316)40:6<1045::AID-ANIE10450>3.0.CO;2-F.
81. Momotake A, Lindegger N, Niggli E, et al. The nitrodibenzofuran chromophore: a new caging group for ultra-efficient photolysis in living cells. Nat Methods. 2006;3:35–40. https://doi.org/10.1038/nmeth821.
82. Kantevari S, Hoang CJ, Ogrodnik J, et al. Synthesis and two-photon photolysis of 6-(ortho-nitroveratryl)-caged IP_3 in living cells. ChemBioChem. 2006;7:174–80. https://doi.org/10.1002/cbic.200500345.
83. Russell AG, Ragoussi M-E, Ramalho R, et al. Alpha-carboxy-6-nitroveratryl: a photolabile protecting group for carboxylic acids. J Org Chem. 2010;75:4648–51. https://doi.org/10.1021/jo100783v.
84. Agarwal HK, Janíček R, Chi S-H, et al. Calcium uncaging with visible light. J Am Chem Soc. 2016;138:3687–93. https://doi.org/10.1021/jacs.5b11606.
85. Brown EB, Shear JB, Adams SR, et al. Photolysis of caged calcium in femtoliter volumes using two-photon excitation. Biophys J. 1999;76:489–99. https://doi.org/10.1016/S0006-3495(99)77217-6.
86. Kantevari S, Matsuzaki M, Kanemoto Y, et al. Two-color, two-photon uncaging of glutamate and GABA. Nat Methods. 2010;7:123–5. https://doi.org/10.1038/nmeth.1413.
87. Olson JP, Banghart MR, Sabatini BL, Ellis-Davies GCR. Spectral evolution of a photochemical protecting group for orthogonal two-color uncaging with visible light. J Am Chem Soc. 2013;135:15948–54. https://doi.org/10.1021/ja408225k.
88. Entcheva E. Cardiac optogenetics. Am J Physiol Heart Circ Physiol. 2013;304:H1179–91. https://doi.org/10.1152/ajpheart.00432.2012.

Optogenetic Tools in the Microscopy of Cardiac Excitation-Contraction Coupling

Lars Kaestner, André Zeug, and Qinghai Tian

General Introduction

Microscopy became a scientific investigation method in the seventeenth century with the application of the first build microscopes on biological samples [1, 2]. Soon it became a popular method to stain samples in order to visualise particular (cellular and subcellular) structures [3]. These stains, either based on absorption or fluorescence, have limitations in respect to their specificity and are often toxic to cells, which limits investigations to short intervals or even dead samples. In 1987 the idea came up to use a fluorescent protein that was discovered 25 years before [4], in particular a green fluorescent protein (GFP) form the medusa *Aequorea victoria* to label cells and cellular structures [5]. With the sequencing and cloning of GFP, a so-called 'green revolution' started, which led to regular usage of fluorescent proteins as markers or sensors (for details see below) in the majority of cellular research in physiology, microbiology, pharmacology, molecular biology, anatomy, cell biology, biophysics and many other biomedical fields. Although the expression of the fluorescent proteins and their optical investigation can already be regarded as optogenetic tools, this term was only applied when the optical properties of proteins were used to manipulate cells. The best-known example of such a protein is the channelrhodopsin, a light-gated ion channel [6, 7]. When this ion channel is expressed in a membrane and illuminated with light of the appropriate wavelength,

L. Kaestner (✉)
Theoretical Medicine and Biosciences, Saarland University, Homburg/Saar, Germany

Experimental Physics, Saarland University, Saarbrücken, Germany

A. Zeug
Institute for Neurophysiology, Hannover Medical School, Hannover, Germany

Q. Tian
Theoretical Medicine and Biosciences, Saarland University, Homburg/Saar, Germany

L. Kaestner, P. Lipp (eds.), *Microscopy of the Heart*,
https://doi.org/10.1007/978-3-319-95304-5_5

the channel will be activated and opened, which results in passive transportation of ions across the membrane and a change of the membrane potential. However, within this chapter we consider both aspects, the observation and the manipulation as optogenetic tools. To use the optogenetic tool, the genes of these proteins need to be transferred into the cells to allow the expression of the protein. For an overview of gene delivery into target cells, see [8].

Quantification of Genetically Encoded Biosensors with a Special Emphasis on Förster Resonance Energy Transfer

The design of genetically encoded biosensors can follow several concepts. One of the early approaches was bimolecular fluorescence complementation [9] that can report protein-protein interactions but does not allow the read-out of fast dynamic processes like excitation-contraction coupling. For biosensors requiring fast kinetics such as calcium- or membrane potential sensors, two engineering strategies have been established: circular permutated fluorescent proteins (CPFP) and sensors taking advantage of the Förster Resonance Energy Transfer (FRET). Both concepts rely on the conformational change of the sensing domain, which induces a spatial rearrangement of the fluorescent protein(s). CPFPs can be described as a switch from a protonated to a deprotonated fluorophore [10] by restricting solvent access to the fluorophore and stabilizing it in an ionized form [11]. This stabilization is supported by extensive contacts between the structure inducing the conformational change and the fluorophore moieties [10]. Apart from the design approach, the application of CPFPs has a significant impact on the recording strategy. CPFPs are often used as equivalents to single-excitation, single-emission small-molecule dye probes. However, some of the CPFPs can also be used in a ratiometric excitation mode, e.g., ratiometric pericam. Despite the relative ease of recording when using the single-excitation single-emission mode, these Ca^{2+} indicators are associated with a number of shortcomings because the measured intensity changes can alternatively be a result of sample movement, inhomogeneous sensor distribution, or changing autofluorescence [12, 13]. In addition to such complications, pH-sensitivity, irreversible or reversible photoconversion, and rather complex intensity relationships can contribute to falsified interpretations of their intensity changes [14].

A real quantitative approach independent on the sensor concentration can be performed taking advantage of the Förster Resonance Energy Transfer (FRET).

FRET is a quantum mechanical effect between two chemical moieties when one is fluorescing and close enough (normally a few nanometers) to another light-absorbing moiety [15, 16]. Already in 1996 variations of the GFP appeared with the clear intention to design biosensors based on FRET [17]. A decent number of FRET-based biosensors have been designed ever since, including sensors to detect cardiac excitation coupling (ECC), like Ca^{2+}-indicators and membrane potential sensors (for details see below). In most of these application cases, FRET-based biosensors are composed of donors and acceptors that are in tandem covalently connected and thus with fixed donor/acceptor stoichiometry. A continuous challenge is the quantitative microscopic

measurement of FRET, because at the wavelength of the donor excitation also a fraction of the acceptor is likely to be excited, and the emission of donor and acceptor is widely overlapping. The difference between the measurement of the pure fluorescence ratio between donor and acceptor and a quantitative FRET analysis in terms of apparent FRET-efficiency (see below) is depicted in Fig. 1. Therefore we provide a short description on quantitative FRET measurements.

The fluorescence from donor and acceptor fluorophores undergoing FRET is the superposition of five quantities: the donor fluorescence from (i) free donor and (ii) donor-acceptor complexes and the acceptor fluorescence from (iii) free acceptor, (iv) directly excited acceptor in donor acceptor complexes and (v) acceptor emission resulting from energy transfer from a donor within a donor-acceptor complex. Due to this complexity, it is apparent that the direct determination of FRET efficiency from

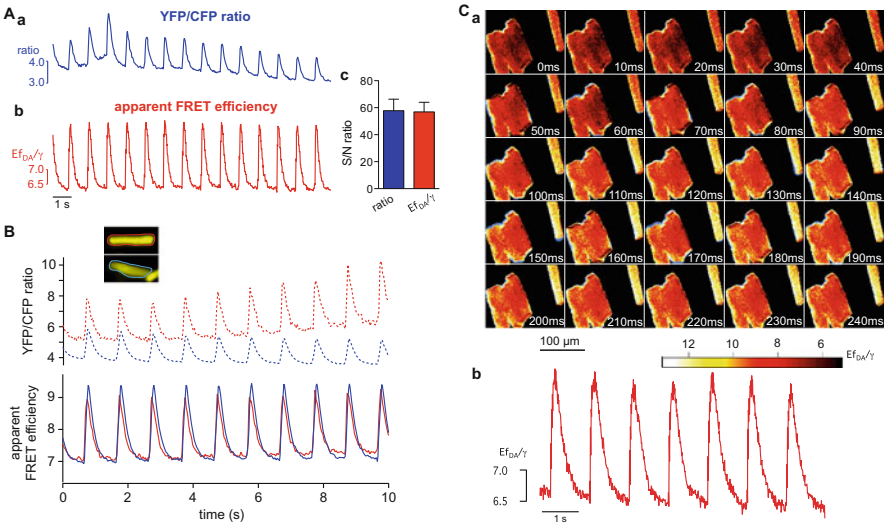

Fig. 1 Comparison of Ca^{2+} transients calculated as the yellow fluorescent protein (YFP)/cyan fluorescent protein (CFP) ratio and apparent Förster resonance energy transfer (FRET) efficiency. (**Aa**) Adult cardiac myocytes expressing YC3.6. The cells were electrically paced, and the resulting CFP and YFP fluorescence were compared after CFP excitation and displayed as the YFP/CFP ratio. (**Ab**) The same Ca^{2+} transients as in (Aa) but displayed as the apparent FRET ratio. (**Ac**) Diagram depicting the signal:noise (S/N) ratio for the two presentation methods. (**B**) Cardiac myocytes expressing YC3.6 were electrically stimulated and analysed. Two representative myocytes displaying substantially different signal transients when calculating simple YFP/CFP fluorescence ratios are shown (dotted lines). Using the same raw data, we calculated the apparent FRET efficiency; the resulting signal transients (solid lines) confirm the expected similar behavior of the two myocytes. (**C**) High-speed recordings of YC3.6 expressing cardiomyocytes. (**Ca**) Image series of a Ca^{2+} upstroke at an image recording frequency of 100 Hz. Each pair of consecutive images was used to calculate the image of the apparent FRET ratio. (**Cb**) Example trace of consecutive Ca^{2+} transients of a single cell recorded at 100 Hz. The multiplicity of infection for all YC3.6 transductions was 4×10^4 pfu/1500 cells. *E* indicates the FRET efficiency; and fDA, fraction of the FRET sensor fluorescent entities. This figure is reproduced from [14], with permission from Wolters Kluwer

spectrally resolved intensity-based measurements is not possible without additional information. To handle the problem that an acceptor emission channel is often polluted by the bleed-through of donor emission, Youvan et al. introduced a filter based method to extract acceptor fluorescence intensity changes while correcting for donor direct acceptor excitation and donor bleed-through [18].

$$nF = F^{ex_D, em_A} - \alpha F^{ex_A, em_A} - \beta F^{ex_D, em_D} \tag{1}$$

For this method, three measurements are required. First, at an excitation wavelength that directly excites the donor, the emission is measured in the acceptor and the donor channels, F^{ex_D, em_A} and F^{ex_D, em_D}, respectively. Next, fluorescence is measured in the acceptor channel F^{ex_A, em_A} at an excitation wavelength that selectively excites acceptor. The amount of donor bleed-through into the acceptor channel is determined by a 'donor-only' measurement, which provides the calibration constant $\beta = F_D^{ex_D, em_A} / F_D^{ex_D, em_D}$. In an 'acceptor-only' measurement, the extent to which the short wavelength excitation directly excites the acceptor is determined relative to the excitation at the longer wavelength. This results in the constant $\alpha = F_A^{ex_D, em_A} / F_A^{ex_A, em_A}$. It should be noted that, while donor bleed-though into the acceptor channel is considered and corrected for, any acceptor bleed-through into the donor channel is neglected. Methods that use these three measurements are collectively known as 'three-cube' methods, due to the necessity of three different filter cubes to perform the measurements. Both calibration constants, α and β, are fluorophore and system specific and may vary with the performance of the device. It is also notable that the nF as provided by Eq. (1) does not represent FRET efficiency, rather it only provides a value that varies with FRET [19]. Specifically, this FRET index varies with donor and acceptor concentration. Several studies have attempted to address this problem by scaling nF by various, somewhat arbitrary combinations of the donor and acceptor signals, but no practical solution was achieved [20–22].

A quantitative solution to determine apparent FRET efficiency from measurements of acceptor intensity was proposed by Lakowicz [23] in the form of

$$Ef_A = \frac{\varepsilon_A^{ex_D}}{\varepsilon_D^{ex_D}} \left(\frac{F_{DA}^{ex_D, em_A} - F_A^{ex_D, em_A}}{F_A^{ex_D, em_A}} \right), \tag{2}$$

where $\varepsilon_D^{ex_D}$ and $\varepsilon_A^{ex_D}$ are the extinction coefficients of the donor and acceptor at donor excitation. It should be noted that the fractional occupancy of acceptor f_A in (2) is denoted with f_D [23]. This equation cannot be directly applied as written, but can only be used in the hypothetical situation that the acceptor in a FRET sample can be measured in absence of donor. More recently, Hoppe and colleagues applied corrections for donor bleed-through and excitation crosstalk to Eq. (2) to quantify apparent FRET efficiency with sensitized emission measurements using a three cube microscope setup [22]. The resulting equation,

$$Ef_A = \gamma \frac{nF}{\alpha F_A^{ex_A, em_A}}, \tag{3}$$

where $\gamma = \varepsilon_A^{ex_D} / \varepsilon_D^{ex_D}$, still requires information about the relative excitability of donor and acceptor at donor excitation wavelength. By applying Eq. (3) to a reference measurement of donor-acceptor tandem construct with known characteristic FRET efficiency, as measured from fluorescence lifetime measurements, γ can be determined. Hoppe et al. further extended this approach by taking into account the donor quenching due to FRET and were able to calculate the donor-dependent apparent FRET efficiency [22]

$$Ef_D = 1 - \frac{F^{ex_D, em_D}}{nF(\xi/\gamma) + F^{ex_D, em_D}}, \tag{4}$$

as well as the donor acceptor ratio

$$R^t \equiv \frac{[A^t]}{[D^t]} = \left(\frac{\xi}{\gamma^2}\right) \frac{\alpha F^{ex_A, em_A}}{nF(\xi/\gamma) + F^{ex_D, em_D}}. \tag{5}$$

To calculate Ef_D and R^t, the constant ξ, which contains information about the donor and acceptor quantum efficiencies and the device detection efficiency, must be determined in a manner similar to γ, by applying reference measurements of a known FRET efficiency construct and solving Eq. (4). Thus, in addition to quantifying α and β from 'acceptor-only' and 'donor-only' reference measurements similarly to Youvan et al. [18], an additional reference measurement of a donor-acceptor tandem construct with known FRET efficiency must be performed in order to determine γ and ξ. Furthermore, the excitation wavelengths and emission channels are constrained as in the calculation of nF, such that ex_A does not excite the donor and no acceptor emission occurs in the donor channel.

Wlodarczyk et al. proposed a new method, linear unmixing FRET (lux-FRET) approach [24], to accomplish correction for bleed-through, crosstalk and unpaired fluorophores in two well separated steps: First, it takes into account bleed-through in a rigorous way by separating spectral components. Thereby it does not need to restrict data acquisition to well-separated spectral channels, but uses photons from the whole spectrum for the fitting process resulting in better efficiency of photon usage [25]. It should be also noted that the equivalent of the three-cube measurement is readily performed using two filter cubes for two excitations, with a beam splitter, which separates emission into two channels. Secondly, for the tandem sensor constructs simplified imaging modes can be employed to measure lux-FRET. For example, after an initial spectrally resolved dual excitation calibration, the user can perform repetitive single excitation wavelength measurements to quantify Ef_D at high temporal resolution. Practically, lux-FRET can be performed on all microscopic devices offering spectral resolution as well as on filter based systems but also on spectrofluorometers.

Excitation-Contraction Coupling

The pumping function of the heart in general and the contraction of the cardiac myocytes in particular are basically characterised by a process called Excitation-Contraction Coupling (ECC). It describes the processing of an electrical signal into the mechanical force [26]. The key player in this mediation is calcium. While the extend of the contraction can be straight forward (optically) recorded by cell length measurements [27], genetically encoded sensors for calcium and voltage will be discussed in dedicated paragraphs below. In similarity the induction or manipulation of ECC by channelrhodopsin will be presented and finally examples from cellular cardiology provided.

GECIs

Genetically Encoded Calcium Indicators (GECI) can be classified as outlined above into two major groups based on their principle of function, these are Circular Permutated Fluorescence Proteins (CPFP) and FRET-based calcium sensors. For a direct comparison of a selection of GECIs with the popular small molecular Ca^{2+}-indicator Fura-2 in cardiomyocytes see Fig. 2. Examples of CPFP based Ca^{2+} sensors include the families of pericams and GCaMPs. Despite the shortcomings of CPFP-based Ca^{2+} indicators, recent iteration of these probes, i.e., GCaMP3-6, offer the best signal-to-noise ratios [32]. Very recently new red-shifted GECIs based on the fluorescent proteins mApple (jRGeCO1a) and on mRuby (jRCaMP1's) were introduced [33] in an attempt to reach the favourable properties of the GCaMP6 series. This goal was partly reached, but smaller maximal fluorescence changes upon Ca^{2+}-binding, a relatively low absorption cross-section and a rather complex intracellular behaviour limit these new probes [33].

An alternative to single fluorophore-based Ca^{2+} indicators is the use of ratiometric Ca^{2+} sensors based on FRET between two different mutants of GFP, similar to the first set of GECI [34, 35]. Both approaches employ Ca^{2+} sensing by calmodulin (CaM) in combination with the Ca^{2+}-dependent interaction of calmodulin and the CaM-binding peptide M13 from the myosin light chain kinase. In cameleons [35], CaM-M13 is sandwiched between CFP and YFP. In these probes, Ca^{2+} binding to CaM is translated into alterations of the steric arrangement between CFP and YFP by a twofold mechanism. First, Ca^{2+} binding to calmodulin itself leads to significant re-arrangement of the EF hands in the molecule. Such steric changes within the molecule result in changes in the CFP-YFP interaction. Nevertheless, the major intramolecular FRET originates from the process of intramolecular interaction of Ca^{2+}-CaM with its binding partner M13. In this process, Ca^{2+}-CaM almost "wraps" around the binding partner, and the entire Ca^{2+}-sensing domain complex drastically changes its arrangement, resulting in a substantial alteration of the CFP-YFP interaction, eventually changing the energy transfer between these two fluorescent proteins (for details see FRET concept above). Additionally, calmodulin-protein interactions might induce cytosolic alterations of the probe properties, such

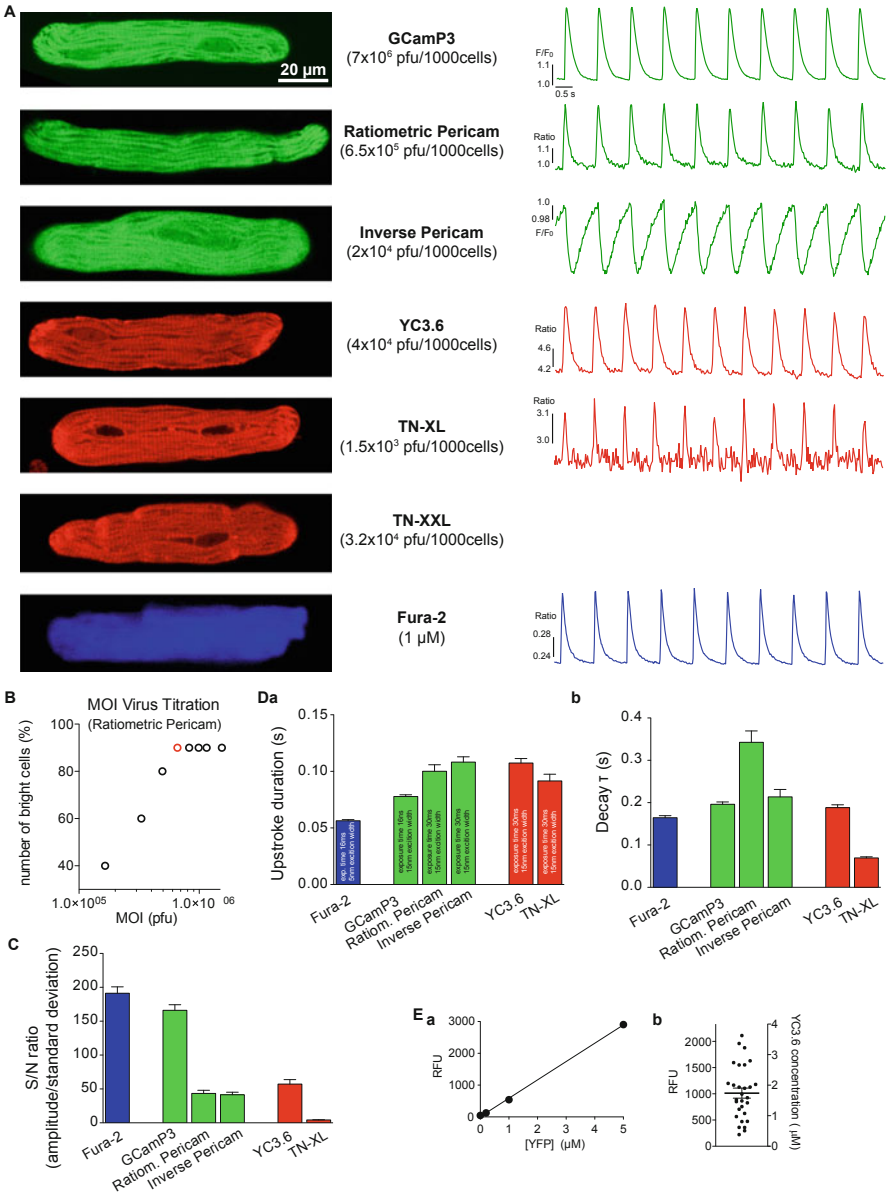

Fig. 2 Comparison of genetically encoded Ca^{2+} indicators expressed in adult ventricular myocytes with Fura-2-loaded cells. (**A**) Examples of Ca^{2+} transients measured with five different genetically encoded Ca^{2+} indicators and Fura-2 under otherwise identical experimental conditions (left, distribution of the fluorescence in myocytes 2 days after transduction; right, typical train of electrically evoked global Ca^{2+} transients). Although the sensor TN-XXL was expressed in cardiac myocytes, it did not report Ca^{2+} changes. Adult rat ventricular myocytes were isolated as previously described [28] and maintained in optimized culture conditions [29] for 3 days. Measurements were performed with a video-imaging set-up as previously described [30] at 34 °C. The multiplicity of infection

side effects include Ca^{2+} responsiveness and intracellular mobility. Observations for genetically encoded Ca^{2+} probes suggest that the Ca^{2+}-sensing domains of the molecules might be either modified by the host cell or altered through protein-protein interactions in the cytosol. There are numerous intracellular interaction partners for calmodulin [36], which include the apo-calmodulin and Ca^{2+}-occupied forms. In both states, calmodulin can in fact serve as both receiver and donor for protein-protein interactions. Apart from changes in the dynamic range and Ca^{2+} affinity of the Ca^{2+} probe, such calmodulin-based sensors might even exert signaling effects, both as a receiver and distributor of subcellular signaling pathways. Apart from the calmodulin domain of the sensors, the intramolecular CaM-binding domain M13 has also been reported to interact with endogenous calmodulin [37]. However, this interaction has been abrogated in a new generation of Ca^{2+} sensors in which the intramolecular calmodulin-M13 interaction has been remodeled so that endogenous calmodulin and CaM cannot bind [38, 39]. A different approach is to avoid employing the ubiquitous calmodulin as a Ca^{2+} binding domain and to make use of the skeletal and cardiac Ca^{2+}-binding protein Troponin C (TnC) [40, 41]. To transfer Ca^{2+} binding into fluorescent changes, genetically encoded Ca^{2+} probes based on TnC use the same approach as calmodulin-based sensors, i.e., FRET between CFP and YFP (or their variants) [37]. In addition to minimized intracellular interference, these indicators also display rapid on and off kinetics because the Ca^{2+}-binding domain (TnC) originates from a very fast Ca^{2+} read-out system, i.e., the contractile machinery of skeletal and/or cardiac muscle. Early versions of these Ca^{2+} probes employed TnC from chicken skeletal muscle (TN-L15) and human cardiac muscle (TN-humTnC) and displayed favorable Ca^{2+} affinities of 1.2 μM and 0.47 μM, respectively [41]. Further molecular evolution yielded molecules with brighter fluorescence, better protein folding (CerTN-L15, K_d = 1.2 μM), and reduced Ca^{2+} affinities (TN-XL, K_d = 2.5 μM) [40]. Because TnC exhibits significant Mg^{2+} binding, its Mg^{2+} affinity was substantially reduced in more advanced versions of these Ca^{2+} probes, such as TN-XL which is characterized by a relatively high K_d for Ca^{2+} of 2.5 μM and an unusually high Hill coefficient of 1.7 [40]. With such a K_d, TN-XL preferentially detects the peak of the Ca^{2+} transients in cardiac myocytes. This restriction to just a part of the signal effectively narrows the apparent time course and reducing the signal-to-noise ratio [14].

Fig. 2 (continued) (MOI) was in the range of 4×10^4 to 7×10^5 pfu per 1500 cells and determined as depicted in (**B**). Example of determination of adenoviral dose for the ratiometric pericam. The MOI marked with the red circle was used for virus transduction. (**C**) Statistical analysis of the signal:noise (S/N) ratio. (**D**) Statistical analysis of (**a**) upstroke duration and (**b**) decay time constant. (**C**) and (**D**), The cumulative data for ≈85 cells per indicator from three independent animal preparations. (**E**) Measurement of the genetically encoded Ca^{2+} indicator concentration in cardiac myocytes according to a previously described method [31]. (**a**) Calibration curve based on confocal measurements of solutions of known yellow fluorescent protein (YFP) concentrations. (**b**) Distribution of relative YFP fluorescence and YC3.6 concentration in virally transduced cardiac myocytes. This figure presents primary experimental results. RFU indicates relative fluorescence units. This figure is reproduced from [14], with permission from Wolters Kluwer

GEVIs

Genetically encoded membrane potential sensors, fluorescent protein based voltage sensors or optogenetic voltage reporters are different synonyms for the same kind of membrane potential probes that are termed GEVI (Genetically Encoded Voltage Indicators) throughout this chapter. Beside all varieties throughout the genesis of GEVIs, they all share voltage sensing domains that are based on (or part of) an integral membrane protein. Therefore the GEVIs will be presented according to the different voltage detection principles (and not like the GECIs according to their fluorescence properties). Regarding the detection principle one can discriminate three different types of GEVIs: based on voltage sensitive conformational changes, microbial opsin-based and sensing non-linear optical properties of fluorescent proteins [42]. However, as a general statement, GEVIs are not yet as mature as GECIs.

The first voltage sensors solely comprising genetically encoded proteins (called FlaSh) fused a wtGFP to the C-terminus of the *Drosophila* Shaker K^+-channel [43]. The second GEVI generated independently was based on the fourth transmembrane segment (S4) of the voltage gated K^+ channel $K_v2.1$ coupled to a CFP/YFP FRET pair in sequence and was named VSFP1 [44]. This sensor was followed by a circular permutated version of the fluorescent protein [45]. The third GEVI type was called SPARC and comprised a GFP fused between domains I and II of the rat skeletal muscle Na^+ channel [46]. Mainly the lack of distinct membrane localization of these three GEVIs [47] made them fail in biological applications. A new generation of GEVIs comprised self-contained voltage sensor domains, such as the voltage sensing domain of the *Ciona intestinalis* Voltage Sensor-containing Phosphatase (Ci-VSP) [48], or voltage sensor domain only proteins [49]. The Ci-VSP domain was chosen by two groups of the same institution (Brain Science Institute, RIKEN, Japan) that independently developed what is now termed VSFP2.x [50] and Mermaid [51]. Especially the VSFP2.x went through several optimisation steps like linker design (VSFP2.3) [52] or choice of fluorescent protein (Clover and mRuby2—VSFP-CR) [53]. However, both constructs, namely VSFP2.3 and Mermaid made it in independent studies into cardiac *in vivo* applications [42, 54, 55], which are compared in Fig. 3. All GEVIs so far share the property of a fast and a slow kinetic response component. While the fast component results from sensing currents within the voltage sensing domain, the slow component is a consequence of the voltage-dependent conformational change in the probe [58]. Seminal work in linker and fluorescent read-out optimization as well as employing voltage sensing domains of voltage-gated phosphatases of other species were performed to shift of the slow sensing component towards faster read-out kinetics [59, 60]. Again these sensors did not make it into biomedical applications because the intensity change per 100 mV voltage change was too low (0.3–0.5%). Based on Mermaid, an improved GEVI was designed using a similar rationale as for the VSFP3.x probes [61] but taking super ecliptic pHluorin [62] as the fluorescent protein. This sensor was named ArcLight and displayed a large fluorescence response of more than 30% per 100 mV voltage change [61, 63]. According to an initial report, the Accelerated Sensor of Action Potentials (ASAP1) is currently the best non-ratiometric GEVI in this group

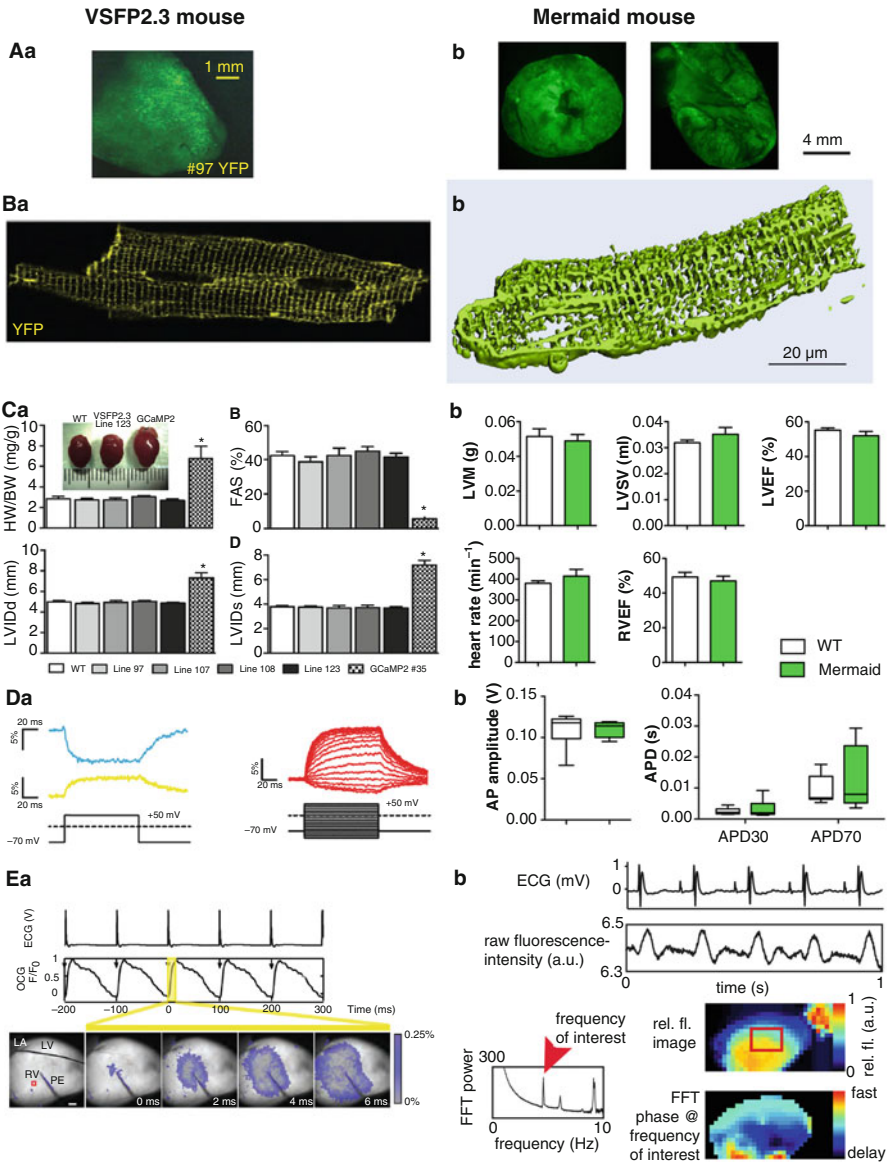

Fig. 3 Transgenic mice expressing a Genetically Encoded Voltage Indicator (GEVI) for optical mapping of the heart. Comparison of mice expressing VSFP2.3 (left, all panels (**a**)) and Mermaid (right, all panels (**b**)). Although slightly different parameters are presented, both mice show consistent data. (**A**) Cardiac appearance of the GEVI expression. (**a**) View of the excised heart; (**b**) Cut open heart: left, short axis; right, long axis; (**B**) Isolated cells expressing the GEVI on the plasmalemma, including T-tubules. (**a**) Confocal section; (**b**) 3D reconstruction based on confocal recordings; (**C**) GEVIs neither alter morphologic nor functional cardiac parameters. (**a**) Echocardiographic based parameters of different VSFP2.3 mouse lines compared to WT and GCaMP2 mice [56]: top left, heart weight to body weight ratio (HW/BW); top right, fractional area shortening

of voltage sensitive fluorescent proteins [64]. It is based on the voltage-sensitive phosphatase of chicken (*Gallus gallus*) and displays around 29% fluorescence intensity change per 100 mV voltage change [65]. In addition, the kinetic was also advantageous, the activation response of the fast component of 2.1 ± 0.2 ms represented approximately 60% of the total signal amplitude [64].

A completely different concept for GEVI design is based on the use of microbial opsins [66] and resulted in the development of sensors named PROBS and Arch [66, 67]. The latter one is derived from the rhodopsin protein, Archaerhodopsin 3 [67]. Microbial opsins bind retinal, a vitamin A-related organic chromophore, and have evolved naturally to function as transducers of light into cellular signals. These proteins are known as tools for optogenetic manipulation [68] (see also below). The natural occurring relationship between light and voltage can be reversed, so that membrane voltage changes are reported as an optical signal. In the initial construct of Arch, the light required for imaging activated a proton current resulting in a contra productive change of the membrane potential. Although a point mutation (D95N) abolished Archs' capacity to elicit light-driven currents, it also impaired the temporal response [67]. A particular interesting variant of Arch(D95N) is it's fusion with the GECI GCaMP5G leading to the dual-function Ca^{2+} and voltage indicator named CaViar [69], which was used to map membrane voltage and calcium in zebrafish heart. The microbial opsin-based GEVIs were improved ever since leading to new versions like QuasAr1 and QuasAr2 [63]. Although the QuasArs display a

Fig. 3 (continued) (FAS); bottom left, diastolic left ventricular inner diameter (LVIDd); bottom right, systolic left ventricular inner diameter (LVIDs). None of the mice lines showed any significant differences except for the comparison with GCaMP2 mice (n = 8 mice per genotype); (**b**) Magnetic resonance imaging based parameters of Mermaid mice compared to WT: top left, left ventricular mass (LVM); top middle, left ventricular stroke volume (LVSV); top right, left ventricular ejection fraction (LVEF); bottom left, heart rate; bottom middle, right ventricular ejection fraction (RVEF). None of the parameters showed significant differences between Mermaid and WT mice (n = 6 mice per genotype); (**D**) Patch-clamp related measurements in mice expressing GEVI. (**a**) Left: representative traces of CFP and YFP in response to a voltage step from −70 to +50 mV in cardiomyocytes expressing VSFP2.3. Right: YFP/CFP ratios in response to a voltage protocol as depicted in cardiomyocytes expressing VSFP2.3, the optical signals show a pronounced delay compared to the command voltage as was also shown for Mermaid in cardiomyocytes [57]; (**b**) Action potential (AP) properties of Mermaid mice compared to WT at a stimulation frequency of 5 Hz: left, AP amplitude; right, AP duration (APD) for 30% and 70% repolarization. None of the parameters showed significant differences between Mermaid and WT mice (n = 10 cells per genotype); (**E**) Proof-of-principle for Langendorff-perfused heart recordings of mice expressing GEVI. (**a**) Synchronous electrical cardiograms (ECG) and optical cardiograms (OCG) supplemented with representative images during 10 Hz electrical pacing via a point electrode; (**b**) Synchronous ECG and raw fluorescence traces (based on the region of interest as indicated by the red rectangle in the relative fluorescence (rel. fl.) image) of an autonomous beating heart (top traces) were subjected to a Fast Fourier Transformation (FFT, left graph). The FFT phase at the frequency of interest (beating frequency of the heart) was visualized for each pixel (bottom right) to map the temporal AP distribution over the heart. Items in the left column (all panels (**a**)) are reproduced from [54], with permission from Wolters Kluwer and items in the right column (all panels (**b**)) are reproduced from [42], with permission from MDPI AG

substantial change in fluorescence intensity per 100 mV change of membrane potential and a fast component of the activation response [63], its overall fluorescence intensity is 30- to 80-fold dimmer than GFP [65]. This might be the reason why QuasArs (at least in our hands) did not work on cardiac myocytes. The combination of fluorescent proteins with a fungal rhodopsin (*Leptosphaeria maculans*) to perform FRET resulted in the development of MacQ-GEVIs with a good responsiveness of around 20% per 100 mV of voltage change and an activation response of the fast component of 2.2 ± 0.2 ms representing approximately 74% of the total signal [70]. A very similar strategy was performed combining QuasAr2 with various fluorescent proteins from eGFP to mKate2 [65].

All previously described approaches using genetically encoded voltage sensors are based on native voltage sensing proteins that functionally rely on protonation or conformational changes, such as voltage dependent protonation of the retinal Schiff base or voltage dependent phosphatases. Their mechanical action towards conformational changes in the sensing domains induce steric alterations in the fluorescent proteins that are utilized to provoke and subsequently measure changes in fluorescence intensity. A different approach is to explore possible interactions between the membrane potential and the chromophore itself. The Stark effect caused by electric field changes is used in small molecular dye-based voltage sensors, e.g. [71]. However, for chromophores of fluorescent proteins this effect is too small to be detected by fluorescence microscopy. This highlights other properties of chromophores that have hardly been appreciated in the development of biosensors in general. These are the non-linear properties allowing the employment of second harmonic generation (SHG) in response to femtosecond pulsed infrared light. The general concept [72, 73] and initial attempts [73, 74] are summarized in [75] but they were not explored further.

Manipulation by Channelrhodopsins

In contrast to the previous sections where light was used to read-out information, channelrhodopsins are proteins that translate light signals into control of cellular function. In some respect this is the genetically encoded variant of caged compounds as outlined in the chapter 'Caged Compounds: Applications in Cardiac Muscle Research' by Niggli and Shirokova within this book. Although there has been a strong interest in light sensitive proteins for decades, the break through came with the discovery and cloning of a faster type of microbial opsins, the channelrhodopsins [6, 7]. Similar as for the genetically encoded indicators initial utilisation and methodological development happened in the field of neuroscience [76]. Most cardiac applications of channelrhodopsins so far are based on the manipulation of tissue or the whole heart and are rather combined with electrical read-outs like multi electrode arrays (MEA) [77–79]. Both approaches are not in the focus of this book that sets the emphasis on microscopic methods. However, we investigated isolated adult cardiomyocytes of mice, where channelrhodopsin-2 was cardiac specific expressed (Fig. 4). As the images show, a 1 ms illumination of light induced contractions in both cells depicted, which shows that the activation of the

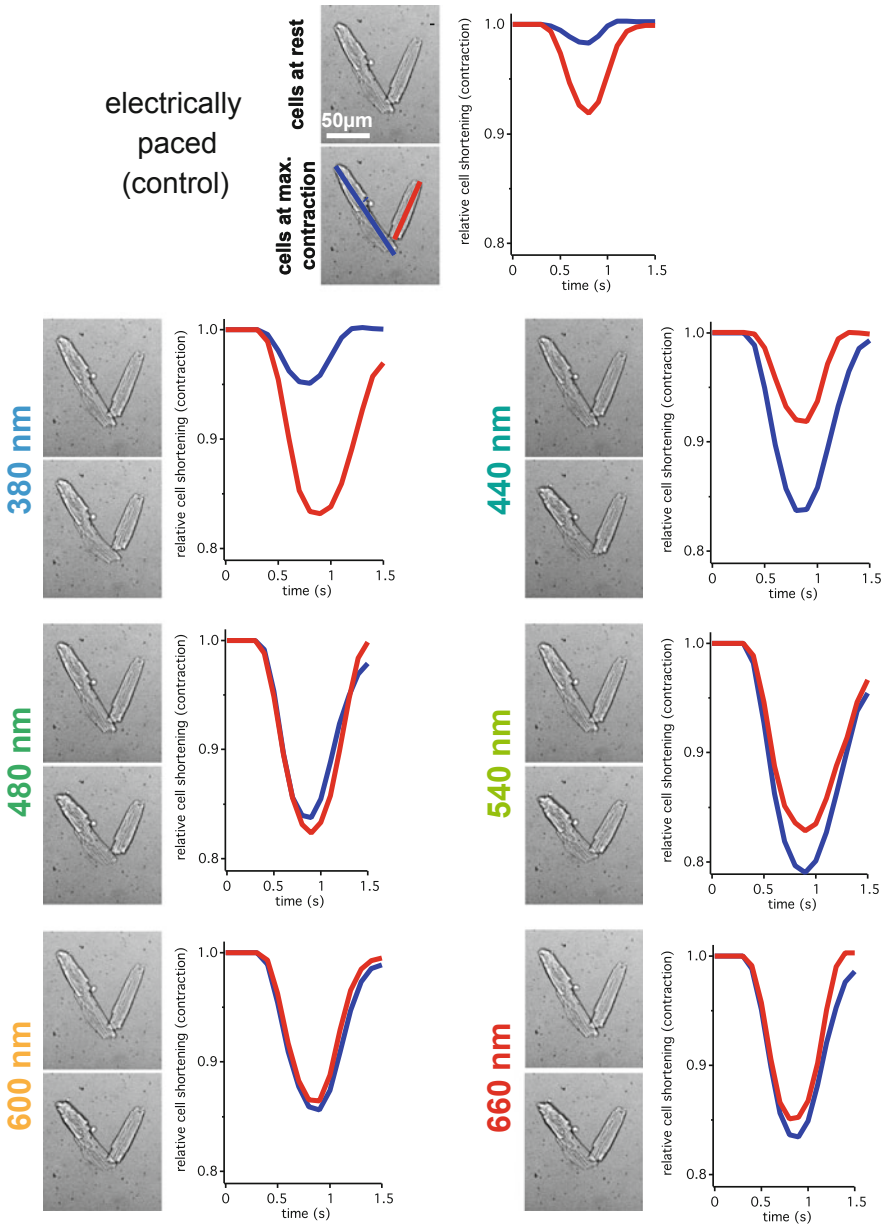

Fig. 4 Adult isolated cardiomyocytes from Chop2YFP mice [80] cross-breeded with a cardiac specific Cre mouse line [81] expressing Channelrhodopsin-2 and YFP were electrically paced as previously described [27] (field stimulation, control) or stimulated with 1 ms light pulses of the given wavelength in a microscopy platform (more, TILL Photonics, Germany) equipped with a monochromator (Polychrome V, TILL Photonics, Germany). For each recording the upper image depicts the cardiomyocytes at rest, whereas the lower one shows the maximal contraction. The graphs show the contractions with the colour codes introduced in the image of the control condition. The contraction of electrically paced cells is less pronounced as the light induced ones. This is caused by the fact that electrical pacing was in a steady state, while optical stimulation reflects post rest potentiation

channelrhodopsin induced an action potential in these cells. At the same time it becomes evident that illumination (as required for imaging approaches) with almost the entire visible spectrum (380–660 nm tested) induces constant openings of the channelrhodopsin. This prevented us from using the optical stimulation in combination with fluorescent probes, e.g., GECI and GEVI as described above.

In light of these properties the development of novel variants of spectrally shifted light gated ion channels, like C2-HR [82] or CheRiff [63], is reasonable. Especially hypochromic shifted spectral properties would open the green and red spectral range for the use of genetically encoded sensors as described above with the goal to perform an all optical observation of ECC from the cellular stimulation to the read-out of action potentials, Ca^{2+}-signals and cellular contraction. Such an approach has recently been performed on human stem-cell derived cardiomyocytes as a proof of principle for cardiotoxicity screens (without cell length recordings) [83]. In this study of electically connected cells in culture, only a subset of cells expressed the channelrhodopsin variant CheRiff while another subset of cells expressed the combined Ca^{2+}/voltage sensor CaViar. Such approaches need specialised microscopes as outlined in the chapter 'Optical Sectioning Microscopy at 'Temporal Super-Resolution'' within this book.

Examples in Cellular Cardiology

Ca^{2+}-Signals in the Nanodomains of Cardiac Myocytes

Although a classical application of genetically encoded Ca^{2+} indicators, the question of Ca^{2+} concentrations in nanodomains near Ca^{2+} transport proteins or in the fuzzy space has only recently been addressed following the introduction of a novel series of CPFPs, the GCaMP6s [32]. These kind of measurements are a functional complementation to the structural superresolution measurements as described in the chapter 'Quantitative Super-Resolution Microscopy of Cardiomyocytes' within this book. Based on the fastest version of the latest GECIs (GCaMP6f), C-terminal fusion proteins of tradin1 and junctin, GCaMP6f-T and GCaMP6f-J, respectively, allowed Ca^{2+} measurements exclusively in the dyadic cleft [84]. The recorded signals were termed 'Ca^{2+} nanosparks', because their calculated volume was approximately 50 times smaller than that of Ca^{2+} sparks. Although the focus of that paper [84] was methodology, the peak intensity (F/F_o) of the nanotransients was 7.8-fold higher than that due to global Ca^{2+} elevation.

Characterisation of the Cellular Cardiac Action Potential Duration and Shape

Conceptual studies of cardiotoxicity screens based on GEVI have been performed with 'Mermaid' [55, 85]. Mermaid compares well with small molecule dyes such as RH-237 or di-8-ANEPPS [86]—we even noticed a 25% higher change of the relative

fluorescence ratio compared to the ratiometric read-out mode of di-8-ANEPPS [87], although the temporal kinetics of Mermaid was much slower than these chemical sensors. In adult cardiomyocytes, pharmaceutical prolongation of the action potential could be detected readily [85]. This prolongation of the action potential duration can be regarded as a cellular equivalent of the QT-interval prolongation in the ECG, which is a pro-arrythmogenic indicator [88]. Differentiating cardiomyocytes from embryonic or induced Pluripotent Stem cells (iPS-cells) for cardiac safety screens as well as for basic research is becoming increasingly popular [89, 90]. In a proof of principle study the combination of human iPS-cells and optogenetics has been successfully performed [83]. However, the stem cell derived cardiomyocytes contain a mixture of different phenotypes, like ventricular myocytes, atrial myocytes or myocytes of the conduction system. All subtypes have a different gene expression, but are morphologically indistinguishable. For the experimental design as well as for further differentiation, it is desirable to purify or just identify a particular subtype of cardiomyocytes. A method to discriminate the cell type is the shape of their action potential, which is characteristic for the subtypes mentioned above [91]. An elegant way to measure such an action potential is by means of a GEVI, was shown for ArcLight and VSFP-CR [42, 92], Fig. 5. Subtype-specific promoters are yet another way to measure such an action potential [94].

Summary

Given the advantages and drawbacks discussed above, there are numerous applications for which GECI and GEVI could prove advantageous, particularly in light of the latest developments of GECI with increased sensitivity [32] and the large momentum, GEVI design and characterization has gained in recent years [42]. However, the selection of the appropriate genetically encoded indicator for a particular application remains challenging. In any case, the intrinsic properties of genetically encoded indicators have to match the dynamics of cardiac myocytes or their subcellular localization to obtain the best results.

The development of GECI and GEVI is far from being at its endpoint. Future research will lead to increased fluorescence yield, enlarged dynamic ranges, and faster sensors. The latter requirement seems to be essential to enable upstroke-based analysis methods of fast confocal recordings, as recently described for Ca^{2+} measurements [95, 96]. Furthermore, biocompatibility must be improved, particularly by reducing cross-talk with endogenous signalling pathways. There is also potential for broad expansion of the spectral range of genetically encoded indicators. There is still a particular demand for indicators with spectral properties shifted into the red or far-red spectral band and at the same time remaining in a limited spectral band. The indicators with bathochromic shifted wavelengths reduce the contribution of autofluorescence and enable better light penetration into the tissue, which is particularly important for *in vivo* imaging approaches with cellular resolution, while the distinct spectral width allows the combination of several biosensors.

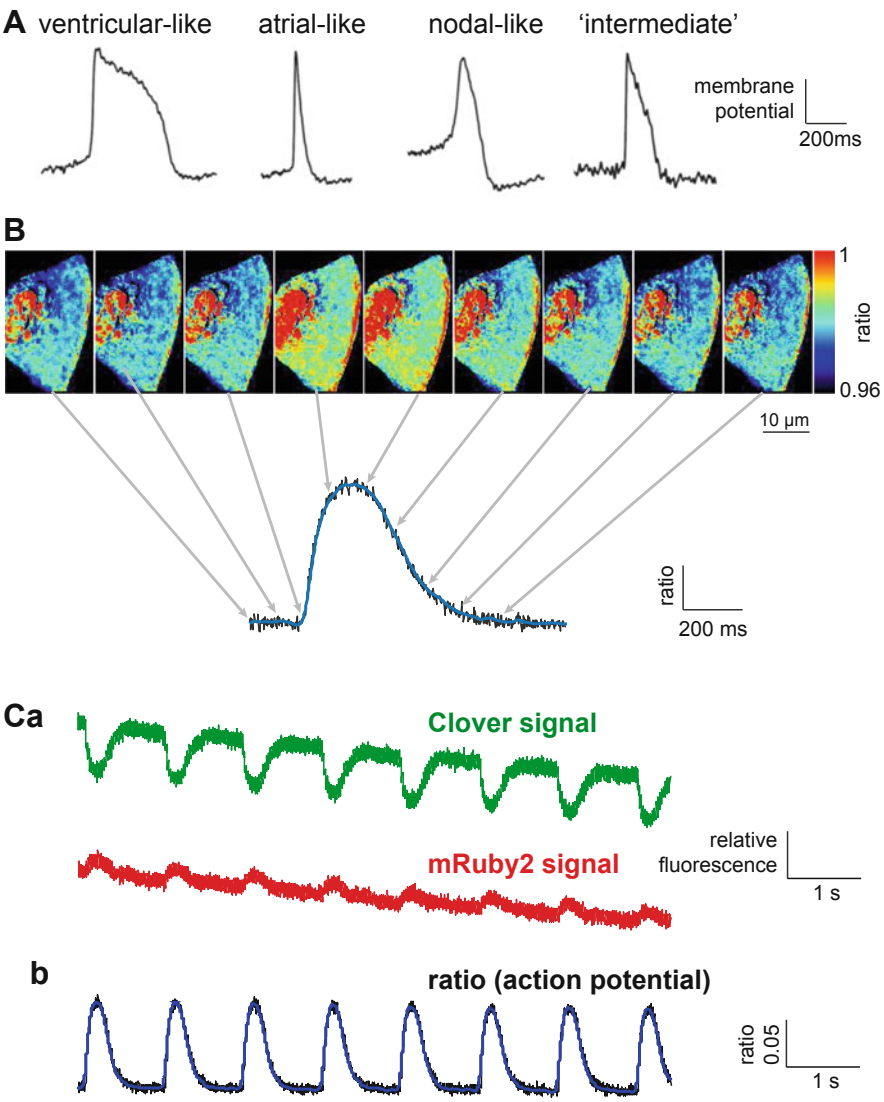

Fig. 5 Voltage-Sensitive Fluorescent Protein Clover-mRuby2 (VSFP-CR) for phenotyping stem cell derived cardiomyocytes. (**A**) Overview of optically recorded (Di-8-ANEPPS) reference action potential phenotypes from induced pluripotent stem cell derived cardiomyocytes. This panel is reproduced from [93], with permission from John Wiley & Sons; (**B**) Recorded image series of a human stem cell derived cardiomyocyte expressing VSFP-CR (Lentiviral gene transfer). The false color ratio images are snapshots every 100 ms of a time series recorded at 500 frames per second using a scientific Complementary Metal-Oxide-Semiconductor (sCMOS) camera and point to the time course of the recorded action potential. Considering the temporal response of the GEVI (Genetically Encoded Voltage Indicators), the example shows most alikeness with an "intermediate" action potential with a tendency to the ventricular phenotype. Overlay of the raw ratio trace (black) and a smoothed trace (blue); (**C**) Original and processed traces of a train of recorded action potentials of an electrically paced (1 Hz) stem cell derived cardiomyocyte. (**a**) Raw traces of the spectral channels for Clover and mRuby2; (**b**) Overlay of the raw ratio trace (black) and a smoothed trace (blue). This figure is reproduced from [42], with permission from MDPI AG

This, in the first place refers to the combination of GECI and GEVI, but also to other types of measurements, such as phosphorylation sensors [97, 98].

Beyond the future developments of optogenetics, their potential field of application is far from being fully exploited. Although the development of GECIs, GEVIs and channelrhodopsins was initially led by applications in neuroscience [99], the examples presented here on cardiac cells pave the way for an application in cardiac topics. It is the responsibility of researchers in the field of cardiovascular sciences to bridge the gap between the availability of optogenetic tools and their appropriate application in cardiovascular studies. We face the situation of a delay between the introduction of the genetic tools and their application, because of intermediate steps, including the generation of transgenic animals or viruses for gene transfer [8] and the establishment of a reproducible and robust read-out mode. In this context, we can expect that recently introduced indicators, novel sensors and light gated ion channels to be developed will replace the optogenetic tools so far used.

References

1. Swammerdam J. Bybel der natuur. London: C. G. Seyffert; 1737.
2. Scientists, A. C. O. D. The collected letters of Antoni Van Leeuwenhoek. Boca Raton, FL: CRC Press; 1996.
3. Milestones in light microscopy. Nat Cell Biol. 2009;11:1165.
4. Shimomura O, Johnson FH, Saiga Y. Extraction, purification and properties of aequorin, a bioluminescent protein from the luminous hydromedusan. Aequorea J Cell Compar Physiol. 1962;59:223–39.
5. Zimmer M. Glowing genes: a revolution in biotechnology. New York, NY: Prometheus Books; 2005.
6. Nagel G, et al. Channelrhodopsin-1: a light-gated proton channel in green algae. Science. 2002;296:2395–8.
7. Nagel G, et al. Channelrhodopsin-2, a directly light-gated cation-selective membrane channel. Proc Natl Acad Sci U S A. 2003;100:13940–5.
8. Kaestner L, Scholz A, Lipp P. Conceptual and technical aspects of transfection and gene delivery. Bioorg Med Chem Lett. 2015;25:1171–6.
9. Hu CD, Chinenov Y, Kerppola TK. Visualization of interactions among bZIP and Rel family proteins in living cells using bimolecular fluorescence complementation. Mol Cell. 2002;9:789–98.
10. Wang Q, Shui B, Kotlikoff MI, Sondermann H. Structural basis for calcium sensing by GCaMP2. Structure. 2008;16:1817–27.
11. Tsien RY. The green fluorescent protein. Annu Rev Biochem. 1998;67:509–44.
12. Coutinho V, Mutoh H, Knöpfel T. Functional topology of the mossy fibre-granule cell--Purkinje cell system revealed by imaging of intrinsic fluorescence in mouse cerebellum. Eur J Neurosci. 2004;20:740–8.
13. Díez-García J, Akemann W, Knöpfel T. In vivo calcium imaging from genetically specified target cells in mouse cerebellum. Neuroimage. 2007;34:859–69.
14. Kaestner L, et al. Genetically encoded Ca^{2+} indicators in cardiac myocytes. Circ Res. 2014;114:1623–39.
15. Förster T. Intermolecular energy migration and fluorescence. Ann Phys. 1948;437:55–75.
16. Tsien RY, Bacskai BJ, Adams SR. FRET for studying intracellular signalling. Trends Cell Biol. 1993;3:242–5.

17. Heim R, Tsien RY. Engineering green fluorescent protein for improved brightness, longer wavelengths and fluorescence resonance energy transfer. Curr Biol. 1996;6:178–82.
18. Youvan DC. Calibration of fluorescence resonance energy transfer in microscopy using genetically engineered GFP derivatives on nickel chelating beads. Biotechnol Alia. 2006;3:1–18. https://doi.org/10.1234/12345678.
19. Berney C, Danuser G. FRET or no FRET: a quantitative comparison. Biophys J. 2003;84:3992–4010.
20. Gordon GW, Berry G, Liang XH, Levine B, Herman B. Quantitative fluorescence resonance energy transfer measurements using fluorescence microscopy. Biophys J. 1998;74:2702–13.
21. Xia Z, Liu Y. Reliable and global measurement of fluorescence resonance energy transfer using fluorescence microscopes. Biophys J. 2001;81:2395–402.
22. Hoppe A, Christensen K, Swanson JA. Fluorescence resonance energy transfer-based stoichiometry in living cells. Biophys J. 2002;83:3652–64.
23. Lakowicz JR. Principles of fluorescence spectroscopy. New York, NY: Springer Science & Business Media; 2013.
24. Wlodarczyk J, et al. Analysis of FRET signals in the presence of free donors and acceptors. Biophys J. 2008;94:986–1000.
25. Thaler C, Koushik SV, Blank PS, Vogel SS. Quantitative multiphoton spectral imaging and its use for measuring resonance energy transfer. Biophys J. 2005;89:2736–49.
26. Bers DM. Cardiac excitation-contraction coupling. Nature. 2002;415:198–205.
27. Viero C, Kraushaar U, Ruppenthal S, Kaestner L, Lipp P. A primary culture system for sustained expression of a calcium sensor in preserved adult rat ventricular myocytes. Cell Calcium. 2008;43:59–71.
28. Kaestner L. et al. Isolation and genetic manipulation of adult cardiac myocytes for confocal imaging. J Vis Exp. 2009; (31).
29. Tian Q, et al. Functional and morphological preservation of adult ventricular myocytes in culture by sub-micromolar cytochalasin D supplement. J Mol Cell Cardiol. 2012;52:113–24.
30. Pahlavan S, et al. Gαq and Gα11 contribute to the maintenance of cellular electrophysiology and Ca^{2+} handling in ventricular cardiomyocytes. Cardiovasc Res. 2012;95:48–58.
31. Kang M, Walker J. Protein kinase C delta and epsilon mediate positive inotropy in adult ventricular myocytes. J Mol Cell Cardiol. 2005;38:753–64.
32. Chen T-W, et al. Ultrasensitive fluorescent proteins for imaging neuronal activity. Nature. 2013;499:295–300.
33. Dana H, et al. Sensitive red protein calcium indicators for imaging neural activity. Elife. 2016;5:413.
34. Romoser VA, Hinkle PM, Persechini A. Detection in living cells of Ca^{2+}-dependent changes in the fluorescence emission of an indicator composed of two green fluorescent protein variants linked by a calmodulin-binding sequence. J Biol Chem. 1997;272:13270–4.
35. Miyawaki A, et al. Fluorescent indicators for Ca^{2+} based on green fluorescent proteins and calmodulin. Nature. 1997;388:882–7.
36. Cox JA. Calcium-calmodulin interaction and cellular function. J Cardiovasc Pharmacol. 1986;8 (Suppl 8):S48–51.
37. Garaschuk O, Griesbeck O, Konnerth A. Troponin C-based biosensors: a new family of genetically encoded indicators for in vivo calcium imaging in the nervous system. Cell Calcium. 2007;42:351–61.
38. Palmer AE, Jin C, Reed JC, Tsien RY. Bcl-2-mediated alterations in endoplasmic reticulum Ca^{2+} analyzed with an improved genetically encoded fluorescent sensor. Proc Natl Acad Sci U S A. 2004;101:17404–9.
39. Palmer AE, et al. Ca^{2+} indicators based on computationally redesigned calmodulin-peptide pairs. Chem Biol. 2006;13:521–30.
40. Mank M, et al. A FRET-based calcium biosensor with fast signal kinetics and high fluorescence change. Biophys J. 2006;90:1790–6.

41. Heim N, Griesbeck O. Genetically encoded indicators of cellular calcium dynamics based on troponin C and green fluorescent protein. J Biol Chem. 2004;279:14280–6.
42. Kaestner L, et al. Genetically encoded voltage indicators in circulation research. Int J Mol Sci. 2015;16:21626–42.
43. Siegel MS, Isacoff EY. A genetically encoded optical probe of membrane voltage. Neuron. 1997;19:735–41.
44. Sakai R, Repunte-Canonigo V, Raj CD, Knöpfel T. Design and characterization of a DNA-encoded, voltage-sensitive fluorescent protein. Eur J Neurosci. 2001;13:2314–8.
45. Knöpfel T, Tomita K, Shimazaki R, Sakai R. Optical recordings of membrane potential using genetically targeted voltage-sensitive fluorescent proteins. Methods. 2003;30:42–8.
46. Ataka K, Pieribone VA. A genetically targetable fluorescent probe of channel gating with rapid kinetics. Biophys J. 2002;82:509–16.
47. Baker BJ, et al. Three fluorescent protein voltage sensors exhibit low plasma membrane expression in mammalian cells. J Neurosci Methods. 2007;161:32–8.
48. Murata Y, Iwasaki H, Sasaki M, Inaba K, Okamura Y. Phosphoinositide phosphatase activity coupled to an intrinsic voltage sensor. Nature. 2005;435:1239–43.
49. Ramsey IS, Moran MM, Chong JA, Clapham DE. A voltage-gated proton-selective channel lacking the pore domain. Nature. 2006;440:1213–6.
50. Dimitrov D, et al. Engineering and characterization of an enhanced fluorescent protein voltage sensor. PLoS One. 2007;2:e440.
51. Tsutsui H, Karasawa S, Okamura Y, Miyawaki A. Improving membrane voltage measurements using FRET with new fluorescent proteins. Nat Methods. 2008;5:683–5.
52. Mutoh H, et al. Spectrally-resolved response properties of the three most advanced FRET based fluorescent protein voltage probes. PLoS One. 2009;4:e4555.
53. Lam AJ, et al. Improving FRET dynamic range with bright green and red fluorescent proteins. Nat Methods. 2012;9:1005–12.
54. Chang Liao M-L, et al. Sensing cardiac electrical activity with a cardiac myocyte--targeted optogenetic voltage indicator. Circ Res. 2015;117:401–12.
55. Tsutsui H, Higashijima S-I, Miyawaki A, Okamura Y. Visualizing voltage dynamics in zebrafish heart. J Physiol (Lond). 2010;588:2017–21.
56. Tallini YN, et al. Imaging cellular signals in the heart in vivo: cardiac expression of the high-signal Ca^{2+} indicator GCaMP2. Proc Natl Acad Sci U S A. 2006;103:4753–8.
57. Tian Q, et al. Optical action potential screening on adult ventricular myocytes as an alternative QT-screen. Cell Physiol Biochem. 2011;27:281–90.
58. Villalba-Galea CA, et al. Charge movement of a voltage-sensitive fluorescent protein. Biophys J. 2009;96:L19–21.
59. Lundby A, Mutoh H, Dimitrov D, Akemann W, Knöpfel T. Engineering of a genetically encodable fluorescent voltage sensor exploiting fast Ci-VSP voltage-sensing movements. PLoS One. 2008;3:e2514.
60. Baker BJ, et al. Genetically encoded fluorescent voltage sensors using the voltage-sensing domain of Nematostella and Danio phosphatases exhibit fast kinetics. J Neurosci Methods. 2012;208:190–6.
61. Jin L, et al. Single action potentials and subthreshold electrical events imaged in neurons with a fluorescent protein voltage probe. Neuron. 2012;75:779–85.
62. Miesenbock G, De Angelis DA, Rothman JE. Visualizing secretion and synaptic transmission with pH-sensitive green fluorescent proteins. Nature. 1998;394:192–5.
63. Hochbaum DR, et al. All-optical electrophysiology in mammalian neurons using engineered microbial rhodopsins. Nat Methods. 2014;11:825–33.
64. St-Pierre F, et al. High-fidelity optical reporting of neuronal electrical activity with an ultrafast fluorescent voltage sensor. Nat Neurosci. 2014;17:884–9.
65. Zou P, et al. Bright and fast multicoloured voltage reporters via electrochromic FRET. Nat Commun. 2014;5:4625.

66. Kralj JM, Hochbaum DR, Douglass AD, Cohen AE. Electrical spiking in *Escherichia coli* probed with a fluorescent voltage-indicating protein. Science. 2011;333:345–8.
67. Kralj JM, Douglass AD, Hochbaum DR, Maclaurin D, Cohen AE. Optical recording of action potentials in mammalian neurons using a microbial rhodopsin. Nat Methods. 2012;9:90–5.
68. Ernst OP, et al. Photoactivation of channelrhodopsin. J Biol Chem. 2008;283:1637–43.
69. Hou JH, Kralj JM, Douglass AD, Engert F, Cohen AE. Simultaneous mapping of membrane voltage and calcium in zebrafish heart in vivo reveals chamber-specific developmental transitions in ionic currents. Front Physiol. 2014;5:344.
70. Gong Y, Wagner MJ, Zhong Li J, Schnitzer MJ. Imaging neural spiking in brain tissue using FRET-opsin protein voltage sensors. Nat Commun. 2014;5:3674.
71. Kuhn B, Fromherz P, Denk W. High sensitivity of stark-shift voltage-sensing dyes by one- or two-photon excitation near the red spectral edge. Biophys J. 2004;87:631–9.
72. Bublitz G, King B, Boxer S. Electronic structure of the chromophore in green fluorescent protein. J Am Chem Soc. 1998;120:9370.
73. Rosell FI, Boxer SG. Polarized absorption spectra of green fluorescent protein single crystals: transition dipole moment directions. Biochemistry. 2003;42:177–83.
74. Khatchatouriants A, Lewis A, Rothman Z, Loew L, Treinin M. GFP is a selective non-linear optical sensor of electrophysiological processes in *Caenorhabditis elegans*. Biophys J. 2000;79:2345–52.
75. Kaestner L, Tian Q, Lipp P. In: Jung G, editor. Action potentials in heart cells. New York, NY: Springer; 2012. p. 163–82.
76. Entcheva E. Cardiac optogenetics. AJP Heart Circ Physiol. 2013;304:H1179–91.
77. Bruegmann T, et al. Optogenetic control of heart muscle in vitro and in vivo. Nat Methods. 2010;7:897–900.
78. Vogt CC, et al. Systemic gene transfer enables optogenetic pacing of mouse hearts. Cardiovasc Res. 2015;106:338–43.
79. Ambrosi CM, Klimas A, Yu J, Entcheva E. Cardiac applications of optogenetics. Prog Biophys Mol Biol. 2014;115:294–304.
80. Scheller A, Bai X, Kirchhoff F. The role of the oligodendrocyte lineage in acute brain trauma. Neurochem Res. 2017; https://doi.org/10.1007/s11064-017-2343-4.
81. Wiesen K, et al. Cardiac remodeling in Gαq and Gα11 knock out mice. Int J Cardiol. 2016;202:836–45.
82. Prigge M, et al. Color-tuned channelrhodopsins for multiwavelength optogenetics. J Biol Chem. 2012;287:31804–12.
83. Dempsey GT, et al. Cardiotoxicity screening with simultaneous optogenetic pacing, voltage imaging and calcium imaging. J Pharmacol Toxicol Methods. 2016;81:240. https://doi.org/10.1016/j.vascn.2016.05.003.
84. Shang W, et al. Imaging Ca^{2+} nanosparks in heart with a new targeted biosensor. Circ Res. 2014;114(3):412. https://doi.org/10.1161/CIRCRESAHA.114.302938.
85. Tian Q, et al. Optical measurement of action potential in adult ventricular myocytes. Biophys J. 2011;100:292a.
86. Haugland RP. Handbook of fluorescent probes and research products. Eugene, OR: Molecular Probes; 2002.
87. Kaestner L, Tian Q, Lipp P. Cardiac safety screens: molecular, cellular, and optical advancements. In: Lin CP, Ntziachistos V, editors. Biomedical optics III, vol. 8089. Munich: SPIE; 2011. p. 80890H-1–6.
88. Arrigoni C, Crivori P. Assessment of QT liabilities in drug development. Cell Biol Toxicol. 2007;23:1–13.
89. Sinnecker D, et al. Induced pluripotent stem cells in cardiovascular research. Rev Physiol Biochem Pharmacol. 2012;163:1. https://doi.org/10.1007/112_2012_6.
90. Matsa E, Burridge PW, Wu JC. Human stem cells for modeling heart disease and for drug discovery. Sci Transl Med. 2014;6:239ps6.

91. Dorn T, et al. Direct Nkx2-5 transcriptional repression of Isl1 controls cardiomyocyte subtype identity. Stem Cells. 2015;33:1113. https://doi.org/10.1002/stem.1923.
92. Leyton-Mange JS, et al. Rapid cellular phenotyping of human pluripotent stem cell-derived cardiomyocytes using a genetically encoded fluorescent voltage sensor. Stem Cell Rep. 2014;2:163–70.
93. Nagai T, Sawano A, Park ES, Miyawaki A. Circularly permuted green fluorescent proteins engineered to sense Ca^2. Proc Natl Acad Sci U S A. 2001;98:3197–202.
94. Chen Z, et al. Subtype-specific promoter-driven action potential imaging for precise disease modelling and drug testing in hiPSC-derived cardiomyocytes. Eur Heart J. 2017;38:292–301.
95. Tian Q, Kaestner L, Lipp P. Noise-free visualization of microscopic calcium signaling by pixel-wise fitting. Circ Res. 2012;111:17–27.
96. Tian Q, Kaestner L, Schröder L, Guo J, Lipp P. An adaptation of astronomical image processing enables characterization and functional 3D mapping of individual sites of excitation-contraction coupling in rat cardiac muscle. Elife. 2017;6:665.
97. Violin JD, Zhang JX, Tsien RY, Newton AC. A genetically encoded fluorescent reporter reveals oscillatory phosphorylation by protein kinase C. J Cell Biol. 2003;161:899–909.
98. Schleifenbaum A, Stier G, Gasch A, Sattler M, Schultz C. Genetically encoded FRET probe for PKC activity based on pleckstrin. J Am Chem Soc. 2004;126:11786–7.
99. Knöpfel T, Gallero-Salas Y, Song C. Genetically encoded voltage indicators for large scale cortical imaging come of age. Curr Opin Chem Biol. 2015;27:75–83.

Electron Microscopy

Sergio Bertazzo

Introduction

In this chapter I will provide the initial and basic steps to the use of electron microscopy in the study of cardiac tissues and biological samples in general. My main objective is to enable the reader to understand the basic principles of electron microscopy and use this knowledge as a guide for choosing samples eligible for use in microscopes. I also want to get the reader excited about the wealth of information that could be obtained from this kind of microscopes applied to cardiovascular research. By reading this chapter, you should be able to start to experiment with microscopes and samples and even obtain basic images on the electron microscope, thus revealing some of the ultrastructure present in the cardiac tissues.

It is not my intention to explain all the details of the techniques involved in electron microscopy studies of biological samples here, since there are specialised books on the topic already doing that job and several articles [1–5] and books [6–10] have been published about the subject. It should be noted that electron microscopy sample preparation methods are not standardised, and different researchers will have different protocols that can produce images of the same quality. In this way, I strongly encourage you to follow up the reading of this chapter with more specialized texts, and look for a deeper understanding of the topic. I also suggest you shadow colleagues that have experience with the technique. Electron microscopy, and this is particularly true for biological samples, is almost an art and can only be fully learned by experience.

S. Bertazzo (✉)
Department of Medical Physics and Biomedical Engineering, University College London, London, UK
e-mail: s.bertazzo@ucl.ac.uk

L. Kaestner, P. Lipp (eds.), *Microscopy of the Heart*,
https://doi.org/10.1007/978-3-319-95304-5_6

Ultrastructure

The most common representation today for any cell is a circle representing the outer membrane and an inner circle for the nucleus, surrounded by scattered cell organelles. Perhaps two of the most iconic organelles are the mitochondria, with their distinctive double membrane, and the Golgi apparatus, with its various membranes. These more refined details (membranes and other internal structures) are a good example of the ultrastructure present in cells. The ultrastructure is, in a few words, the set of structures found at the nanoscale.

The most common way to image the ultrastructure from cells is by electron microscopy. It is also the best way to obtain an overall image, where the signal or information is not targeted to specific structures or proteins of tissues and cells. Electron microscopes today are able to easily magnify by thousands of times (it is even quite common to find the nominal resolution at sub Angstrom scale).

Electron microscopes are based on how electrons interact with samples. There are two types of basic electron microscopes: the Scanning Electron Microscope (SEM) and the Transmission Electron Microscope (TEM). Both use a source of electrons but produce completely different information and demand different sample preparation procedures.

Fundamentals of Electron Microscope

Put briefly, electron microscopes are a source of electrons in a column with vacuum where electrons are accelerated, interact with a sample and then reach a detector (Fig. 1).

In a SEM, an electron beam is focused on the surface of a sample to scan it. The image is generated either by the electrons that bounce back to a detector (in this case, a backscattering electron detector) or by secondary electrons (that are generated on the surface by the bombardment of the surface with the original electron beam) that are recorded by a secondary electron detector.

Similarly, to what happens in an optical microscope, where the light passes through the sample, in a TEM the electron beam is focalised on the sample so that the electrons pass through the sample and the interaction between these and the sample is recorded in detector, placed below the sample. Therefore, the sample should be as thin as possible (generally below 100 nm in thickness). This particular requirement has important consequences for the preparation of biological samples.

Imaging Biological Samples

Image formation depends only on the topography of the sample when using SEM with the secondary electron detector (the most common detector, present in every SEM). This allows for simple planning for the imaging work, since no attention must be paid to the composition of samples.

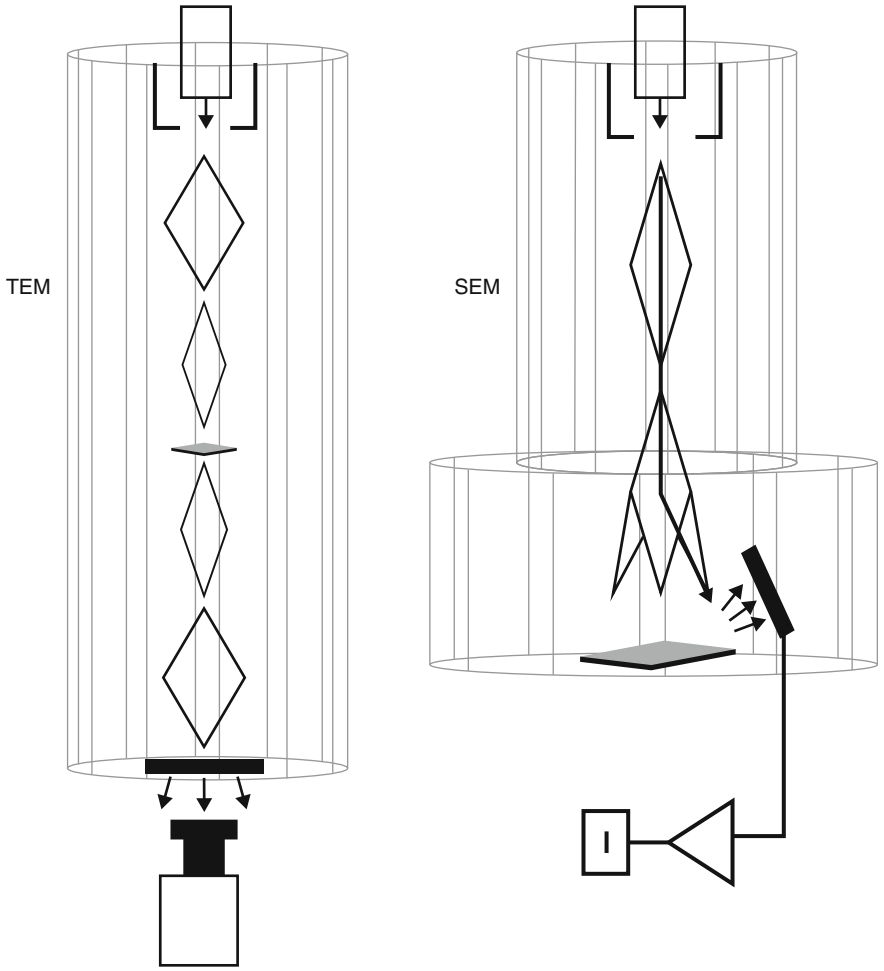

Fig. 1 Schematic of electron beam path in a (**a**) transmission electron microscope (TEM) and (**b**) scanning electron microscope (SEM). In the TEM, the electrons generated at the top of the column and accelerate towards the samples, passing through them and arriving at the camera. In the SEM, the electrons generated at the top of the column accelerate towards and bombard the surface of the sample and then either the electrons generated or those that bounce back are directed towards a detector

The only consideration that is important for biological samples is that the majority of SEM equipment operates at vacuum. Since the electron beam is focused on the surface of each sample, any excess electrons in the surface must be dissipated. It is therefore a requirement that surface of the sample should be conductive, and the way to overcome this restriction for biological samples is to add a metallic or carbon conductive layer on the surface of the sample.

For TEM, the contrast in images from biological samples arises from the interaction between electrons and the different components of samples. In this way, it is really important to consider the composition. The contrast on the final image is proportional to the atomic number (Z) of the chemical elements in a sample. Areas of the sample presenting elements with higher Z will look darker compared to regions presenting lighter elements. Latest equipment generally have a built-in CCD camera for detection and automatically correct levels of brightness. This auto-correction feature must be kept in mind, since some information of the sample can be lost.

Biological samples are mostly composed of carbon, and in this way, staining agents must be used to increase contrast. Latest microscopes equipped with digital cameras partially offset the lack of a contrast agent by digitally increasing contrast. Image quality, however, is severely compromised (Fig. 2a, b).

Contrast Agent

Because the contrast on TEM images is relative to the Z, heavier elements will give a stronger contrast. In this way, most contrast agents for the staining of biological samples are actually composed of heavy metals, which selectively stain components of cells and tissues. The most common stain used is Osmium Tetroxide (OsO_4). Because it oxidizes unsaturated bounds on fat acids [6], it is the perfect staining agent for any of the membranes in cells (Fig. 2e, f). Indeed, most of the structures seen in TEM images of cells in the literature derive from the Os on lipid membranes.

Another common reagent used is Uranyl Acetate ($C_4H_6O_6U$), which reacts with amino and phosphate groups [11], thereby staining mainly nucleic acids and proteins (Fig. 2c, d). Uranyl acetate is the best option for staining when the structure of interest is proteins in cells and tissues.

One of the most common procedures for the preparation of biological samples for TEM uses the combination of Osmium Tetroxide and Uranyl Acetate. In this way, the procedure allows simultaneous imaging of membranes and some of the structures of proteins.

In addition to these two main staining agents, Lead Citrated and Iron Cyanide, among others are also commonly used [6, 11]. Each of the different stains will improve the observation of specific structures.

Sample Preparation

The main challenge and difficulty related to the imaging of biological samples with electron microscopes is successful sample preparation. Since electron microscopes operate in vacuum and biological samples are generally rich in water, several methods have been developed to dehydrate them with minimum alteration to their ultrastructure. More specifically and in addition to dehydration, TEM imaging requires that samples be thin enough or sectioned in thin slices.

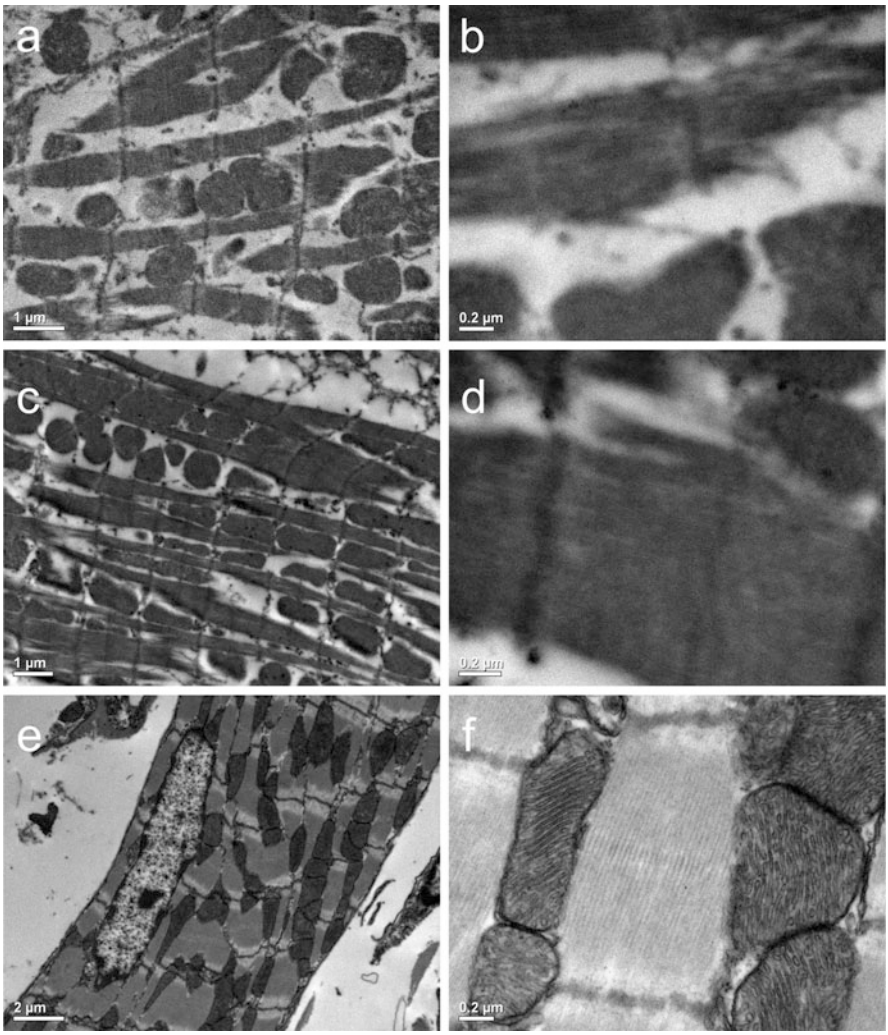

Fig. 2 Transmission electron micrographs of cardiac muscle with (**a**, **b**) no staining, (**c**, **d**) stained with uranyl acetate and (**e**, **f**) stained with uranyl acetate and osmium tetroxide

For SEM, however, samples basically need to be dehydrated following a procedure that prevents the collapse of internal structures during the process of drying. For the TEM, samples must be dehydrated and infiltrated by a resin, which will keep the ultrastructure together and allow the sectioning of the sample thinner than 100 nm. Even though sample preparation methods may be significantly different between SEM and TEM, both start with sample fixation, in order to keep components in place during the dehydration procedure.

Fixation

Biological samples may be fixated in a 4% (w/v) formaldehyde in phosphate buffered saline solution at room temperature. It is also quite common to use a mix of fixatives, such as 4% (w/v) formaldehyde with 0.2% (w/v) glutaraldehyde solution in phosphate buffered saline solution.

If necessary, the sample (tissue or other) must first be cut in small pieces (the smaller, the better since this will help later with the infiltration of the fixative, dehydratation and staining processes). The small pieces must then be immersed in the solution of the fixative (Fig. 3b). For cardiac tissue, it is better fix samples for least 1 day immediately upon harvesting. The main concern with the fixation process is that the fixative has to fully infiltrate the tissue and, for this reason, larger samples will demand a longer time for fixation.

The decision of which fixative to use is mainly based on the fact that formaldehyde can infiltrate faster in samples and, in this way, cross link proteins faster than glutaraldehyde. On the other hand, glutaraldehyde offers a more permanent fixation that formaldehyde, but is slower to fix the sample and can also affect the antigenicity of the sample, if used in excess. A rule of thumb is for a faster fixation, use formaldehyde, and if you are not too worried about the antigenicity of the sample, use a mixture of both fixatives. It is also important to stress that some variation on the concentration of the fixatives does not have a significant effect on the images obtained.

Contrast Agent for TEM Imaging

As mentioned earlier, in the section dealing with how images are created, biological samples must be stained with heavy metals for TEM, and the most common and simple stains used are osmium tetroxide and uranyl acetate.

To use these staining agents, first prepare a solution of osmium tetroxide of 2% (w/v) in cacodilate buffer (smaller concentrations may also be used, and the best concentration will be dependent sample and also related to the time of exposure of the sample to the osmium tetroxide solution) and a solution of uranyl acetate 2% (w/v) cacodilate buffer.

Take, for instance, fixed small pieces of heart tissue and immerse in cacodylate buffer or HEPES buffer for 15 min (phosphate buffer oxidises osmium tetroxide and can reduce the staining quality). After this, immerse the tissue in the osmium solution at room temperature for 30 min to 1:30 h (the exact time will depend on the sample and on the concentration of osmium). Wash the sample five times with deionised water and proceed to the dehydration protocol (Fig. 3c).

Uranyl acetate may be used to stain proteins. The procedure consists in placing sections of the sample embedded in resin onto a drop of uranyl acetate for 5 min and then washing with deionized water.

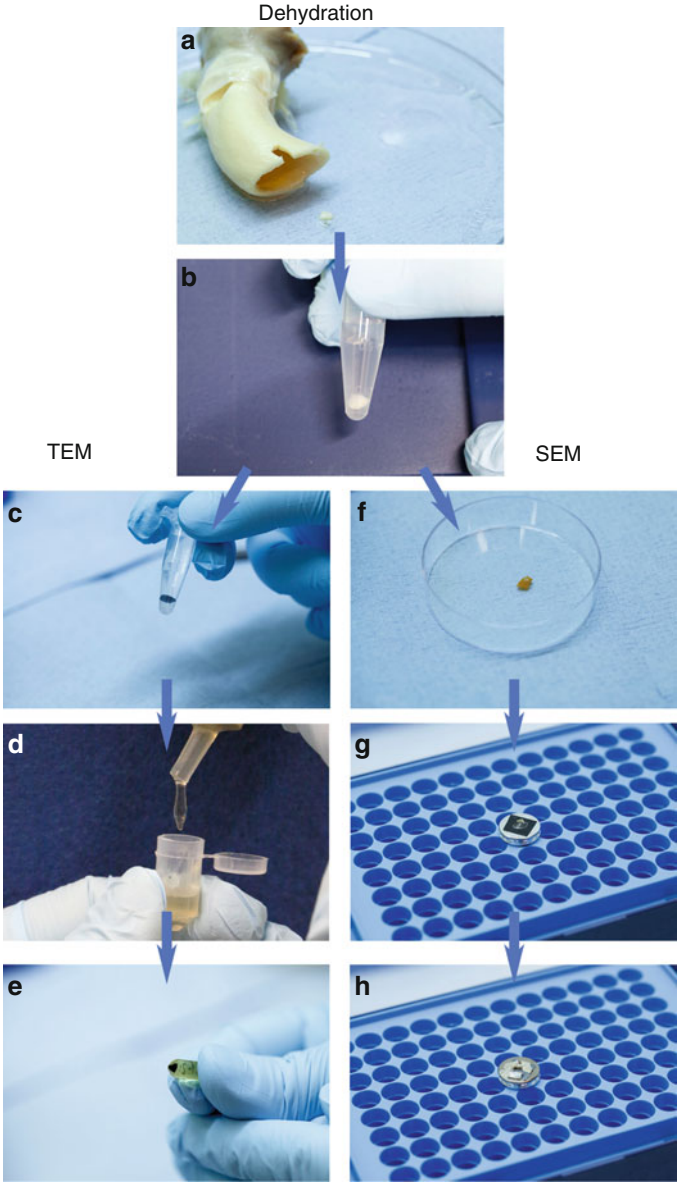

Fig. 3 Cardiac tissue sample preparation for (I) transmission electron microscopy and (II) scanning electron microscopy. (**a**) Dissection of tissue after fixation in 4% formaldehyde. (**b**) Dehydration process with series of ethanol grades. (**c**–**e**) Resin infiltration and final resin block with sample embedded. (**f**–**h**) Dehydrated sample after critical point dry, mounted on aluminium SEM sample holder with silver paste

Dehydration

The dehydration protocol is the same for samples to be imaged by SEM or TEM. Following fixation and staining the biological sample is immersed in a series of ethanol dilution from most diluted to pure ethanol.

The best protocol for cardiac tissue would be to use a series of graded solutions from 20% (v/v) to pure ethanol at intervals of 10% for at least 1 h. The time and number of different concentrations will be dependent on the size of the tissue samples to be dehydrated. Larger pieces will require a longer time and more solutions should be used. After the series of solutions, it is recommended that the tissue be immersed in pure ethanol for a further three times, to secure a complete dehydration.

SEM Sample Preparation: Final Steps

For SEM imaging, all the liquid in a sample must be removed in a way that does not modify their nanostructure due to capillary forces from the drying process. There are two methods to preserve the nanostructure. Known as critical point drying, the first method consists in using CO_2 at the supercritical state to initially substitute the ethanol in the sample and then dry it without damaging its nanostructure. This method is considered to be the best for preparing biological samples for SEM.

The second method consists in immersing samples in Hexamethyldisilazane (HMDS) after the last immersion in pure ethanol. HMDS will also dry the samples while preserving the nanostructure. After the last ethanol immersion, samples must be immersed in pure HMDS for as long as they were left in pure ethanol (ensuring, in this way, a complete substitution of ethanol with HMDS) and be allowed to air dry. Although this method might be considered somewhat inferior to the critical point dryer, it is much more convenient and presents excellent results for cardiac tissue.

TEM: Resin Embedding

For TEM imaging, it is necessary that the sample be sectioned in slices of ~100 nm, while keeping the internal ultrastructure in place. To achieve that, after dehydratation, the sample must be infiltrated by resin. Different resins are used today for embedding, and the most common are basic epoxy resins [12].

To infiltrate resin on samples, immerse them after dehydration into the epoxy resin diluted in ethanol at 3:1, 2:1, and 1:1 for 3 h each, and then overnight at 1:2. Replace the solution with pure resin change it every 6 h and then allow to infiltrate overnight again. After that, immediately place samples in an oven at 60 °C and left to cure overnight (Fig. 3e).

An ultramicrotome must be used for the sectioning of cured resin blocks. Samples should be sectioned at 100 nm and then placed on copper grids for imaging by TEM (Fig. 4). Resin block sectioning requires skill and experience dramatically improves results.

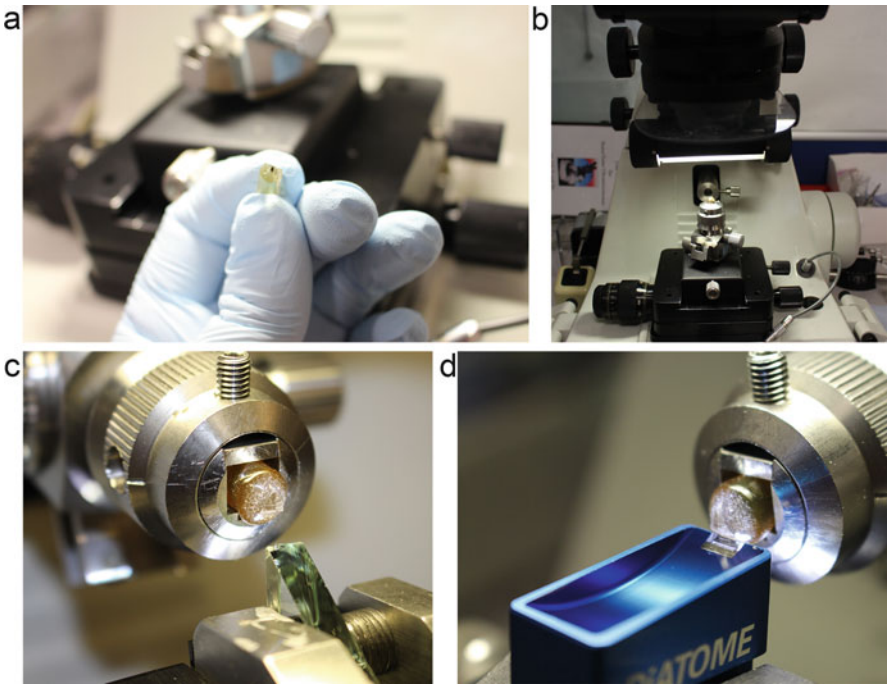

Fig. 4 (**a–d**) Resin block with embedded sample ultrathin sectioning with ultramicrotome. The resin block is attached to the ultramicrotome and initially trimmed with a glass knife, then sectioned at 100 nm with a diamond knife

Imaging

SEM

For SEM imaging, dried samples are attached to a metallic sample holder using carbon tape and silver paint (the latter can help considerably with the conductivity of the sample), and then coated with 10 nm of a metal layer.

Several metal coatings are available, gold being the most common. Gold is a fine option, since it is one of the most stable metals and presents good conductivity, but at higher magnification produces structural artifacts on the surface, such as a characteristic fracture pattern (Fig. 5).

After the coating with a conductive layer, the sample is ready for imaging by SEM. Different types of detectors can be attached to a SEM, such as a secondary detector and a backscattering detector. For the first one, the best images will have used lower voltages, such as 5 kV (Fig. 6a) and for the latter, the best images will require higher voltages, in the range of 10 kV (Fig. 6b).

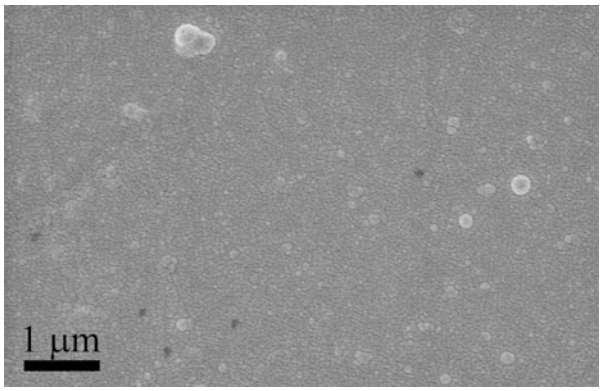

Fig. 5 Scanning electron micrograph of surface coated with gold, where the 'cracked' surface created by an excess of gold coating is visible

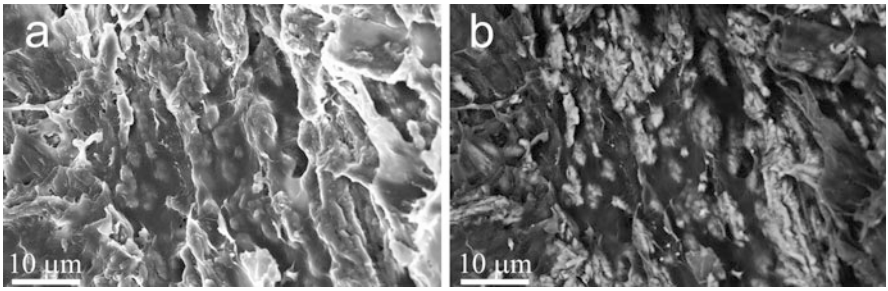

Fig. 6 (**a**) Scanning electron micrograph from calcified cardiac tissue obtained using secondary electron detector. (**b**) Scanning electron micrograph from the same area in a imaged using the backscattering detector. The bright regions indicate calcification

TEM

Grids with sections from samples require no further preparation before insertion in the TEM (Fig. 7). For biological samples, smaller voltages are the best option, as they increase the contrast significantly, helping in this way the visualization of the ultrastructure. In this way, the most common voltage used is 80 kV, as can be seen in the images presented in Fig. 2.

Electron Microscopy and Cardiovascular Research

Electron microscopy is now commonplace in cardiovascular research. The most directly way it has been applied is to establish the ultrastructure of cardiac tissue (Fig. 8), where TEM micrographs are able to clearly show the main organelles and the ultrastructures present in the tissue, such as mitochondria and myofibrils (Fig. 8).

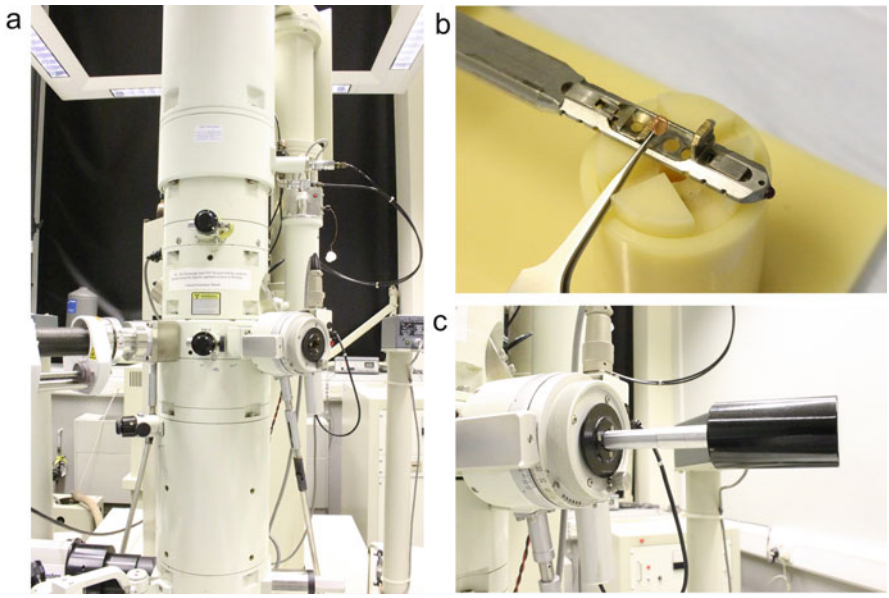

Fig. 7 (**a**) Transmission electron microscope. (**b**) Copper grid supporting the ultrathin sections placed on the TEM grid holder. (**c**) Grid holder introduced in the TEM

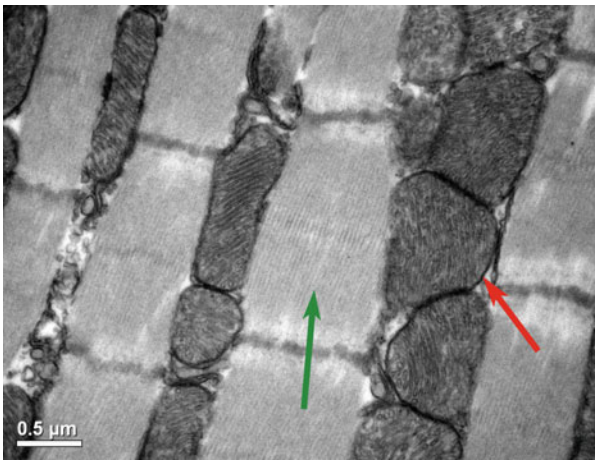

Fig. 8 Transmission electron micrographs of cardiac muscle featuring mitochondria (red arrows) and myofibrils (green arrow)

The same techniques have been applied in research looking to understand how pathologies can affect tissue ultrastructures and the literature contains several examples of this method used together with other methods in the research of cardiovascular diseases [13, 14].

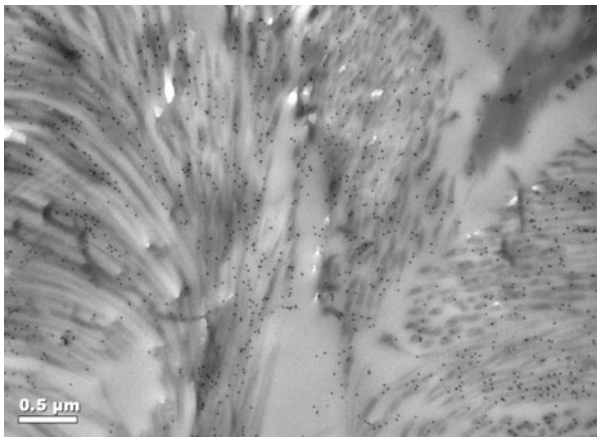

Fig. 9 Transmission electron micrographs with example of immunogold application to aorta wall to identify the location of collagen fibers. Black dots are gold nano particles coated with anti-collagen antibodies that attached to the collagen fibers shown in the micrograph

Another way in which TEM is extensively applied to cardiac research is immunogold. As in fluorescence microscopy, in TEM with immunogold proteins can be tagged and imaged. However, instead of a fluorophore, a heavy metal nanoparticle is used (generally gold nanoparticles) for tagging and these particles are associated to the protein of interest, therefore providing the specific location of those proteins. The sample preparation protocol for immunogold is similar to the procedure used for fluorescence microscopy [15, 16], except for the use of a secondary antibody attached to a gold nanoparticle, the dehydration and coating steps described earlier for SEM, and the resin infiltration and sectioning described earlier for TEM.

The main advantages of immunogold over fluorescence microscopy are that it not only provides the spatial localization of a protein of interest (Fig. 9—gold nanoparticles attached to collagen fibers of cardiac vascular tissue) but also allows observation of the ultrastructure of the tissue surrounding these proteins, which simply cannot be achieved by fluorescence microscopy. The literature has several examples of the application of the TEM with immunogold method to study cardiovascular tissue [17], and it is probably one of the varieties of electron microscopy most widely used in cardiac research.

SEM has also been extensively applied in cardiac research, more specifically to the study of cardiovascular calcification. SEM is particularly suitable for the research of this kind of pathology because its different image modes can identify inorganic components in tissues, a feature that is useful in the case of calcific diseases. Research using SEM has demonstrated that cardiovascular calcification is a unique biomineralization process whereby the resulting mineral is not found in any other tissue of vertebrates [2, 18–21]. By SEM, it is also possible to show that the first calcified structures formed in the soft tissues are spherical particles made of calcium phosphate (Fig. 10). Furthermore, the combined application of SEM and TEM has shown that these particles present a unique mineral that cannot be found in any other region of the body [2]. Also by SEM it is possible to demonstrate that as the disease progresses, calcified fibers can be found in the tissue (Fig. 11) and at more advanced stages, a compact calcification is also present in the affected tissue (Fig. 12).

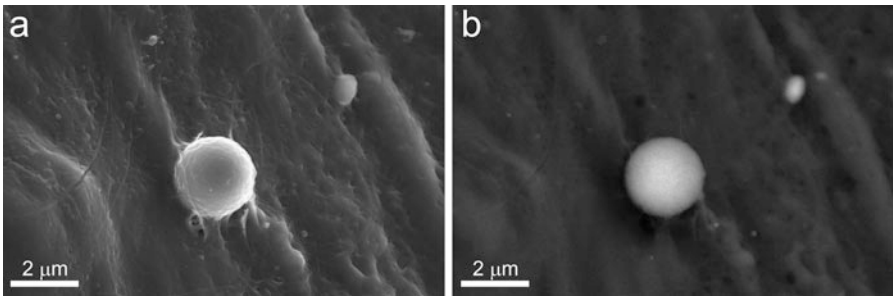

Fig. 10 Scanning electron micrograph of aorta tissue sample acquired using secondary electron detector (**a**) and backscattering detector (**b**) and featuring calcified particle present on that tissue

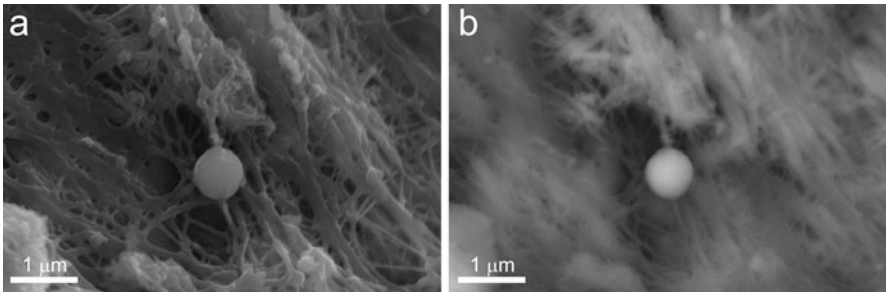

Fig. 11 Scanning electron micrograph of aorta tissue sample acquired using secondary electron detector (**a**) and backscattering detector (**b**) and featuring calcified particle and fibers present on that tissue

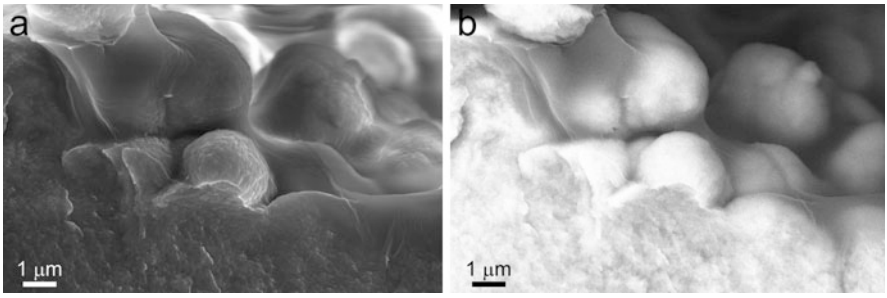

Fig. 12 Scanning electron micrograph of aorta tissue sample acquired using secondary electron detector (**a**) and backscattering detector (**b**) and featuring compact calcification present on that tissue

These studies are relevant examples of how the use of electron microscopy can provide fundamental insights into the biology of the cardiac tissue, and perhaps more importantly, into the biology of diseases affecting the cardiovascular tissue. SEM images show that cardiovascular calcification is not simply a formation of bone in

soft tissue, but rather a different process potentially originated from a different mechanism that has no parallel with any other tissue. Taken together, the and the elemental analysis obtained at the electron microscope provide clues about the origins of calcification. This is because in order to produce such a unique material, the organism requires a system that can provide the same elements present in the calcification and that can also control its morphology.

References

1. de Jonge N, Ross FM. Electron microscopy of specimens in liquid. Nat Nanotechnol. 2011;6:695–704.
2. Bertazzo S, et al. Nano-analytical electron microscopy reveals fundamental insights into human cardiovascular tissue calcification. Nat Mater. 2013;12:576–83.
3. Tokuyasu KT. A technique for ultracryotomy of cell suspensions and tissues. J Cell Biol. 1973;57:551–65.
4. Braet F, deZanger R, Wisse E. Drying cells for SEM, AFM and TEM by hexamethyldisilazane: a study on hepatic endothelial cells. J Microsc Oxf. 1997;186:84–7.
5. Araujo JC, et al. Comparison of hexamethyldisilazane and critical point drying treatments for SEM analysis of anaerobic biofilms and granular sludge. J Electron Microsc (Tokyo). 2003;52:429–33.
6. Bozzola JJ, Russell LD. Electron microscopy: principles and techniques for biologists. Boston, MA: Jones & Bartlett Learning; 1999.
7. Kuo J. Electron microscopy: methods and protocols, vol. 369. New York, NY: Springer Science & Business Media; 2007.
8. Allen TD. Introduction to electron microscopy for biologists: methods in cell biology, vol. 88. San Diego, CA: Academic Press; 2008.
9. Stirling J, Curry A, Eyden B. Diagnostic electron microscopy: a practical guide to interpretation and technique. Chichester: John Wiley & Sons; 2012.
10. Hunter EE, Maloney P, Bendayan M. Practical electron microscopy: a beginner's illustrated guide. New York, NY: Cambridge University Press; 1993.
11. Kuo J. Electron microscopy: methods and protocols. New York, NY: Springer; 2014.
12. Newman GR, Hobot JA. Resins for combined light and electron microscopy: a half century of development. Histochem J. 1999;31:495–505.
13. Rosca MG, Hoppel CL. Mitochondria in heart failure. Cardiovasc Res. 2010;88:40–50.
14. Wang K, et al. Cardiac tissue slices: preparation, handling, and successful optical mapping. Am J Physiol Heart Circ Physiol. 2015;308:H1112–25.
15. Verveer PJ. Advanced fluorescence microscopy: methods and protocols. New York, NY: Humana Press; 2014.
16. Herman B. Fluorescence microscopy. Oxford: Bios Scientific Publishers; 1998.
17. Benz PM, et al. Mena/VASP and αII-spectrin complexes regulate cytoplasmic actin networks in cardiomyocytes and protect from conduction abnormalities and dilated cardiomyopathy. Cell Commun Signal. 2013;11:1–22.
18. Bertazzo S, Gentleman E. Aortic valve calcification: a bone of contention. Eur Heart J. 2017;38:1189. https://doi.org/10.1093/eurheartj/ehw071.
19. Bertazzo S, Steele JAM, Chester AH, Yacoub MH, Stevens MM. Cardiovascular calcification violet pearl. Lancet. 2014;384:1294.
20. Miller JD. Cardiovascular calcification: orbicular origins. Nat Mater. 2013;12:476–8.
21. Agarwal S, Bertazzo S. New paradigms in cardiovascular calcification. C R Chim. 2016;19:1605. https://doi.org/10.1016/j.crci.2015.09.013.